Bulk Motions of Flat Galaxies on 100-Mpc Scales from New Data

S. L. Parnovsky[*] and A. V. Tugay

Astronomical Observatory, Shevchenko Kiev National University, Kiev, Ukraine

Received July 15, 2003

Abstract—We use a new expanded and partially modified sample of 1501 thin edge-on spiral galaxies from the RFGC catalog to analyze the non-Hubble bulk motions of galaxies on the basis of a generalized multiparameter Tully—Fisher relation. The results obtained have confirmed and refined our previous conclusions (Parnovsky *et al.* 2001), in particular, the statistical significance of the quadrupole and octupole components of the galaxy bulk velocity field. The quadrupole component, which is probably produced by tidal forces from overdense regions, leads to a difference in the recession velocities of galaxies on scales of $8000-10\,000$ km s^{-1} up to 6% of their Hubble velocity. On Local Supercluster scales (3000 km s^{-1}), its contribution increases to about 20%. Including the octupole components in the model causes the dipole component to decrease to the 1σ level. In contrast, in the dipole model, the galaxy bulk velocity relative to the frame of reference of the cosmic microwave background is 310 ± 75 km s^{-1} toward the apex with $l = 311°$ and $b = 12°$. We also consider a sample of 1493 galaxies that was drawn using a more stringent galaxy selection criterion. The difference between the results of our data analysis for this sample and for the sample of 1501 galaxies is primarily attributable to a decrease in the dipole velocity component (290 ± 75 km s^{-1} toward the apex with $l = 310°$ and $b = 12°$) and a decrease in σ by about 2%. © 2004 MAIK "Nauka/Interperiodica".

Key words: *galaxies, large-scale motions.*

INTRODUCTION

Samples of galaxies whose distances have been determined independently of their radial velocities are used to investigate the large-scale bulk motions of galaxies. One such sample is the RFGC catalog of flat galaxies (Karachentsev *et al.* 1999) specially compiled for these purposes. It includes 4236 flat edge-on spiral field galaxies. By 2001, the radial velocities and H I line widths were known for 1328 of them. A sample of 1271 galaxies was obtained after the rejection of clear misses; this sample was used to analyze the large-scale motions on the basis of a generalized multiparameter Tully—Fisher relation. The results obtained were published previously (Parnovsky *et al.* 2001). The bulk motions of galaxies were analyzed in terms of three models of their motion: the dipole (D), quadrupole (dipole+quadrupole, DQ), and octupole (dipole+quadrupole+octupole, DQO) models. Both the quadrupole and octupole components were shown to be statistically significant. Including the octupole component significantly affects the velocity of the dipole component.

Since the publication of our previous paper (Parnovsky *et al.* 2001), we have obtained new data on the radial velocities and H I line widths for several

galaxies. The HyperLeda database (http://leda.univ-lyon1.fr) contains relevant information for 1201 RFGC galaxies. Our previous sample (Parnovsky *et al.* 2001) did not include 233 of these galaxies. For the remaining 968 galaxies, some of the data differed greatly from those used previously. We deemed it necessary to take from them new data for 34 galaxies. The criterion was a significant reduction in the deviation of the galaxy radial velocity from the regression line.

As a result, we have obtained a data set on the basis of which we can calculate the distances and radial peculiar velocities of 1561 galaxies. Naturally, there is a certain percentage of bad data among them that greatly deviate from the regression line. The criterion used to select galaxies can be seen from Fig. 1. In this figure, deviations from the regression line in the D-model are plotted against distance to the galaxies. We see that most of the galaxies lie near the regression line. However, some of the galaxies deviate from it to such an extent that these data should obviously be rejected. Unfortunately, the deviations from the regression line have such a distribution that the boundary can be drawn by various methods. Drawing the boundary closer to the regression line, we reduce the number of sample galaxies, but simultaneously decrease σ. Including additional galaxies causes the number of sample galaxies and the velocity dispersion to increase. The problem is exacerbated by the

---

[*]E-mail: `par@observ.univ.kiev.ua`
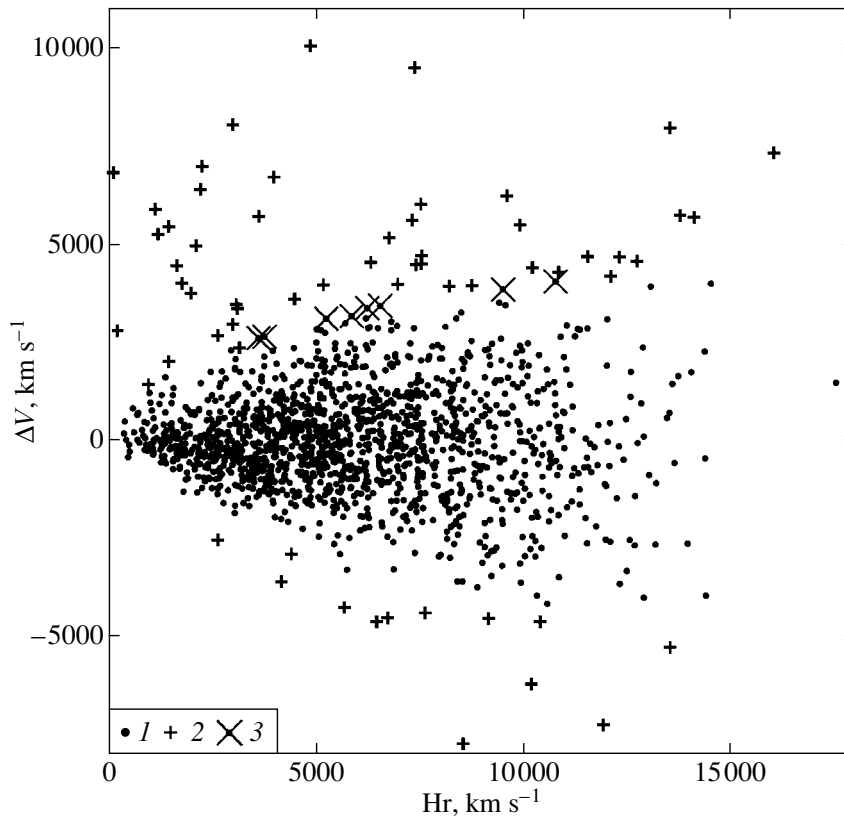
Fig. 1. Deviations of the galaxy radial velocities from the regression line versus distance for the D-model with $R_{max} =$ 10 000 km s^{-1}: (1) regressions and distances to the galaxies were determined for sample 1 of 1501 galaxies, (2) data for the rejected galaxies, (3) data for the 8 galaxies included in sample 1 and excluded from sample 2.

fact that rejecting or including any galaxy leads to a displacement of the regression line and to a change in the distance estimate for all of the remaining galaxies. Therefore, we rejected galaxies using a multistep procedure. After the construction of a regression for all of the available data, we rejected clearly deviating galaxies. After the construction of a new regression, we repeated the operation several times. For large $R = $ Hr, we retained galaxies with peculiar velocities lower than 3500−4000 km s^{-1} (3.5−4σ); for nearby galaxies, we also took into account the ratio of the recession velocity relative to the cosmic microwave background to the galaxy distance. When rejecting galaxies, we disregarded their positions in the sky.

Having applied the multistep rejection procedure, we obtained two samples used here. One of these, which is below referred to as sample 1, contains 1501 galaxies whose deviations from the regression line are seen in Fig. 1. With a slightly more stringent selection criterion, we obtain a sample of 1493 galaxies, which is below referred to as sample 2. In Fig. 1, the 8 galaxies that distinguish sample 1 from sample 2 are indicated by crosses. Their RFGC numbers,

which are given in order of increasing R, i.e., from left to right in Fig. 1, are 1566, 51, 3865, 1806, 2893, 2092, 3396, and 2046. The pluses in Fig. 1 mark the 68 galaxies with large deviations that were excluded from the subsequent analysis. All of the galaxies from samples 1 and 2 are uniformly distributed over the sky, with the natural exception of the Galactic plane (as we see from Fig. 2). At the same time, the 8 galaxies that distinguish samples 1 and 2 have a positive peculiar velocity, as we see from Fig. 1, and lie roughly in the same hemisphere of the sky, as we see from Fig. 2 in which these are indicated by large circles. As a result, as we show below, including or excluding these 8 galaxies, which account for less than 1% of the sample, leads to a change in the magnitude of the dipole velocity component by 4%.

In comparison with the sample used previously (Parnovsky *et al.* 2001), the mean distance to the galaxies decreased only slightly and is 5800 km s^{-1} for sample 2. The sample median (5500 km s^{-1}) and mode (5200 km s^{-1}) are also close to this value. The sample is complete up to distances of about 5600 km s^{-1}. As any combination of observations
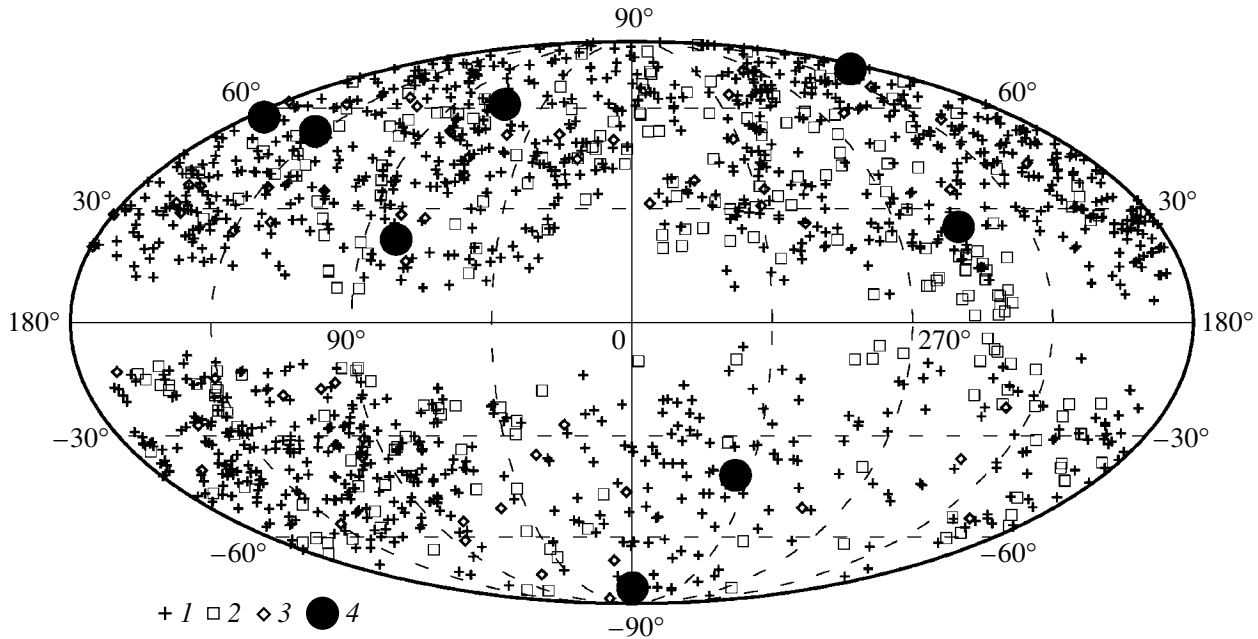
Fig. 2. Sky distribution of the sample of flat galaxies: (*1*) galaxies included in the previously used sample, (*2*) new data, (*3*) bad galaxies that were not involved in our calculations, (*4*) positions of the 8 galaxies included in sample 1 and excluded from sample 2.

with different telescopes in different programs, the sample used is inhomogeneous and asymmetric, particularly at large distances. To eliminate this effect, we used subsamples with limited maximum distances to the galaxies, $R < R_{max}$, in our analysis.

In the near feature, we are going to compile a new list of peculiar velocities for the sample being described and make it accessible via the Internet. It will be supplied with detailed information about the sample properties. For now, we point out that the 216 new galaxies included in sample 2 have mean corrected values of $\langle W \rangle = 295$ km s^{-1}, $\langle V_{3K} \rangle = 5152$ km s^{-1}, $\langle a_b \rangle = 1\rlap{.}'32$, and $\langle a_r \rangle = 1\rlap{.}'25$. For the 34 galaxies for which the data changed compared to the previous sample, the mean corrected sizes are $\langle a_b \rangle = 1\rlap{.}'16$ and $\langle a_r \rangle = 1\rlap{.}'07$. Their mean parameters changed as follows: $\langle W \rangle$ from 321 to 305 km s^{-1} and $\langle V_{3K} \rangle$ from 5801 to 6101 km s^{-1}.

Here, we apply the methods developed previously (Parnovsky *et al.* 2001) to our new samples of 1501 and 1493 galaxies. As a result, we have been able not only to improve the previous results, but also to check the validity of our previous qualitative conclusions (Parnovsky *et al.* 2001) for the new sample.

DESCRIPTION OF THE MODELS

In this paper, we use our previously developed models (Parnovsky *et al.* 2001) for the spatial dis-

tribution of the galaxy radial bulk velocity component V_r, which are based on a multipole expansion. In the simplest D-model,

$$V_r = R + D_i n_i, \tag{1}$$

where $R = \text{Hr}$ is the distance to the galaxy measured in km s^{-1}, **D** is the dipole bulk velocity vector, and **n** is a unit vector directed toward the galaxy and having the Cartesian components (n_1, n_2, n_3). Below, we use the Einstein rule: the summation is performed over any repetitive indices. The DQ-model includes the quadrupole component

$$V_r = R + D_i n_i + R Q_{ij} n_i n_j. \tag{2}$$

The symmetric traceless tensor Q_{ij} is defined by five parameters q_i,

$$Q_{ij} n_i n_j = q_1(n_1^2 - n_3^2) + q_2(n_2^2 - n_3^2) \tag{3}$$
$$+ q_3 n_1 n_2 + q_4 n_1 n_3 + q_5 n_2 n_3.$$

Adding the octupole components yields a DQO-model that can be written in two equivalent forms. In the first form, the octupole contribution is broken down into two parts: the traceless tensor O_{ijk} symmetric in each pair of indices and the vector **P** describing the corrections to the vector **D** quadratic in distance. The tensor **O** is described by seven parameters d'_i, and the vector **P** is described by three components:

$$V_r = R + (D_i + R^2 P_i)n_i \quad (4)$$
$$+ RQ_{ij}n_i n_j + R^2 O_{ijk}n_i n_j n_k,$$

$$V_r^{\text{oct}} = R^2 O_{ijk}n_i n_j n_k = R^2\{d_1'(3n_1 n_2^2 - n_1^3) \quad (5)$$
$$+ d_2'(3n_1 n_3^2 - n_1^3) + d_3'(3n_2 n_1^2 - n_2^3)$$
$$+ d_4'(3n_2 n_3^2 - n_2^3) + d_5'(3n_3 n_1^2 - n_3^3)$$
$$+ d_6'(3n_3 n_2^2 - n_3^3) + d_7' n_1 n_2 n_3\}.$$

The contributions **P** and **O** may be combined into a single tensor $\tilde{\mathbf{O}}$ symmetric in any pair of indices and described by ten parameters d_i, which can be linearly expressed in terms of d_i' and P_i:

$$V_r = R + D_i n_i + RQ_{ij}n_i n_j + R^2 \tilde{O}_{ijk}n_i n_j n_k,$$

$$V_r^{\text{oct}+P} = R^2 \tilde{O}_{ijk}n_i n_j n_k \quad (6)$$
$$= R^2\{d_1 n_1^3 + d_2 n_2^3 + d_3 n_3^3 + d_4 n_1 n_2^2 + d_5 n_1 n_3^2$$
$$+ d_6 n_2 n_1^2 + d_7 n_2 n_3^2 + d_8 n_3 n_1^2$$
$$+ d_9 n_3 n_2^2 + d_{10} n_1 n_2 n_3\}.$$

All of the velocities used here are given in the frame of reference of the cosmic microwave background. The unit vectors (n_1, n_2, n_3) are related to the Galactic coordinates l and b by

$$n_1 \equiv n_z = \sin b, n_2 \equiv n_x = \cos l \cos b, \quad (7)$$
$$n_3 \equiv n_y = \sin l \cos b.$$

The distances R in all models were determined from a fit that generalizes the Tully–Fisher relation (in its "linear size–H I line width" version):

$$R = \frac{W}{a_r}(c_1 + c_2 B + c_3 BT) + c_4 \frac{W}{a_b} \quad (8)$$
$$+ c_5 \left(\frac{W}{a_r}\right)^2 + c_6 \frac{1}{a_r},$$

where W is the H I line width (in km s^{-1}) measured at half maximum and corrected for the cosmological expansion and turbulence; a_r and a_b are the major angular diameters of the galaxy (in arcminutes), respectively, in the red and blue POSS and ESO/SERC reproductions corrected for the inclination of the axis to the line of sight and for the absorption in the Milky Way; T is the centered index of the galaxy morphological type derived from the index of the type I_t in the catalog by subtracting an approximate mean value, $T = I_t - 5.35$; and B is the centered index of the galaxy surface brightness derived from the surface brightness index I_{SB} in the catalog by subtracting an approximate mean value, $B = I_{\text{SB}} - 2$.

The parameters c_i were determined simultaneously with the model parameters by the least-squares method. As a result, the D-model contains 9 parameters, the DQ-model is described by 14 parameters, and 24 parameters and their errors were determined in the DQO-model.

RESULTS

Parameters of the generalized Tully–Fisher relation for all three models, two samples, and two values of R_{max} are given in Table 1 together with their statistical significance estimated by the Fisher test. A comparison of this table with a similar table from our previous paper (Parnovsky *et al.* 2001) shows that the changes in all coefficients lie within the error limits. The statistical significance of all coefficients exceeds 99.95% ($F = 12.1$ corresponds to this confidence level; $F = 3.8$, 6.6, 7.9, and 10.8 correspond to the confidence levels of 95, 99, 99.5, and 99.9%, respectively). Comparing the distances determined previously and given in the list of peculiar velocities by Karachentsev *et al.* (2000a) with the distances calculated using formula (8) with the coefficients from Table 1 for the D-model and $R_{\text{max}} = 10\,000$ km s^{-1}, we see that the differences are insignificant, $\sim$100 km s^{-1}. This suggests that the generalized Tully–Fisher relation did not change significantly. A comparison of the coefficients obtained for two different samples shows that the differences between them for the D- and DQ-models are much smaller than the errors of these quantities. For the DQO-model, a more or less significant difference is observed only for the coefficient c_1 for the subsample with $R_{\text{max}} = 8000$ km s^{-1}.

Previously (Parnovsky *et al.* 2001), we showed that including the octupole term in the analysis for subsamples with R_{max} near 8000 km s^{-1} led to a sharp decrease in the dipole component to the 1σ level. Such a strong "dipole–octupole interaction" is attributable to the same symmetry of these components relative to space inversion. This property is only enhanced for the new samples. Figure 3 shows the corresponding plot for sample 2; the plot for sample 1 differs only slightly from it. As a result, the dipole component for the subsamples with $R_{\text{max}} \approx 8000$ km s^{-1} is statistically significant for the D- and DQ-models and insignificant for the DQO-model. Naturally, the incompleteness and asymmetry of the galaxy sample are responsible for this effect; this asymmetry causes the dipole and octupole regressors to become nonorthogonal for the galaxy sample used.

Compared to the previous sample, the following new effect appears: an increase in the significance of the individual components of the vector **P** to a maximum value of 10.2 for sample 2 and $R_{\text{max}} = 8000$ km s^{-1}. Its components are $P_z = (4.3 \pm 3.1) \times$

Table 1. Coefficients of the generalized Tully–Fisher relation, their errors, and statistical significance

i	D-model		DQ-model		DQO-model	
	c_i	F_i	c_i	F_i	c_i	F_i
Sample 1 of 1501 galaxies, $R_{max} = 8000$ km s^{-1} (1139 galaxies)						
1	16.5 ± 1.7	96	17.7 ± 1.7	108	21.7 ± 1.7	112
2	2.07 ± 0.21	95	2.15 ± 0.22	100	2.17 ± 0.22	101
3	-0.713 ± 0.134	28	-0.724 ± 0.134	29	-0.715 ± 0.133	29
4	8.16 ± 1.47	31	7.30 ± 1.48	24	7.24 ± 1.46	24
5	$(-6.08 \pm 1.60) \times 10^{-3}$	14	$(-6.97 \pm 1.60) \times 10^{-3}$	19	$(-7.51 \pm 1.68) \times 10^{-3}$	20
6	-877 ± 90	94	-917 ± 90	103	-922 ± 90	105
Sample 1 of 1501 galaxies, $R_{max} = 10\,000$ km s^{-1} (1358 galaxies)						
1	18.8 ± 1.5	166	19.9 ± 1.5	181	20.0 ± 1.5	181
2	1.63 ± 0.20	70	1.73 ± 0.20	75	1.78 ± 0.20	78
3	-0.624 ± 0.127	24	-0.657 ± 0.126	27	-0.618 ± 0.128	23
4	5.76 ± 1.28	20	4.85 ± 1.29	14	4.98 ± 1.29	15
5	$(-7.92 \pm 1.06) \times 10^{-3}$	56	$(-8.34 \pm 1.07) \times 10^{-3}$	61	$(-8.50 \pm 1.17) \times 10^{-3}$	52
6	-770 ± 90	73	-806 ± 90	79	-854 ± 91	88
Sample 2 of 1493 galaxies, $R_{max} = 8000$ km s^{-1} (1128 galaxies)						
1	16.7 ± 1.7	99	17.5 ± 1.7	109	17.8 ± 1.7	113
2	2.02 ± 0.21	92	2.09 ± 0.22	94	2.13 ± 0.21	98
3	-0.710 ± 0.133	28	-0.730 ± 0.168	30	-0.732 ± 0.133	30
4	8.09 ± 1.46	31	7.37 ± 1.47	25	7.32 ± 1.46	25
5	$(-6.07 \pm 1.60) \times 10^{-3}$	14	$(-6.93 \pm 1.61) \times 10^{-3}$	19	$(-7.47 \pm 1.68) \times 10^{-3}$	20
6	-881 ± 89	98	-911 ± 89	104	-915 ± 89	106
Sample 2 of 1493 galaxies, $R_{max} = 10\,000$ km s^{-1} (1357 galaxies)						
1	19.2 ± 1.4	179	20.2 ± 1.5	193	20.2 ± 1.5	193
2	1.60 ± 0.19	69	1.69 ± 0.20	73	1.75 ± 0.20	77
3	-0.620 ± 0.125	24	-0.655 ± 0.125	27	-0.616 ± 0.127	24
4	5.28 ± 1.26	18	4.42 ± 1.27	12	4.62 ± 1.27	13
5	$(-7.73 \pm 1.03) \times 10^{-3}$	56	$(-8.14 \pm 1.04) \times 10^{-3}$	61	$(-8.32 \pm 1.15) \times 10^{-3}$	52
6	-789 ± 89	78	-819 ± 90	84	-867 ± 90	93
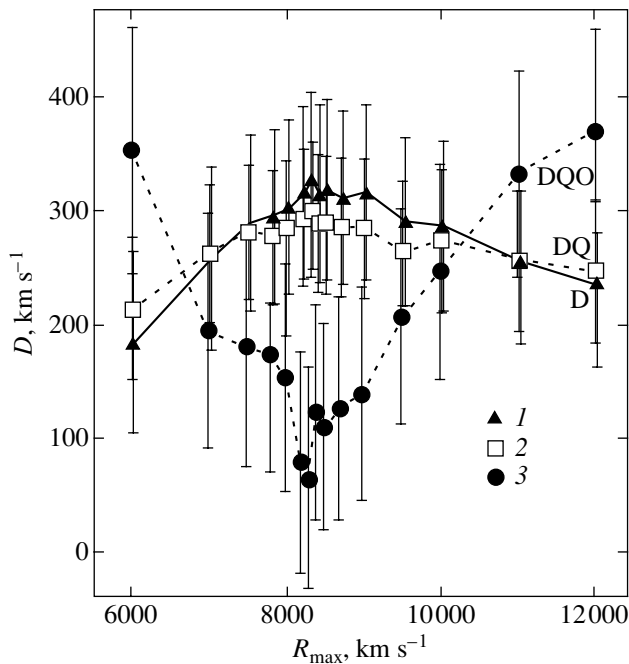
Fig. 3. Magnitude of the dipole velocity component versus maximum distance of the galaxies in the subsample. The calculations were performed with the D-model (*1*), DQ-model (*2*), and DQO-model (*3*). For convenience, the error bars for different models were separated slightly. The plot was constructed for sample 2.

for the entire Mark III catalog by Dekel *et al.* (1999), which yielded a magnitude of 370 km s^{-1} for the dipole velocity component in the direction $l = 305°$, $b = 14°$. Previous results are summarized in the paper by Karachentsev *et al.* (2000b). Table 2 also lists rms deviations of the measured radial velocities from the corresponding regressions. Naturally, the value of this quantity is lower for sample 2. We also see from the table that the magnitude of the dipole in the D-model decreases when passing from sample 1 to sample 2. These changes lie within the error limits. However, the results for sample 2 are closer to the estimates based on the analysis of density perturbations as the Universe expands using the currently universally accepted cosmological parameters, for example, those determined from WMAP satellite data.

Table 3 lists the values, errors, and statistical significance of the individual quadrupole components. We see that only the first component is statistically significant, as in our previous paper (Parnovsky *et al.* 2001). Therefore, we also determined the total statistical significance of the entire quadrupole, which is given in the last row of the table. Note that $F = 3.02$ and 4.10 correspond to the 99% and 99.9% quantiles, respectively. Thus, the statistical significance of the entire quadrupole is about 99% for the DQO-model and $\sim$99.9% for the DQ-model. The significance and amplitude of the quadrupole are slightly higher for sample 1. Combining the quadrupole with the Hubble expansion yields anisotropic recession of the galaxies with a direction-dependent Hubble constant,

$$H(\mathbf{n}) = H + Q_{ij}n_in_j. \tag{9}$$

The tensor of the quadrupole is described by three mutually perpendicular proper vectors and the corresponding proper values, the sum of which is equal to zero. Therefore, one of the axes corresponds to the maximum proper value of Q_1, which is always positive, the second axis corresponds to the negative minimum value of Q_2, and the third proper value of Q_3 can have an arbitrary sign. The Hubble constant is at its maximum and minimum along the first and second axes, respectively. Table 4 gives quadrupole parameters for different subsamples. We see that both the proper values and the directions of the proper axes are always close, except for the direction of the minimum axis for the subsample with $R_{max} = 3000$ km s^{-1}. For sample 2, the directions of the minimum in the DQ- and DQO-models are much closer to each other than those for sample 1. A comparison with a similar table from our previous paper (Parnovsky *et al.* 2001) shows that the directions of the axes can deviate by an angle as large as $20°-30°$. This suggests that, despite the statistical significance

10^{-6}, $P_x = (2.8 \pm 3.9) \times 10^{-6}$, $P_y = (-12.4 \pm 3.9) \times 10^{-6}$. This vector is directed toward the point with $l = 283°$ and $b = 19°$, i.e., toward the Great Attractor and the Shapley concentration. For sample 1 and $R_{max} = 8000$ km s^{-1}, the maximum significance of the **P** component is 8.4, and the components themselves are $P_z = (4.1 \pm 3.1) \times 10^{-6}$, $P_x = (3.9 \pm 3.9) \times 10^{-6}$, $P_y = (-11.2 \pm 3.9) \times 10^{-6}$. The direction of the vector **P** ($l = 289°$, $b = 19°$) almost coincides with the above direction for sample 2. In our previous paper (Parnovsky *et al.* 2001), all of the components of the vector **P** were insignificant. Since the vector **P** in a linearized perturbation theory is proportional to the gradient of the mean mass density, its significance may imply only an increase in density as the Great Attractor is approached.

Table 2 lists parameters of the dipole vector **D**. Due to the above decrease in the magnitude of **D** in the DQO-model, it is statistically insignificant for the sample with $R_{max} = 8000$. Nevertheless, the apex found is in good agreement with the results of our previous paper (Parnovsky *et al.* 2001) and the paper by Karachentsev *et al.* (2000b), who obtained the apex with $l = 328° \pm 15°$ and $b = 7° \pm 15°$. There is also good agreement with the results of the data analysis

Table 2. Parameters of the dipole component of the galaxy velocity field in the Galactic coordinate system

Model and sample	R_{max}	D_z	D_x	D_y	D	l, deg	b, deg	σ, km s^{-1}
				km s^{-1}				
D, 1	8000	63 ± 49	192 ± 62	-240 ± 59	313 ± 78	309	12	1040
DQ, 1	8000	128 ± 52	197 ± 64	-225 ± 61	299 ± 60	311	0	1031
DQO, 1	8000	-74 ± 81	124 ± 108	-47 ± 103	152 ± 98	339	-29	1016
D, 1	10 000	62 ± 51	211 ± 62	-210 ± 62	304 ± 75	315	12	1158
DQ, 1	10 000	-14 ± 55	183 ± 67	-219 ± 65	286 ± 64	310	-3	1151
DQO, 1	10 000	7 ± 80	179 ± 102	-156 ± 101	237 ± 96	319	2	1143
D, 2	8000	64 ± 49	178 ± 61	-237 ± 58	303 ± 76	307	12	1020
DQ, 2	8000	17 ± 51	185 ± 63	-217 ± 61	286 ± 58	311	3	1012
DQO, 2	8000	-63 ± 80	140 ± 106	-74 ± 102	154 ± 100	357	-24	997
D, 2	10 000	61 ± 50	189 ± 61	-209 ± 61	288 ± 74	312	12	1144
DQ, 2	10 000	-2 ± 55	174 ± 66	-212 ± 65	274 ± 63	309	-1	1137
DQO, 2	10 000	14 ± 79	215 ± 101	-125 ± 99	249 ± 95	330	3	1129

Table 3. Parameters of the quadrupole component of the galaxy velocity field in the Galactic coordinate system for sample 1

i	$R_{max} = 8000$ km s^{-1}				$R_{max} = 10\,000$ km s^{-1}			
	DQ-model		DQO-model		DQ-model		DQO-model	
	q_i, %	F_i	q_i, %	F_i	q_i, %	F_i	q_i, %	F_i
1	6.8 ± 1.6	18.4	4.8 ± 1.8	7.4	6.1 ± 1.5	17.2	6.9 ± 1.8	15.1
2	-0.5 ± 1.7	0.1	0.2 ± 1.9	0.0	-1.9 ± 1.5	1.6	-3.0 ± 1.8	2.6
3	-1.3 ± 2.3	0.3	-1.1 ± 2.5	0.2	1.3 ± 2.0	0.4	-0.2 ± 2.3	0.0
4	1.1 ± 2.4	0.2	2.9 ± 2.7	1.2	4.1 ± 2.1	3.7	3.7 ± 2.7	1.9
5	3.1 ± 2.9	1.2	-0.3 ± 3.0	0.0	0.5 ± 2.6	0.4	-1.0 ± 3.0	0.1
Total		5.18		2.79		4.52		3.55

of the quadrupole, the directions of its axes can be reliably determined only by considerably increasing the sample size and completeness. Compared to our previous results (Parnovsky *et al.* 2001), we see that the maximum axis is now fairly stable. Its direction for all models and for R_{max} from 8500 to 10 000 km s^{-1} lies within a 7° × 10° region in Supergalactic coordinates.

One end of the axis is directed toward the Coma cluster, while its opposite end is directed toward the constellation Sculptor. This direction for all samples de-

Table 4. Proper vectors and proper values of the tensor of the quadrupole component

R_{max}, km s^{-1}	N	Maximum					Minimum					Third axis				
		Q_1, %	l	b	Sgl	Sgb	Q_2, %	l	b	Sgl	Sgb	Q_3, %	l	b	Sgl	Sgb
DQ-model, sample 1 of 1501 galaxies																
3000	267	18.3 ± 4	138	-14	346	-2	-17.9 ± 5	271	69	104	-9	-0.4 ± 6.8	44	-15	261	68
6000	855	5.4 ± 1.5	169	60	64	-10	-7.4 ± 1.9	57	12	32	79	2.0 ± 2.4	141	-27	333	-6
7000	984	6.7 ± 1.5	172	74	77	-3	-5.1 ± 1.7	74	2	352	63	-1.6 ± 2.3	343	16	165	26
8000	1139	6.8 ± 1.4	157	85	85	5	-6.7 ± 1.6	105	-3	353	32	-0.1 ± 2.1	15	4	183	58
8500	1217	6.4 ± 1.3	39	82	91	14	-5.5 ± 1.5	111	-2	355	26	-0.9 ± 2.0	21	-7	206	61
9000	1271	6.0 ± 1.2	44	75	91	21	-5.9 ± 1.5	111	-6	350	25	-0.1 ± 1.9	92	-14	335	41
9500	1328	5.8 ± 1.3	62	76	86	20	-4.3 ± 1.4	111	-10	346	25	-1.5 ± 1.9	19	-11	211	57
10 000	1358	6.5 ± 1.3	66	78	86	18	-4.6 ± 1.4	93	-11	339	41	-1.9 ± 1.9	2	-5	193	43
DQO-model, sample 1 of 1501 galaxies																
3000	267	21.1 ± 5	140	-14	346	-4	-18.3 ± 5.0	85	67	75	24	-2.8 ± 6.7	45	-19	265	65
6000	855	4.6 ± 1.9	153	45	47	-6	-6.5 ± 2.0	59	5	354	78	1.9 ± 2.8	144	-44	316	-9
7000	984	4.8 ± 1.9	138	70	70	6	-4.9 ± 1.8	77	-10	331	56	0.1 ± 2.6	350	17	164	33
8000	1139	5.0 ± 1.8	129	79	79	8	-5.2 ± 1.6	89	-8	342	46	0.2 ± 2.4	0	7	176	43
8500	1217	5.7 ± 1.8	86	79	83	15	-4.8 ± 1.6	94	-10	341	41	-0.9 ± 2.4	4	-1	188	46
9000	1271	6.5 ± 1.7	93	78	81	15	-4.7 ± 1.5	100	-12	341	35	-1.8 ± 2.4	10	-1	190	52
9500	1328	6.8 ± 1.8	100	82	84	11	-4.6 ± 1.6	87	-7	342	48	-2.2 ± 2.4	357	2	183	40
10 000	1358	7.2 ± 1.8	96	81	83	12	-4.4 ± 1.6	71	-9	327	62	-2.8 ± 2.4	161	-4	358	-24
DQ-model, sample 2 of 1493 galaxies																
3000	267	18.3 ± 4	138	-14	346	-2	-17.9 ± 5	89	69	75	22	0.4 ± 6.4	44	-15	261	68
6000	855	4.8 ± 1.5	354	-61	247	11	-7.2 ± 1.9	59	13	31	78	2.4 ± 2.4	143	-12	349	-7
7000	990	5.7 ± 1.5	15	-74	261	7	-5.3 ± 1.7	81	7	3	57	-0.4 ± 2.3	349	-14	200	29
8000	1128	5.8 ± 1.4	118	89	89	7	-6.4 ± 1.6	104	-1	355	33	0.6 ± 2.1	14	3	184	57
8500	1211	5.7 ± 1.2	20	78	96	17	-5.4 ± 1.6	112	0	357	25	-0.3 ± 2.0	22	-12	216	59
9000	1268	5.8 ± 1.1	30	70	96	25	-6.0 ± 1.5	109	-4	352	28	0.2 ± 1.9	18	-19	222	52
9500	1321	5.5 ± 1.2	43	76	91	20	-4.5 ± 1.4	106	-6	349	30	-1.0 ± 1.8	15	-12	210	53
10 000	1357	5.8 ± 1.2	54	78	89	18	-4.8 ± 1.3	86	-10	337	48	-1.0 ± 1.8	354	-6	192	35
DQO-model, sample 2 of 1493 galaxies																
3000	267	21.1 ± 5	140	-14	346	-4	-18.3 ± 5	85	67	75	24	-2.8 ± 7.1	45	-18	265	66
6000	855	3.7 ± 1.9	154	24	26	-12	-5.9 ± 2.0	62	5	356	75	2.2 ± 2.8	142	-66	294	-8
7000	990	4.5 ± 1.9	154	74	75	2	-5.2 ± 1.8	82	-5	343	54	0.7 ± 2.6	353	15	166	36
8000	1128	4.2 ± 1.7	75	82	86	13	-5.1 ± 1.6	89	-7	343	46	0.9 ± 2.3	359	-2	188	41
8500	1211	5.1 ± 1.7	54	78	89	18	-4.5 ± 1.6	96	-9	343	39	-0.6 ± 2.3	5	-8	198	45
9000	1268	6.0 ± 1.7	73	80	86	15	-4.7 ± 1.5	102	-9	345	33	-1.3 ± 2.3	12	-5	197	53
9500	1321	6.2 ± 1.8	69	84	88	12	-4.4 ± 1.6	94	-6	346	42	-1.8 ± 2.4	4	-3	191	46
10 000	1357	6.8 ± 1.7	77	82	86	13	-4.4 ± 1.6	79	-8	336	55	-2.4 ± 2.3	349	0	184	31

Table 5. Parameters of the octupole component of the galaxy velocity field in the Galactic coordinate system

i	Sample 1 of 1501 galaxies				Sample 2 of 1493 galaxies			
	$R_{\max} = 8000$ km s^{-1}		$R_{\max} = 10\,000$ km s^{-1}		$R_{\max} = 8000$ km s^{-1}		$R_{\max} = 10\,000$ km s^{-1}	
	d_i, 10^6	F_i	d_i, 10^6	F_i	d_i, 10^6	F_i	d_i, 10^6	F_i
1	8.1 ± 4.1	3.9	-4.9 ± 3.4	2.1	7.0 ± 4.1	3.0	-6.2 ± 3.3	3.5
2	3.5 ± 5.8	0.4	0.6 ± 4.0	0.2	2.7 ± 5.7	0.2	0.1 ± 3.9	0.0
3	-8.6 ± 5.3	2.6	-8.3 ± 4.7	3.1	-9.3 ± 5.3	3.0	-9.2 ± 4.6	4.1
4	11.5 ± 7.5	2.3	11.1 ± 5.2	4.6	13.1 ± 7.5	3.1	13.7 ± 5.1	7.3
5	-15.2 ± 7.6	4.0	0.9 ± 6.3	0.0	-12.9 ± 7.6	2.9	2.1 ± 6.2	0.1
6	13.0 ± 7.9	2.8	8.4 ± 5.9	2.1	12.7 ± 7.8	2.6	7.6 ± 5.8	1.7
7	-3.9 ± 9.9	0.2	-10.7 ± 8.4	1.6	-7.1 ± 9.8	0.5	-17.0 ± 8.2	4.3
8	5.1 ± 8.2	0.4	13.4 ± 6.5	4.3	2.6 ± 8.2	0.1	11.6 ± 6.3	3.3
9	-35.4 ± 9.5	14.0	-9.9 ± 7.0	2.0	-36.6 ± 9.4	15.2	-7.6 ± 6.9	1.2
10	35.1 ± 10.5	11.2	19.9 ± 7.9	6.4	34.9 ± 10.4	11.2	16.1 ± 7.7	4.3

viates from the Supergalactic plane by no more than $20°$. For the sample with $R_{\max} = 3000$ km s^{-1} within the Local Supercluster, the maximum axis lies almost in the Supergalactic plane, while the minimum axis deviates from it by no more than $24°$. This corresponds to the results by Hoffman *et al.* (2001), who asserted that the principal plane of the quadrupole tensor is close to the Supergalactic plane. However, the directions of the axes of the tensor **Q** are clearly different from those obtained by these authors. Note that Hoffman *et al.* (2001) considered a subsample with $R_{\max} \approx 7000$ km s^{-1}. For a similar subsample, Table 4 gives a direction of the minimum axis that clearly does not lie in the Supergalactic plane. For the subsample with $R_{\max} = 3000$ km s^{-1}, our results for the proper values are close to those by Staveley-Smith and Davies (1989), but the directions of the proper axes differ.

Compared to our previous paper (Parnovsky *et al.* 2001), Q_1 slightly increased, while $|Q_2|$ decreased. As a result, the sign of Q_3 ceased to be positive and became negative for all but one of the samples with $R_{\max} > 8500$ km s^{-1}. The direction of the minimum axis, which was fairly stable in our previous paper (Parnovsky *et al.* 2001), was preserved (the constel-

lation Lacerta in one direction and the constellation Vela in the opposite direction).

Parameters of the octupole written in form (6) are given in Table 5. We see that there are both statistically significant and statistically insignificant parameters among them. The total statistical significance of the entire octupole is described by $F = 4.38(4.21)$ for $R_{\max} = 8000$ km s^{-1} and $F = 2.72(2.34)$ for $R_{\max} = 10\,000$ km s^{-1}. The values for sample 2 are given in parentheses. These values should be compared with 2.32 and 2.96 that correspond to the 99% and 99.9% confidence levels, respectively. Thus, the significance of the octupole exceeds 99%. Its sky distribution is displayed in Figs. 4a and 4b, which show isolines of the function $F(l, b) = 10^6 \tilde{\mathbf{O}}_{ijk} n_i n_j n_k$ for sample 1.

The overall pattern of the peculiar velocity field is shown in Figs. 4c and 4d for $R = 8000$ km s^{-1} and $R_{\max} = 10\,000$ km s^{-1} for samples 1 and 2, respectively. It is similar to the previous pattern and is characterized by a sharp minimum directed toward the constellation Cygnus. This feature almost coincides for both samples. In other directions, the peculiar velocity field can differ, but only slightly.
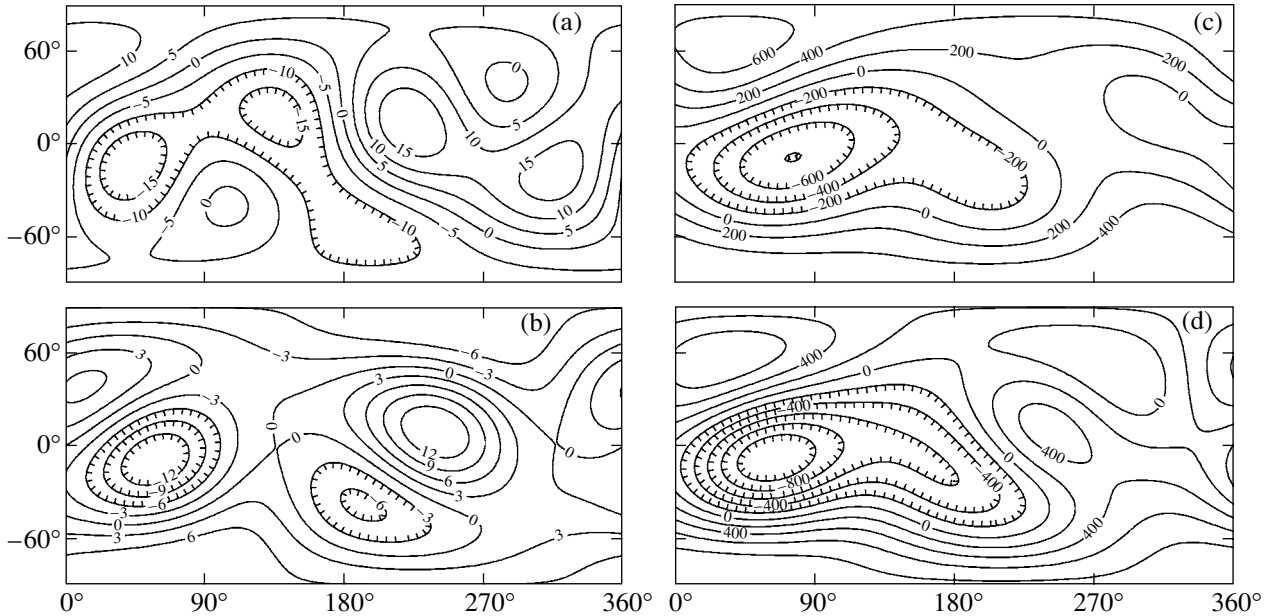
Fig. 4. Lines of constant radial velocity for the octupole of the galaxy bulk motion for two subsamples with $R_{max} = 8000$ km s^{-1} (a) and $R_{max} = 10\,000$ km s^{-1} (b). Panels (c) and (d) show lines of constant velocity for the total bulk motion for $R = 8000$ km s^{-1} for samples 1 and 2. We used the DQO-model with $R_{max} = 10\,000$ km s^{-1}. Galactic coordinates lie along the axes.

Naturally, some of the galaxies have radial velocities that differ from the models under consideration. Rms deviations are given in Table 2. The distribution of these deviations resembles a Gaussian, but using the χ^2 test shows that its deviation from a Gaussian is statistically significant.

CONCLUSIONS

We have confirmed and refined the results of our previous paper (Parnovsky *et al.* 2001) for the samples of flat spiral galaxies from the RFGC catalog obtained by adding new data for 233 galaxies and improving data for 34 galaxies. The main conclusions remain the same:

The quadrupole and octupole components of the galaxy bulk motion are statistically significant.

The dipole velocity component (bulk motion) decreases to 1σ when the octupole terms are included in the model.

The magnitude of the dipole component is 290 ± 75 km s^{-1}, and its apex is in the direction of $l = 310°$ and $b = 12°$ in the D-model. While the direction of the apex is well preserved, the magnitude of the dipole velocity component for sample 2 decreased by 44 km s^{-1} compared to its previously obtained value (Parnovsky *et al.* (2001).

A new result is the appearance of the statistically significant vector **P**, which is indicative of an increase

in the mean mass density toward the Great Attractor. We have improved the parameters of the multiparameter Tully–Fisher relation and the quadrupole tensor for the bulk motion. The anisotropy in the galaxy recession velocities lies within $\pm 7\%$ for samples with R_{max} from 7000 to 10 000 km s^{-1}.

One of our most important results is the possibility of determining the peculiar velocities for 1561 galaxies and for any galaxies from the RFGC catalog with measured radial velocities and H I line widths. Such a list, which refines and expands the list by Karachentsev *et al.* (2000a), is to be made accessible for all interested readers in the near future. These data have already been used by P.Yu. Sharov to analyze the mass density distribution by the POTENT method (this paper has been submitted for publication in the Journal *Kinematics and Physics of Celestial Bodies*) and by S.L. Parnovsky, O.Z. Gaidamaka, and P.Yu. Sharov to determine the cosmological parameters Ω_m and σ_8.

In this paper, we present the results for two samples. In our opinion, sample 2 is better. When the number of galaxies is slightly reduced, it yields a tangible decrease in the dispersion of the results and a magnitude of the dipole velocity component that is in better agreement with cosmological data. The galaxy peculiar velocities can subsequently be used both for the rejected 8 galaxies in this sample and for any galaxies that were not included in the sample but

still have a reasonable deviation from the regression line in Fig. 1.

ACKNOWLEDGMENTS

REFERENCES

1. A. Dekel, A. Eldar, T. Kolatt, *et al.*, Astrophys. J. **522**, 1 (1999).
2. Y. Hoffman, A. Eldar, S. Zaroubi, and A. Dekel, astro-ph/0102190 (2001).
3. I. D. Karachentsev, V. E. Karachentseva, Y. N. Kudrya, *et al.*, Bull. Spec. Astrophys. Observ. **50**, 5 (2000a); astro-ph/0107058.
4. I. D. Karachentsev, V. E. Karachentseva, Y. N. Kudrya, and S. L. Parnovsky, Astron. Zh. **77**, 175 (2000b) [Astron. Rep. **44**, 150 (2000b)].
5. I. D. Karachentsev, V. E. Karachentseva, Y. N. Kudrya, *et al.*, Bull. Spec. Astrophys. Observ. **47**, 5 (1999); astro-ph/0305566.
6. S. L. Parnovsky, Yu. N. Kudrya, V. E. Karachentseva, and I. D. Karachentsev, Pis'ma Astron. Zh. **27**, 890 (2001) [Astron. Lett. **27**, 765 (2001)].
7. L. Staveley-Smith and R. D. Davies, Mon. Not. R. Astron. Soc. **241**, 787 (1989).

Translated by V. Astakhov

Observations of Radio Emission from the Cosmic Gamma-Ray Burst GRB 030329

A. M. Finkelstein[1], A. V. Ipatov[1], Yu. N. Gnedin[2], D. V. Ivanov[1], M. A. Kharinov[1], and I. A. Rakhimov[1]*

[1]*Institute of Applied Astronomy, Russian Academy of Sciences, nab. Kutuzova 10, St. Petersburg, 191187 Russia*
[2]*Pulkovo Astronomical Observatory, Russian Academy of Sciences, Pulkovskoe sh. 65, St. Petersburg, 196140 Russia*

Received August 7, 2003

Abstract—We present the radio observations of the afterglow from the intense cosmic gamma-ray burst GRB 030329 performed with the radio telescopes of the Institute of Applied Astronomy, Russian Academy of Sciences, at the Svetloe ($\lambda = 3.5$ cm) and Zelenchuk ($\lambda = 6$ cm) Observatories. The difference between the fluxes measured in two different polarization modes suggests the existence of a circular polarization in the radio afterglow from GRB 030329. However, since the measurement errors of the fluxes with different circular polarizations are large, we cannot draw a firm conclusion about its detection; we can only set an upper limit on its value. An analysis of the possible generation mechanisms for the circular polarization of the relativistic jet suggests that there is a helical magnetic field in the jet. The existence of significant flux densities at various wavelengths during a long (≥ 10 days) period leads us to conclude that the hydrodynamic evolution of the relativistic bow shock takes place in the stellar wind, not in the interstellar medium. We have estimated the total GRB energy ($E = 10^{51}$ erg) (under the assumption of isotropic radiation) and the plasma density of the stellar wind from the presupernova ($n = 3$ cm^{-3}). The magnetic-field strength in the relativistic jet can be estimated as $B \approx 100$ G. © *2004 MAIK "Nauka/Interperiodica"*.

Key words: *radio astronomy, cosmic gamma-ray bursts, polarization.*

INTRODUCTION

The cosmic gamma-ray burst GRB 030329 was recorded by the High Energy Transient Explorer (HETE) gamma-ray observatory at 11:14:14.6 UT on March 29, 2003 (Vanderspek *et al.* 2003; Lamb *et al.* 2003; Ricker *et al.* 2003). The fluence of this extremely intense burst with a characteristic duration of $\sim$50 s was $\sim 10^{-4}$ erg cm^{-2}; its peak flux in the energy range 30−400 keV exceeded 7×10^{-6} erg cm^{-2}, i.e., it was more than a factor of 100 higher than the flux from the Crab Nebula in the same energy range. This burst was also recorded by the Konus−Wind observatory (Golenetskii *et al.* 2003) in the energy range 15−5000 keV with the following parameters: a fluence of 1.6×10^{-4} erg cm^{-2}, a peak flux of 2.5×10^{-5} erg cm^{-2} s^{-1}, and an energy at peak intensity of 150 keV.

Immediately after the discovery of this burst, Peterson and Price (2003) and Torii (2003) detected a very bright ($R \sim 13^m$) optical transient with the coordinates $\alpha = 10^h 44^m 50\overset{s}{.}0$ and $\delta = +21°31'17''\!.8$

(J 2000.0). The brightness of this transient slowly decreased with time (Uemura *et al.* 2003). Due to the significant brightness of the optical transient and the slow rate of decrease in its brightness, this event has become an object of numerous observations in various spectral ranges.

The afterglow proved to be bright in the X-ray (Marshall and Swank 2003), radio (Berger *et al.* 2003), submillimeter (Hoge *et al.* 2003), and infrared spectral ranges. Blake and Bloom (2003) estimated the upper limit on the brightness of the GRB host galaxy to be $R = 22^m\!.5$. The first spectroscopic observations of the optical transient were carried out by Martini *et al.* (2003) and Della Ceca *et al.* (2003). They identified only one spectral feature and, having attributed it to the O II emission line, estimated the redshift to be $z = 0.58$. However, more detailed and reliable VLT observations (Greiner *et al.* 2003a) yield the redshift $z = 0.1685$. Thus, GRB 030329 is the second nearest (after GRB 980425) cosmic gamma-ray burst.

Russian astronomers observed the optical transient with the 1.5-m RTT-150 telescope installed at the Turkish TUBITAK National Observatory (Burenin *et al.* 2003) and with the MASTER system

*E-mail: `amf@quasar.ipa.nw.ru`

installed by the staff of the Sternberg Astronomical Institute (SAI) near Moscow (Lipunov *et al.* 2003). Spectroscopic observations of the optical transient were also performed with the 6-m BTA telescope (Fatkhullin *et al.* 2003). Photometric and polarimetric observations of the afterglow from GRB 030329 were also carried out at the Crimean Astrophysical Observatory, Ukraine (Rumyantsev *et al.* 2003), the Crimean Station of the SAI (Lyuty and Metlov 2003), and the Mount Maidanak Observatory, Uzbekistan (Ibragimov *et al.* 2003).

The numerous spectroscopic observations, including those performed with the 6.5-m MMT telescope and the 6.5-m Magellan telescope, have shown that the spectrum of the optical transient is remarkably similar to the spectra of type-Ib/c supernovae, including the spectrum of SN 1998bw. However, in contrast to the latter, which was identified in the optical transient of GRB 980425 only on the basis of the behavior of its light curve and color characteristics, the supernova in the optical transient of GRB 030329 was first identified on the basis of spectroscopic observations (Stanek *et al.* 2003).

Radio observations of the optical transient of GBR 030329 were carried out with the RTF-32 radio telescopes of the Institute of Applied Astronomy, Russian Academy of Sciences (IAA RAS), in the village of Svetloe, Leningrad region, on April 11 and 12, 2003 (Finkelshtein *et al.* 2003), and with the RATAN-600 radio telescope of the Special Astrophysical Observatory, Russian Academy of Sciences (SAO RAS), at the Zelenchuk Station of the Karachaevo-Cherkessian Republic on April 11–13, 2003 (Trushkin 2003).

Below, we present our observations and compare them with other radio observations of the afterglow from GRB 030329 and with radio observations of the afterglows from other GRBs.

OBSERVATIONS OF THE RADIO FLUX FROM GRB 030329 WITH THE IAA RAS RTF-32 TELESCOPES

The RTF-32 radio telescope is a quasi-parabolic 32-m dish with a secondary quasi-hyperboloid 4 m in diameter and 11.4 m in focal length that has an azimuthal mounting and an rms surface error of 0.5 mm. The pointing accuracy of the instrument is $10''$ (Finkelstein 2001).

Cryoelectronic radiometers in the 18/21, 13, 6, 3.5, and 1.35 cm wavelength ranges with a reception bandwidth of about 500 MHz were mounted on the radio telescope (Ipatov *et al.* 1997). In single-dish mode, the radiometers operate according to a pilot-signal scheme, and information is recorded with a digital recording system (Gornovesov *et al.* 1997).

Parameters of the receiving systems at the Svetloe and Zelenchuk Observatories are given in Table 1.

The source was continuously scanned by the RTF-32 beam to eliminate atmospheric effects during long signal accumulation. The object under study was followed by the radio telescope for 60 min; the source was azimuthally scanned by the antenna beam to eliminate atmospheric effects. At 3.5 cm, we chose the scanning amplitude and speed to be $\pm 12'$ and $45''$ s^{-1}, respectively, and, hence, the total number of scans was 110. At 6 cm, we chose the scanning amplitude and speed to be $\pm 20'$ and $40''$ s^{-1}, respectively, and, hence, the total number of scans was 60. The data in the scans were azimuthally aligned and averaged over all scans. A Gaussian was fitted to the points obtained through averaging by the least-squares method (see the figure). The error was determined as the accuracy of fitting a Gaussian to the averaging results. The results of our observations are summarized in Tables 2 and 3. The time corresponds to the middle of the individual observation. Since the observations were carried out under variable cloudiness conditions, the accuracy of our results is much higher than the theoretical limit P in most cases (2.4 and 1.1 mJy for 3.5 cm LCP and RCP, respectively; 2.1 mJy for 6 cm RCP). Only at 6 cm, at which the atmospheric effects are weaker, does the accuracy of the individual results approach the theoretical limit. We calibrated the flux using the source 3C 286, whose flux was assumed to be 7480 mJy at 6 cm and 5200 mJy at 3.5 cm.

Table 2 presents our observations of the radio afterglow from GRB 030329 at wavelength $\lambda = 3.5$ cm in both (right- and left-hand) circular polarization on April 11 and 12, 2003 (UT). The radio fluxes are given in mJy. The fluxes at $\lambda = 6$ cm are listed in Table 3. The observations at this wavelength span the period of April 11–13, but they were performed only in one polarization mode. It should be noted that the results of our observations are in satisfactory agreement with the data of other authors obtained before our observations and during a period close to our observations (Table 4). The observations, the results of which are presented in Table 4, were carried out at wavelengths that occasionally differed from our wavelengths. A comparison with other observations shows variability of the radio emission, which is most likely attributable to the propagation effects in the dense medium surrounding the GRB 030329 source similar to interstellar scintillation effects. These effects are common to the radio afterglows of cosmic GRBs (see Frail *et al.* 2000; Berger 2003). Below, we discuss in more detail the comparison of our observations with those of other authors and compare our observations with theoretical models of cosmic GRBs.

Table 1. Parameters of the receiving systems at the Svetloe and Zelenchuk Observatories

Wavelength range		T_{rec}, K	T_{an}, K	T_{sys}, K	SUF	SEFD, Jy	Δf, MHz	P_{min}, mJy
Zelenchuk	RCP	24	24	48	0.69	258	505	16.2
6 cm								
Svetloe	LCP	39	27.5	66.5	0.57	400	495	25.4
3.5 cm	RCP	14.4	26.5	40.9	0.56	250	900	11.8

Note: T_{rec} is the equivalent receiver input noise temperature; T_{an} is the equivalent antenna noise temperature at the receiver input; T_{sys} is the equivalent system noise temperature at the receiver input; SUF is the surface utilization factor; SEFD is the system equivalent flux density; P_{min} is the sensitivity in radio flux density; and Δf is the frequency bandwidth. The sensitivity in flux density was calculated using the formula $P_{min} = \sqrt{2}\text{SEFD}\sqrt{\Delta F/\Delta f}$, where ΔF is the integrator output filter pass band, in our case, 1 Hz.

Table 2. Results of the Svetloe observations at 3.5 cm

Date, 2003	Time, UT	LCP		RCP		P_V
		F, mJy	σ	F, mJy	σ	
Apr. 11	18:42	1.8	10.1	21.9	4.5	–
Apr. 12	17:32	1.4	12.8	16.8	5.8	–
Apr. 12	19:09	2.8	11.4	22.9	5.2	–
Mean		2.02	6.51	20.94	2.94	0.824 ± 0.400

MEASURED RADIO FLUXES: COMPARISON WITH OTHER OBSERVATIONS AND WITH THEORETICAL MODELS

A remarkable property of the afterglows from cosmic GRBs is the appearance of an appreciable radio flux several days after the GRB itself. Radio observations allow the following characteristic parameters to be determined for the afterglow region of cosmic gamma-ray emission: (i) the phase of the nonrelativistic shock propagation; (ii) the density profile of the circumstellar matter through which the shock propagates; and (iii) the basic parameters of the star-forming region hidden by a thick layer of matter in the host galaxy. They also allow the synchrotron radiation from the relativistic electrons of the reverse shock to be determined. The characteristic reverse-wave emission time scale was estimated by analyzing the observations of several previous cosmic GRBs (Sari and Piran 1999; Berger 2003):

$$t_{max} \sim \Delta t \left(\frac{\omega_{opt}}{\omega_{rad}}\right)^{0.7}, \qquad (1)$$

where Δt is the characteristic duration of the GRB itself. For GRB 030329, $\Delta t \ll 50$ s. Choosing $\lambda_{opt} \sim \lambda_B \sim 0.44\mu m$ and $\lambda_{rad} \sim 6$ cm, we obtain $t_{max} \sim 3$ days. This implies that our observations were most likely performed at the maximum of the bow-shock emission that is reached precisely near ~ 10 days and that slowly ($t^{-1/3}$) decays with time (Berger 2003).

An analysis indicates that our data and other observations presented in Table 4 are in satisfactory agreement.

First of all, we can establish the law of variations in the radio flux from the afterglow of GRB 030329 with time if we compare the fluxes obtained at approximately the same wavelength but at different epochs. We compared the MRAO fluxes on 03.04.07 UT and 04.04.11 UT at $\lambda = 2$ cm as well as the VLBA flux on 01.04.05 UT at $\lambda = 3.57$ cm with the mean value of our data obtained with the radio telescope at Svetloe Observatory. This comparison leads us to conclude that the radio flux was virtually constant over the period from 03.04 until 11.04, i.e., $F_\nu \sim t^0$.

This result is in good agreement with the theoretical calculations of the hydrodynamic evolution of a relativistic bow shock in a stellar wind (Wu *et al.* 2003; see Figs. 1−6 from this paper).

Based on the widely used hydrodynamic calculations of the propagation of a bow shock through a stellar wind and interstellar medium (Chevalier and Li 2000), we can estimate the total burst energy (the energy estimate for the isotropic case is commonly used) and the density of the stellar wind from the presupernova. According to the Chevalier−Li theory, the maximum radio flux is

$$F_{\nu, max} \sim E^{1/2} A D^{-2}, \qquad (2)$$
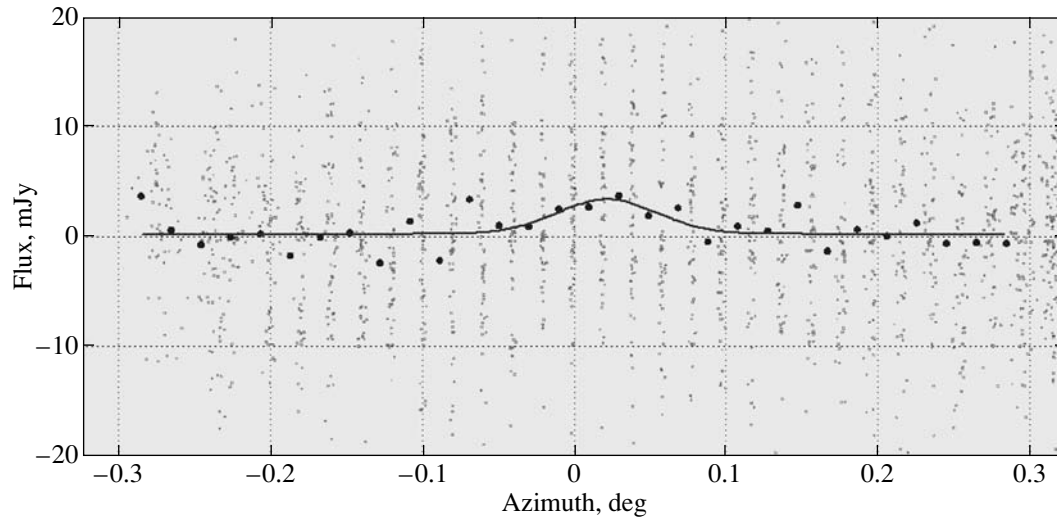
Results of 6-cm observations.

where

$$A = \dot{M}/4\pi m_p V_{\rm W} = 3 \times 10^{34} \quad (\dot{M}/(10^{-6} M_\odot) \, {\rm yr})$$

(10^3 km s^{-1} $V_{\rm W}$), $V_{\rm W}$ is the stellar-wind velocity, and D is the distance to the GRB.

The hydrodynamic calculations by Wu *et al.* (2003) and formula (2) allow us to estimate the burst energy. The cosmological redshift $z = 0.186$ for GRB 030329 corresponds to a distance $D \approx 10^3$ Mpc if the Hubble constant is assumed to be $H_0 = 70$ km s^{-1} Mpc^{-1}. A burst energy estimate of $E \sim 10^{51}$ erg for $A = 3 \times 10^{34}$ cm^{-1} then follows from Fig. 1 in the paper by Wu *et al.* (2003). A stellar-wind density of $n \approx 3$ cm^{-3} corresponds to $A = nR^2$ if the shock radius is chosen to be $R = 10^{17}$ cm (Wu *et al.* 2003). This density lies within the range $0.1 \leq n \leq 10^2$ cm^{-3} for the afterglows of other GRBs (Holland *et al.* 2003).

The power-law spectral index α of the synchrotron radiation can in principle be determined from quasi-simultaneous observations of the radio emission from GRB 030329 at various wavelengths, although a sufficient amount of data for the same epoch is required for this determination. For this purpose, we use the MRAO data that were kindly made available to us by G. Pooley in a private communication. The fluxes measured by this author on April 11 and 12 at $\lambda = 2$ cm lies between 20 and 30 mJy, in satisfactory agreement with our data. The following preliminary conclusion can be drawn from a comparison of all these data: the radiation spectrum is most likely flat and may even be inverted, i.e., $\alpha \leq 0$ (see Tables 1–3). This implies that the spectral index S of the relativistic electrons responsible for the synchrotron radiation was close to unity, i.e., $S \sim 1$, at the epochs of our observations.

ESTIMATING THE CIRCULAR POLARIZATION OF RADIO EMISSION FROM GRB 030329 AND POSSIBLE GENERATION MECHANISMS OF POLARIZED EMISSION

The circular polarization of the emission from the radio transient of GRB 030329 can be estimated from the data obtained with the RTF-32 Svetloe Observatory telescope (Table 2).

The degree of circular polarization is defined as

$$P_{\rm V} = \frac{V_{\rm R} - V_{\rm L}}{V_{\rm R} + V_{\rm L}}, \tag{3}$$

Table 3. Results of the Zelenchuk observations at 6 cm

Date, 2003	Time, UT	RCP	
		F, mJy	σ
Apr. 11	20:59	8.3	2.2
Apr. 11	22:48	8.3	3.1
Apr. 12	16:24	10.1	2.6
Apr. 12	18:07	10.1	6.6
Apr. 12	19:50	10.1	3.1
Apr. 12	21:33	8.8	3.1
Apr. 12	23:15	9.6	3.1
Apr. 13	15:19	12.3	4.4
Apr. 13	17:02	11.8	3.5
Apr. 13	18:57	19.3	5.7
Apr. 13	20:42	10.1	3.5
Apr. 13	22:25	8.3	3.1

Table 4. Radio observations of GRB 030329

Date of observation (month, day, UT)	Instrument	Wavelength, cm	Flux, mJy
03.30.06	VLA	3.55	3.5
03.30.116.35−31.03.30	MRAO, Cambridge	2	9.8
03.31.91	MRAO	2	18
04.01.98			16
03.31.14−18	GMRT	23.3	1.100 ± 0.150
04.01.14−22			0.330 ± 0.100
04.01.05	VLBA	3.57	8.3 ± 0.4
04.03.07	JCMT	0.085	30 ± 0.5
04.03.07	MRAO	2	20
04.04.11			28
04.03.11.03	Nobeyama	1.3	32.2 ± 0.9
−17.0		0.7	53.9 ± 2.9
		0.333	80.4 ± 5.6
04.03−7	RATAN-600	7.7	49 ± 10
		4.0	33 ± 5
		2.68	20 ± 5
04.11.16.47	IAA RAS, Svetloe	3.5	30.4 ± 9.7
			18.7 ± 4.7
04.11.18.12			27.1 ± 7.8
			7.8 ± 4.2
04.11.18.46	IAA RAS, Zelenchuk	6	18.4 ± 3.2
04.11.22.48			
04.12.18.43	IAA RAS, Svetloe	3.5	18.1 ± 5.2
			7.8 ± 2.8
04.12−13	IAA RAS, Zelenchuk	6	$10−20 \pm 2.6$
04.11−12	MRAO	2	30
04.13−21	RATAN-600	7.7	15 ± 3
		4.0	28 ± 5
		2.68	47 ± 7
05.01−07	RATAN-600	7.7	15 ± 3
		4.0	15 ± 3
		2.68	32 ± 6
05.15−31	RATAN-600	7.7	10 ± 3
		4.0	18 ± 3
		2.68	19 ± 4

Note: See GCN Circ. by Berger *et al.* (2003), Pooley (2003), Pramesh *et al.* (2003), Taylor *et al.* (2003), Hoge *et al.* (2003), Kuno *et al.* (2003), Finkelstein *et al.* (2003), and Trushkin (2003).

where V_R and V_L are the radiation fluxes with right- and left-hand circular polarizations, respectively.

The error in the degree of polarization can be estimated by the standard method (Clarke and Stewart 1986):

$$\sigma_P = \frac{\sqrt{(\sigma_R^2 + \sigma_L^2)(1 + P_V^2)}}{V_R + V_L}, \qquad (4)$$

where σ_R and σ_L are the errors in the radiation fluxes with right-hand (R) and left-hand (L) circular polarizations presented in Table 2. The last row of this table gives the degree of circular polarization and its errors averaged over all observational data. The procedure consisted in averaging the Stokes parameters rather than the degree of polarization itself. The final error was determined using formula (4). The parameters were averaged with weights using the technique by Agekyan (1972).

It follows from Table 2 that we may reach a conclusion only about the possibility of circularly polarized radio emission being generated in cosmic GRBs and can determine an upper limit for the degree of polarization. The possible existence of circular polarization was discussed by Matsumiya and Ioka (2003). In the future, we are planning to perform a more detailed analysis of our observational data and will attempt to isolate the signal amplitude corresponding to a circularly polarized radio emission with a higher reliability.

Let us briefly analyze the possible generation mechanisms of circularly polarized emission under typical conditions of the radio transient of GRB 030329.

First note that we may assert with certainty that a linear polarization has been detected from the optical afterglows of several cosmic GRBs, including GRB 030329 (Greiner *et al.* 2003b).

The synchrotron radiation mechanism that is generally believed (see the reviews by Meszaros (2002) and Hurley *et al.* (2003)) to be responsible for the optical and radio emission of the transient gives rise in principle to a circular polarization (Sazonov 1969; Jones and O'Dell 1977):

$$P_V \approx \varepsilon_V \left(\frac{\nu_B}{\nu}\right)^{1/2} \cot\Theta, \qquad (5)$$

where $\nu_B = eB\sin\Theta/2\pi m_e c$ is the cyclotron frequency, ν is the emission frequency, Θ is the angle between the magnetic-field direction and the line of sight, and ε_V is the factor that depends on the spectral index S of the relativistic electrons, which may be assumed to be on the order of unity under reasonable ($S \sim 2$–3) assumptions. Formula (5) is valid only if $\gamma\sin\Theta \gg 1$, where γ is the Lorentz factor of the relativistic electrons.

Since the characteristic frequency of the synchrotron spectrum for an optically thin source is $\nu \sim \gamma^2$, the degree of circular polarization $P_V \sim 1/\gamma$ is much lower than the degree of linear polarization $P_l = (3S + 3)/(3S + 7)$, which generally exceeds the 50% level. In principle, a situation where $P_V > P_l$ is possible for the synchrotron mechanism. However, this situation takes place only if the relativistic electron beam is highly anisotropic; in this case, there is a strong gradient in the electron pitch-angle distribution within Θ (Sazonov 1969).

In a nonrelativistic magnetoactive plasma, the relationship between the polarization states is opposite: $P_V > P_l$. This relationship stems from the fact that the high-frequency ($\nu \gg \nu_B$) electromagnetic waves (commonly called normal modes) in a nonrelativistic plasma with a magnetic field are circularly polarized over a wide range of angles Θ (except a narrow region $\Theta \approx \pi/2$). While propagating through such a plasma with different phase velocities, they produce circularly polarized radiation as they exit from it. Another well-known effect is the Faraday rotation of the plane of linear polarization of the linearly polarized radiation that passes through such a plasma.

Of course, the presence of a substantial amount of nonrelativistic plasma in the region of the radio afterglow from GRB 030329 can give rise to a detectable circular polarization, but only if the nonrelativistic plasma component significantly dominates over the relativistic component. However, for standard models of comic GRBs, is is assumed that this situation can arise only about 100 days after the GRB itself.

Nevertheless, there are several possibilities for the generation of a detectable circular polarization in the emission of a relativistic plasma. The first is the gyrosynchrotron emission of a mildly relativistic plasma with an anisotropic electron pitch-angle distribution. Ramaty (1969) and Takakura (1972) pointed out that circular polarization dominates in the emission of mildly relativistic electrons. Detailed numerical calculations of the spectral distribution and the degree of polarization of such a plasma have recently been performed by Fleishman and Melnikov (2003). The degree of circular polarization is particularly high for small viewing angles with respect to the relativistic jet (the so-called quasi-longitudinal propagation of emission) and low if the jet is seen at a large angle (quasi-transverse propagation). The calculations by Fleishman and Melnikov (2003) have shown that anisotropy in a mildly relativistic loss-cone electron beam, i.e., $f \sim \sin^N\left(\frac{\pi}{2}\frac{\Theta}{\Theta_c}\right)$ at $0 < \Theta < \Theta_c$ and $N \gg 1$, gives rise to a significant circular polarization of the gyrosynchrotron emission from electrons at frequencies $\omega \geq 10\omega_B$. The calculations were performed for various ratios ω_P/ω_B, where ω_P is the plasma

frequency of the nonrelativistic plasma surrounding the relativistic beam. The degree of polarization is high over a wide range of ratios $\omega_P/\omega_B : \omega_P/\omega_B \ll 1$, $\omega_P/\omega_B > 1$. The change in the spectral index of the gyrosynchrotron emission is more significant.

The polarization spectra of the synchrotron radiation from relativistic jets were calculated in detail by Zheleznyakov and Koryagin (2002). In particular, these authors analyzed the polarization characteristics of a jet composed of an electron–positron plasma in which the normal waves had a purely linear polarization. In principle, an admixture of a cold nonrelativistic plasma can give rise to a detectable circular polarization of the synchrotron radiation from a relativistic jet. This is the well-known effect of the so-called circular repolarization (Pacholczyk 1977).

The most interesting theoretical result by Zheleznyakov and Koryagin (2002) is the possibility of significant circular polarization of the emission from a relativistic electron–positron plasma in the presence of a magnetic-field shear. The degree of circular polarization oscillates with decreasing plasma frequency and changes its sign, which makes it more difficult to observe over a wide frequency range. If the shear is close to the location from which the radiation emerges from the jet, then either there is no detectable circular polarization or it is observed at low frequencies, below the spectral intensity maximum of the relativistic electron–positron jet calculated by Zheleznyakov and Koryagin (2002). If, however, the shear is localized inside the jet itself, then the frequency range of detectable circular polarization includes the frequency of the spectral intensity maximum and the frequency range above the maximum itself.

We do not rule out the possibility that the presence of a magnetic-field shear in the relativistic electron–positron jet gives rise to a detectable circular polarization of the radio emission at $\lambda = 3.5$ cm.

BASIC CONCLUSIONS

Our observations of the afterglow from the intense gamma-ray burst GRB 030329 performed almost simultaneously at wavelengths $\lambda = 3.5$ cm and $\lambda = 6$ cm with the RTF-32 IAA RAS telescopes at the Svetloe and Zelenchuk Observatories have allowed us to place an upper limit on the circular polarization of the GRB radio afterglow. An analysis of the possible generation mechanisms for the circular polarization of the relativistic jet leads us to conclude that there is a magnetic-field shear in the jet itself (Zheleznyakov and Koryagin 2002) or to assume that the magnetic field of the jet has a helical structure. In the latter case, a transition from the quasi-transverse propagation of an electromagnetic wave dominated

by linear polarization to its quasi-longitudinal propagation characterized precisely by a circular polarization is possible.

The existence of significant flux densities during a long ($>1-10$ days) period suggests that that the hydrodynamic evolution of the relativistic bow shock takes place precisely in the stellar wind, not in the interstellar medium with a roughly uniform density. Based on the theoretical calculations by Wu *et al.* (2003), we can estimate the total gamma-ray energy released during the supernova explosion, $E \approx 10^{51}$ erg, and the plasma density of the pre-supernova stellar wind, $n \approx 3$ cm^{-3}. The magnetic-field strength in the radio emission generation region probably does not exceed $B \approx 10^2$ G (if the spectral index of the relativistic electrons in this region is assumed in the model of gyrosynchrotron emission to be $S \sim 1$).

REFERENCES

1. T. A. Agekyan, *Foundations of the Error Theory for Astronomers and Physicists* (Nauka, Moscow, 1972) [in Russian].
2. E. Berger, astro-ph/0304346 (2003).
3. E. Berger, A. M. Soderberg, and D. A. Frail, GCN Circ., No. 2014 (2003).
4. C. Blake and J. C. Bloom, GCN Circ., No. 2011 (2003).
5. R. A. Burenin, R. A. Sunyaev, and M. N. Pavlinsky, Pis'ma Astron. Zh. **29**, 649 (2003) [Astron. Lett. **29**, 573 (2003)].
6. R. A. Chevalier and Z. Li, Astrophys. J. **536**, 195 (2000).
7. D. Clarke and B. G. Stewart, Vistas Astron. **29**, 27 (1986).
8. R. Della Ceca, T. Maccacaro, D. Fugazza, *et al.*, GCN Circ., No. 2015 (2003).
9. T. Fatkhullin, V. Komarova, V. Sokolov, *et al.*, GCN Circ. No. 2142 (2003).
10. A. M. Finkelstein, Nauka Ross. **5**, 20 (2001).
11. A. M. Finkelstein, A. V. Ipatov, and Yu. N. Gnedin, GCN Circ., No. 2161 (2003).

12. G. D. Fleishman and V. F. Melnikov, Astrophys. J. **587**, 823 (2003).

13. D. A. Frail, E. Waxman, and S. R. Kulkarni, Astrophys. J. **537**, 191 (2000).

14. S. Golenetskii, E. Mazets, V. Pal'shin, *et al.*, GCN Circ., No. 2026 (2003).

15. S. Yu. Gornovesov, N. E. Kol'tsov, and N. E. Tsarev, Tr. Inst. Prikl. Astron. Ross. Akad. Nauk **2**, 111 (1997).

16. J. Greiner, S. Klose, K. Reinsch, *et al.*, astro-ph/0312089 (2003a).

17. J. Greiner, M. Peimbert, C. Estaban, *et al.*, GCN Circ., No. 2020 (2003b).

18. J. C. Hoge, R. Meijerink, R. P. J. Tulanis, and I. A. Smith, GCN Circ., No. 2088 (2003).

19. S. T. Holland, M. Weidinger, J. P. U. Fynbo, *et al.*, Astron. J. **125**, 2291 (2003).

20. K. Hurley, R. Sari, and S. G. Djorgovski, astro-ph/0211620 (2002).

21. M. A. Ibragimov, I. M. Astandiyarov, B. B. Kakharov, *et al.*, GCN Circ., No. 2077 (2003).

22. A. V. Ipatov *et al.*, Tr. Inst. Prikl. Astron. Ross. Akad. Nauk **2**, 242 (1997).

23. T. W. Jones and S. L. O'Dell, Astrophys. J. **214**, 522 (1977).

24. N. Kuno, N. Sato, and H. Nakanishi, GCN Circ., No. 2089 (2003).

25. D. Q. Lamb, D. York, J. Barentine, *et al.*, GCN Circ., No. 2040 (2003).

26. V. Lipunov, A. Krylov, V. Kornilov, *et al.*, GCN Circ., Nos. 2035, 2091 (2003).

27. V. Lyuty and V. Metlov, GCN Circ., No. 2113 (2003).

28. P. Martini, P. Garnavich, and K. Z. Stanek, GCN Circ., No. 2013 (2003).

29. F. E. Marshall and J. H. Swank, GCN Circ., No. 1996 (2003).

30. M. Matsumiya and K. Ioka, Astrophys. J. Lett. **595**, L25 (2003).

31. P. Meszaros, Annu. Rev. Astron. Astrophys. **40**, 137 (2002).

32. A. Pacholczyk, *Radio Galaxies* (Pergamon, 1977; Mir, Moscow, 1980).

33. B. A. Peterson and P. A. Price, GCN Circ., No. 1985 (2003).

34. G. Pooley, GCN Circ., No. 2043 (2003), GCN Circ., No. 2072 (2003), GCN Circ., No. 2090 (2003).

35. A. Pramesh Rao, C. H. Ishwara Chandra, D. Bhattacharya, and A. J. Castro-Tirado, GCN Circ., No. 2268 (2003).

36. R. Ramaty, Astrophys. J. **158**, 753 (1969).

37. G. R. Ricker and HETE Sci. Team, Astronomer's Telegram No. 8101 (2003).

38. V. Rumyantsev, E. Pavlenko, Y. Efimov, *et al.*, GCN Circ. No. 2005 (2003).

39. R. Sari and T. Piran, Astrophys. J. Lett. **517**, L109 (1999).

40. V. N. Sazonov, Astron. Zh. **46**, 502 (1969) [Sov. Astron. **13**, 396 (1969)].

41. K. Z. Stanek, T. Matheson, P. M. Garnavich, *et al.*, astro-ph/0304173 (2003).

42. T. Takakura, Sol. Phys. **26**, 151 (1972).

43. G. B. Taylor, E. Berger, D. A. Frail, and S. R. Kulkarni, GCN Circ., No. 2129 (2003).

44. K. Torii, GCN Circ. 1986 (2003).

45. S. A. Trushkin, GCN Circ., No. 2282 (2003).

46. M. Uemura, H. Yamaoka, R. Ishioka, and T. Kato, GCN Circ., No. 1994 (2003).

47. R. Vanderspek, G. Ricker, T. Donaghy, and HETE Sci. Team, GCN Circ., No. 1997 (2003).

48. X. F. Wu, Z. G. Dai, Y. F. Huang, and T. Lu, astro-ph/0304110 (2003).

49. V. V. Zheleznyakov and S. A. Koryagin, Pis'ma Astron. Zh. **28**, 809 (2002) [Astron. Lett. **28**, 727 (2002)].

Translated by V. Astakhov

Plasma Instability in Relativistic Jets

S. L. Ginzburg, V. F. D'yachenko, V. V. Paleychik, A. L. Sudarikov, and V. M. Chechetkin[*]

Keldysh Institute of Applied Mathematics, Russian Academy of Sciences,
Miusskaya pl. 4a, Moscow, 125047 Russia
Received October 21, 2003

Abstract—Based on the Maxwell–Vlasov equations, we consider the possible generation mechanisms of hard emission through the growth of plasma instabilities in a relativistic jet composed of electrons and protons. The accelerated material of the jet moves by inertia. When a small difference arises between the electron and proton velocities (which may result from the interaction of jet material with background plasma or from the acceleration mechanism) plasma instabilities can grow. The particle distribution functions, which were initially delta functions both in angle and in energy, transform into complex angular and energy dependences. In this case, the probability of collisions between high-energy particles in the jet increases, resulting in hard gamma-ray emission. © *2004 MAIK "Nauka/Interperiodica".*

Key words: *accretion, jet theory and stellar wind, gamma-ray emission, plasma instability.*

INTRODUCTION

In recent years, much attention has been drawn to the relativistic jets associated with active galactic nuclei and other objects. Observations of such objects (e.g., BL Lacertae) are indicative of a high gamma-ray luminosity in the GeV and TeV energy ranges for photons with variability on timescales from several days to several hours (von Montigny *et al.* 1995; Mukherjee *et al.* 1997). In general, the TeV-range variability is not related to the GeV-range variability (Mattox *et al.* 1996; Gaidos *et al.* 1996). However, a correlation monitoring suggests that the gamma-ray emission is generally accompanied by activity in the radio and optical ranges (Lin *et al.* 1994; Buckley *et al.* 1996).

Published models of these phenomena are usually based on the inverse Compton effect for the scattering of soft photons, for example, those from an accretion disk, by relativistic electrons of the jet (Reich *et al.* 1993; Mecke *et al.* 1996). These models require the assumption that the jet material is optically transparent for soft photons, while the study is focused on the radiation problems, and the origin of the relativistic electrons is not considered.

Recently, several models that explain the appearance of relativistic electrons have been proposed. Bisnovatyi-Kogan and Lovelace (1995) considered the acceleration of charged particles in the field of a strong electromagnetic wave. The wave is emitted when the electric current oscillates in a separate clump during the formation of which the electric charge is polarized. Wagner (1996), Dermer *et al.* (1992), and Dermer and Schlickeiser (1993) used models of the hadron origin of high-energy gamma rays, but did not elucidate the cause of the generation of the hadrons themselves. The substantiation of the appearance of hadrons of various kinds is of considerable importance for the future. In our paper, we propose possible mechanisms of their generation in relativistic jets under conditions of plasma instability. In addition, there are discrepancies in the time variations of the emission in existing models. In the future, we may be able to solve this problem.

Pohl and Schlickeiser (2000) and Pohl (1999) have proposed mechanisms of high-energy gamma-ray emission based on the particle acceleration in blast waves or on two-stream instability in proton–electron beams. However, the question of the nature of these phenomena arises here again. Galanin *et al.* (1999) studied the mechanisms of jet acceleration to relativistic energies through the interaction of matter with photons from a central source. It is interesting to note that oblique shocks can emerge in jet structures (Savel'ev *et al.* 1996). Structures similar to transverse shocks and a transverse magnetic field are observed in relativistic jets (Gabuzda 1999).

FORMULATION OF THE PROBLEM

As we see from the situation described above, many physical characteristics of the jets still remain to be determined. In particular, there is no
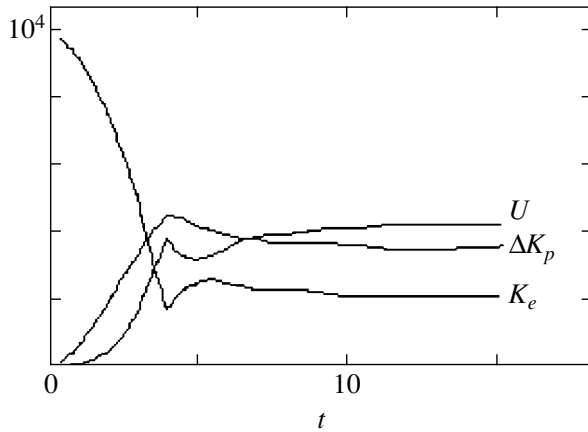
Fig. 1. Redistribution of the initial kinetic energy of electrons K_{e0}: K_e is the energy of the electrons, ΔK_p is the energy transferred to the protons, and U is the energy of the electromagnetic field.

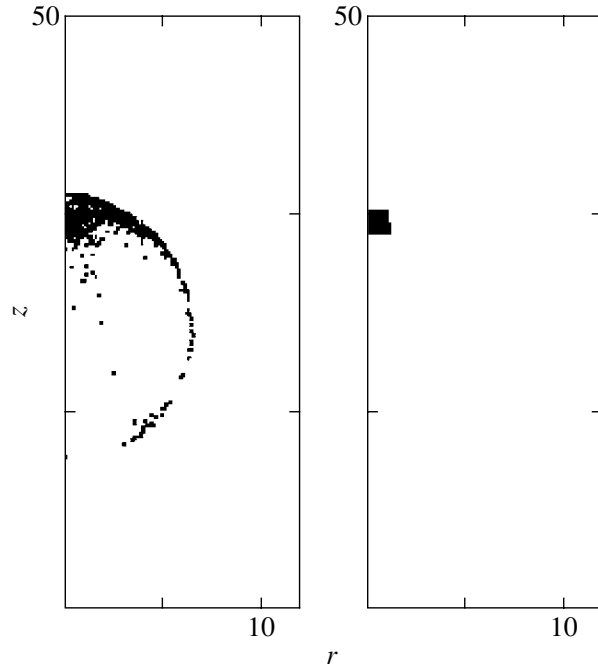**Fig. 2.** An electron cloud and a proton core at time $t = 10$.

self-consistent model of jet acceleration. However, Galanin *et al.* (1999) managed to obtain relativistic velocities of the material through light pressure under certain conditions: for some of the calculations, the velocity of the material was $0.96c$, which corresponds to the relativistic factor $\gamma = 3.57$.

Another interesting fact is that a relativistic factor of 10^6 is observed for the leptonic part of the jets (Birk, 1999). Naturally, it cannot be so large for the baryonic component of the relativistic jets, because the energy is limited.

In our paper, the emphasis is on the decay time of the deltalike proton distribution function. Observations of jets on large scales suggest that the angular distribution function for the proton component is close to a deltalike function. It would be natural to assume that a deltalike distribution also holds for the momenta. The problem lies in determining the characteristic lifetime of such a deltalike proton distribution. For definiteness, we take a proton velocity of $0.9c$, in agreement with the results by Galanin *et al.* (1999).

For electrons, we take a γ factor of 100, but, as our calculations show, the electron factor affects the proton distribution function only slightly. This result is obvious because of the huge difference between the kinetic energies of electrons and protons.

We consider a two-stream problem. Our goal is to determine the transformation efficiency of the kinetic energy of a relativistic beam to hard gamma-ray emission. The interaction of plasma with an electromagnetic field is described by the system of Maxwell–

Vlasov equations. For the above choice of units, this system is

$$\frac{\partial \mathbf{E}}{\partial t} - \nabla \times \mathbf{H} + \mathbf{j} = \mathbf{0}, \qquad \nabla \mathbf{E} = \rho,$$

$$\frac{\partial \mathbf{H}}{\partial t} + \nabla \times \mathbf{E} = \mathbf{0}, \qquad \nabla \mathbf{H} = 0,$$

$$\frac{\partial f_{e,p}}{\partial t} + \mathbf{v}_{e,p} \frac{\partial f_{e,p}}{\partial \mathbf{x}} + q_{e,p} \left(\mathbf{E} + \mathbf{v}_{e,p} \times \mathbf{H} \right)$$
$$\times \frac{\partial f_{e,p}}{\partial \mathbf{p}} = 0,$$

where $\mathbf{E}(t, \mathbf{x})$, $\mathbf{H}(t, \mathbf{x})$ is the electromagnetic field; $f(t, \mathbf{x}, \mathbf{p})$ are the distribution functions; $\mathbf{v} = \partial w / \partial \mathbf{p}$ are the velocities; $w = \left(m^2 + \mathbf{p}^2 \right)^{1/2}$ are the energies; m is the rest masses; and q are the electron (e) and proton (p) charges, respectively. The charge and current densities are

$$\rho = \sum q \int f d^3 p, \qquad \mathbf{j} = \sum q \int \mathbf{v} f d^3 p$$

with the summation over the types of particles. Below, we use the following system of units: the length is the characteristic scale length L; the velocity is the speed of light c; the time is L/c; the frequency is c/L; the particle mass is the electron rest mass m; the particle momentum is mc; the particle energy is mc^2; the field is mc^2/eL, where e is the elementary
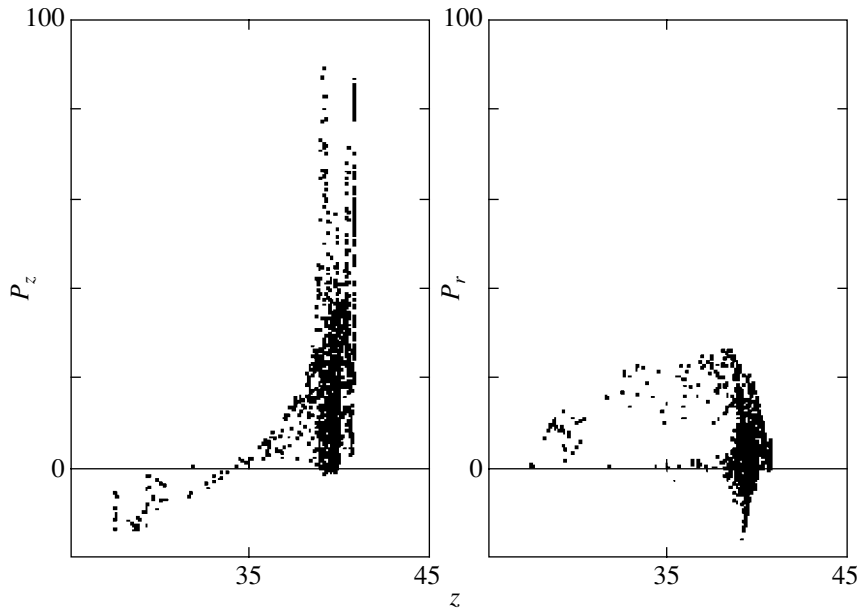
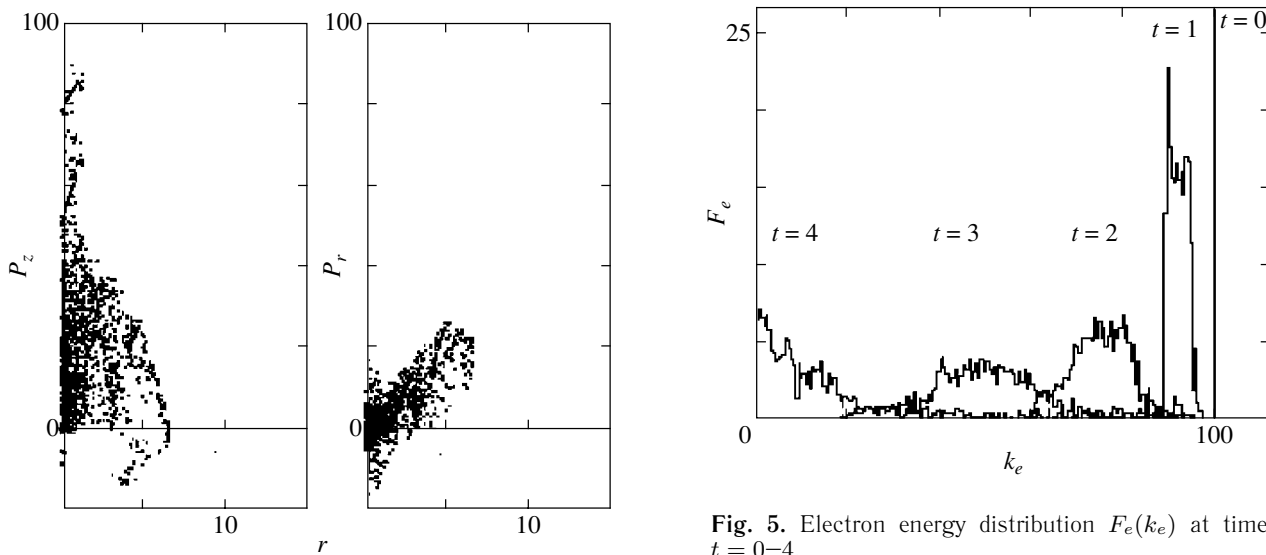**Fig. 3.** (P_z, z) and (P_r, z) projections of the electron phase portrait at $t = 10$.

Fig. 4. (P_z, r), (P_r, r) projections of the electron phase portrait at $t = 10$.

Fig. 5. Electron energy distribution $F_e(k_e)$ at times $t = 0$–4.

charge; the particle number density is $mc^2/4\pi e^2 L^2$; the charge density is $mc^2/4\pi e L^2$; the number of particles is $mc^2 L/2e^2$; the energy distribution function is $L/2e^2$; and the energy is $m^2 c^4 L/2e^2$. In these units, the proton mass is $m_p = 1836$, the electron mass is $m_e = 1$, and the charges are $q = \pm 1$, respectively.

In the problem, we assume axial symmetry $(\partial/\partial\varphi \equiv 0)$ and use the cylindrical coordinates r, φ, z. Although the problem is posed over the entire space, the actual calculation is performed in a bounded region on the surface of which we set artificial boundary conditions that imitate the openness of the boundary for the exit of particles and emission, but its closeness for the entrance of these and any types of energy. The physical justification of these boundary conditions suggests that the energy density inside the beam (both in particles and in emission) is much higher than that outside. Therefore, the external energy was disregarded in our calculations.

The problem was solved by a numerical method; the basic principles of its algorithm (the difference scheme for the Maxwell equations and the macroparticle method for the Vlasov equation) were described by D'yachenko (1985).
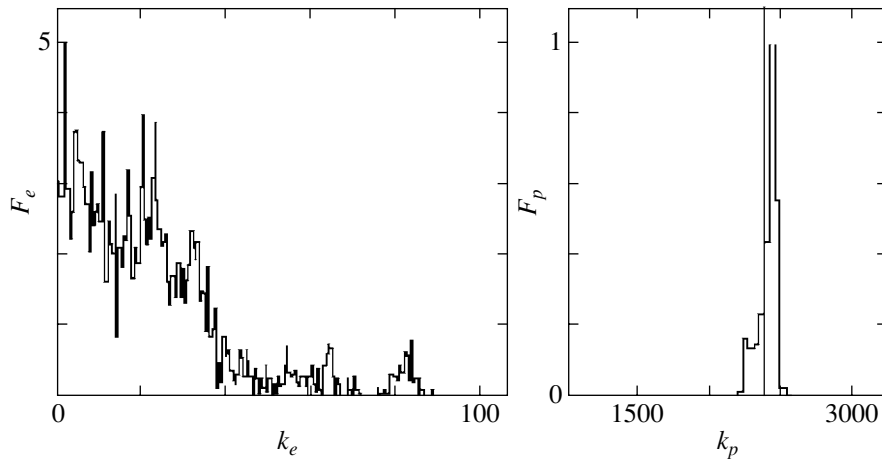
Fig. 6. Electron ($F_e(k_e)$) and proton ($F_p(k_p)$) energy distributions at $t = 10$.
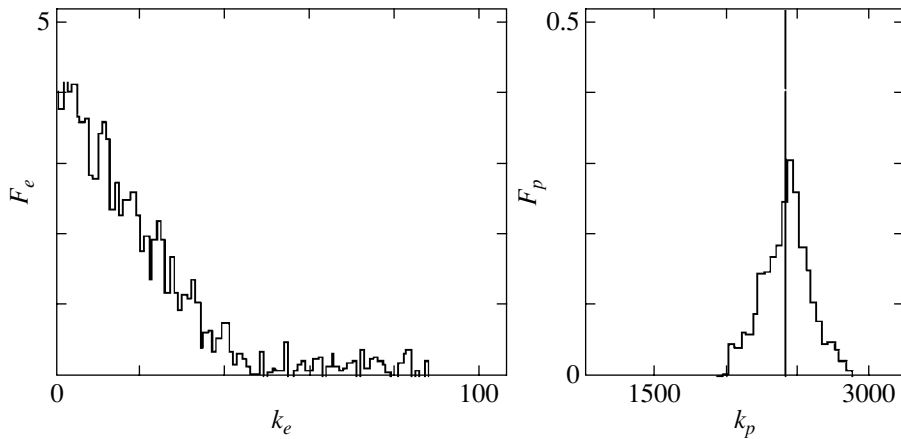

Fig. 7. Same as in Fig. 6, but at $t = 50$.

RESULTS OF THE CALCULATIONS

At the initial time, there is no field, and a plasma composed of electrons and protons with equal number densities, $n_{e0} = n_{p0} = 200$, fills a cylinder of radius $R_0 = 1$ and height $\Delta Z = 1$ located within the computational region. The particle velocities have only an axial component; the electron velocity is $v_{e0} = 0.99995$, implying that the kinetic energy is $k_{e0} = w_{e0} - m_e = 99$. For protons, $v_{p0} = 0.9$ and $k_{p0} = w_{p0} - m_p = 2377$ respectively.

The initial state is rapidly modified. Figure 1, which shows the energy redistribution with time, gives an idea of this modification. Here, the total energy of the electrons K_e decreases severalfold in 4 time units (from $K_{e0} = 10^4$ to $K_e = 1670$). Slightly less than half of it is transferred to protons ($\Delta K_p = 4460$); the rest goes into the excitation of the electromagnetic field (frequency ~ 27) to the energy $U = 3733$. Subsequently, the achieved ratio of the added proton energy to the electron energy (~ 2) is conserved.

Figure 2 demonstrates the location of the electron cloud at time $t = 10$ in the meridian r, z section. The disklike front layer of the electrons that have detached from their protons clearly seen. The remaining electrons, which actively interact with the protons, lag behind and form a broad cloud. For comparison, the right-hand panel shows the 'black square' formed by protons. Subsequently, the electron cloud retains its spherical shape, concentrating near the proton core in its head and increasing in size. It is important to note that this configuration (bubble) is preserved in the vicinity of the head of the relativistic beam that moves almost at the speed of light.

Figures 3 and 4 show the (P_z, z), (P_r, z), (P_z, r), (P_r, r) projections of the phase portrait of the electron fraction at time $t = 10$. Note that a tenfold decrease in electron momentum, from 100 to 10, implies a decrease in velocity from 0.99995 to 0.995. Only a
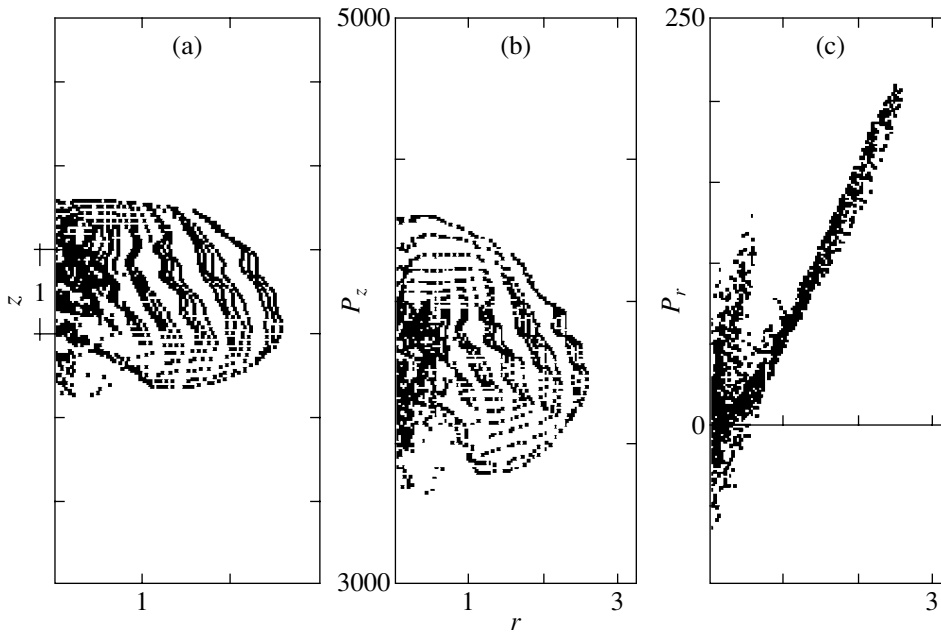
Fig. 8. Proton core (a) and (P_z, r) (b) and (P_r, r) (c) projections of the proton phase portrait at $t = 50$.

50-fold decrease in momentum makes the electron and proton velocities equal.

The initial state described above implies a deltalike energy distribution function, $f \sim \delta(k - k_0)$. Figure 5 shows the distributions $F_e(k_e)$ for the entire ensemble of electrons, i.e., the integral of f_e over space, at specific times. These plots show the initial smearing of the energy distribution function. Figures 6 and 7 demonstrate the subsequent evolution of the electron ($F_e(k_e)$) and proton ($F_p(k_p)$) distributions (the vertical lines on the $F_p(k_p)$ plots denote the initial proton energy, 2377). By the time $t = 50$, the proton energy k_p is within the range of 2000−2800, i.e., it differs from the initial energy by no more than 17%. Subsequently, this difference reaches 25%.

Figure 8 shows the configuration of the proton core (Fig. 8a) and its phase portraits (P_z, r) (Fig. 8b) and (P_r, r) (Fig. 8c) at $t = 50$.

CONCLUSIONS

Our calculations show a new possibility for modeling the high-energy gamma-ray emission. The derived proton and electron distribution functions allow us to estimate the production rate of hadrons of various types and the direct high-energy gamma-ray emission.

The jet acceleration mechanism proposed by Galanin *et al.* (1999) requires the generation of soft photons within the jet itself, because the material surrounding the jet can absorb photons from the accretion disk. However, even in this case, there is a possibility of the passage of very soft photons from the disk through the material surrounding the jet. In the future, it will be necessary to calculate the γp process, which also leads to the generation of hard gamma rays, using the derived proton distribution functions. It is interesting to note that, because of allowance for the shape factor, the peak of this emission lies within in the GeV energy range.

REFERENCES

1. J. T. Birk, in *Plasma Turbulence and Energetic Particles in Astrophysics,* Ed. by M. Ostrowski and R. Schlickeiser (Observ. Astron. Univ. Jangiellonski, Krakow, 1999), p. 321.
2. G. S. Bisnovatyi-Kogan and R. V. E. Lovelace, Astron. Astrophys. **296**, L17 (1995).
3. J. H. Buckley, C. W. Akerlof, and S. Biller, Astrophys. J. **472**, L9 (1996).
4. C. D. Dermer and R. Schlickeiser, Astrophys. J. **416**, 458 (1993).
5. C. D. Dermer, R. Schlickeiser, and A. Mastichiadis, Astron. Astrophys. **256**, L27 (1992).
6. V. F. D'yachenko, Zh. Vychisl. Mat. Mat. Fiz. **4**, 622 (1985).

7. D. C. Gabuzda, in *Plasma Turbulence and Energetic Particles in Astrophysics,* Ed. by M. Ostrowski and R. Schlickeiser (Observ. Astron. Univ. Jangiellonski, Krakow, 1999), p. 301.

8. J. A. Gaidos, C. W. Akerlof, S. Biller, *et al.*, Nature **383**, 319 (1996).

9. M. P. Galanin, Yu. M. Toropin, and V. M. Chechetkin, Astron. Zh. **76**, 143 (1999) [Astron. Rep. **43**, 119 (1999)].

10. Y. C. Lin, J. Chiang, P. F. Michelson, *et al.*, in *Proceedings of the 2nd Compton Symposium,* Ed. by C. E. Fichetel *et al.* (1994), p. 582.

11. J. R. Mattox, S. J. Wagner, M. Malkan, *et al.*, Astrophys. J. **476**, 692 (1997).

12. A. Mecke, M. Pohl, P. Reich, *et al.*, Astron. Astrophys., Suppl. Ser. **120**, 541 (1996).

13. R. Mukherjee, D. L. Bertsch, S. D. Bloom, *et al.*, Astrophys. J. **490**, 116 (1997).

14. M. Pohl, in *Plasma Turbulence and Energetic Particles in Astrophysics,* Ed. by M. Ostrowski and R. Schlickeiser (Observ. Astron. Univ. Jangiellonski, Krakow, 1999), p. 311.

15. M. Pohl and R. Schlickeiser, Astron. Astrophys. **354**, 395 (2000).

16. W. Reich, H. Steppe, R. Schlickeiser, *et al.*, Astron. Astrophys. **273**, 65 (1993).

17. V. V. Savel'ev, Tu. M. Toropin, and V. M. Chechetkin, Astron. Zh. **73**, 543 (1996) [Astron. Rep. **40**, 494 (1996)].

18. C. von Montigny, D. L. Bertsch, J. Chiang, *et al.*, Astrophys. J. **440**, 525 (1995).

19. S. J. Wagner, Astron. Astrophys., Suppl. Ser. **120**, 495 (1996).

Translated by G. Rudnitskiĭ

A Hard X-ray Survey of the Galactic-Center Region with the IBIS Telescope of the INTEGRAL Observatory: A Catalog of Sources

M. G. Revnivtsev[1,2]*, R. A. Sunyaev[1,2], D. A. Varshalovich[3],
V. V. Zheleznyakov[4], A. M. Cherepashchuk[5], A. A. Lutovinov[1],
E. M. Churazov[1,2], S. A. Grebenev[1], and M. R. Gilfanov[1,2]

[1]*Space Research Institute, Russian Academy of Sciences, Profsoyuznaya ul. 84/32, Moscow 117810, Russia*

[2]*Max-Planck-Institut für Astrophysik, Karl-Schwarzschild-Str. 1, Postfach 1317, D-85741 Garching, Germany*

[3]*Ioffe Physicotechnical Institute, Russian Academy of Sciences, ul. Politekhnicheskaya 26,*
St. Petersburg, 194021 Russia

[4]*Institute of Applied Physics, Russian Academy of Sciences, ul. Ul'yanova 46, Nizhni Novgorod, 603600 Russia*

[5]*Sternberg Astronomical Institute, Universitetskiĭ pr. 13, Moscow, 119992 Russia*

Received January 15, 2004

Abstract—From August 23 through September 24, 2003, the INTEGRAL Observatory conducted a deep survey of the Galactic-Center region with a record-breaking sensitivity at energies above 20 keV. We have analyzed the images of the Galactic-Center region obtained with the ISGRI detector of the IBIS telescope (15−200 keV) and give a catalog of detected sources. We detected a total of 60 sources with fluxes above 1.5 mCrab, 44 and 3 of which were previously identified as binary systems of different classes in our Galaxy and as extragalactic objects, respectively. We discovered one new source. © *2004 MAIK "Nauka/Interperiodica"*.

Key words: *Galactic Center, hard X-ray sources.*

INTRODUCTION

Bright Galactic X-ray sources, which are mostly binary systems with accreting black holes or neutron stars, are strongly concentrated toward the Galactic plane and, in particular, toward the Galactic Center. Therefore, of great value in studying the population of bright compact objects in the Galactic-Center region are imaging instruments. X-ray images have long been reconstructed from the scans of sky regions made by collimated-field detectors, as, for example, those on UHURU (Forman *et al.* 1978), HEAO1 (Wood *et al.* 1984), etc. With the advent of grazing-incidence telescopes (EINSTEIN, ROSAT, CHANDRA, XMM), the angular resolution of X-ray images has improved greatly. However, such telescopes can presently operate only at energies below ∼10 keV.

Since X-ray photons with energies above 30 keV are very difficult to focus, an alternative imaging method, the principle of a coded aperture (see, e.g., Fenimore and Cannon 1978; Skinner *et al.* 1987a), is widely used for imaging in this energy range. A number of coded-aperture telescopes have yielded

interesting results, in particular, for the Galactic-Center region, for example, Spacelab2/XRT (Skinner *et al.* 1987b), MIR/KVANT/TTM (Sunyaev *et al.* 1990), GRANAT/ART-P (Pavlinsky *et al.* 1992, 1994), GRANAT/SIGMA (Cordier *et al.* 1991; Sunyaev *et al.* 1991); and BeppoSAX/WFC (Ubertini *et al.* 1999).

The most recent survey of the Galactic Center at energies above 40 keV was finished by the SIGMA telescope onboard the GRANAT orbital observatory more than five years ago. More than 5×10^6 s were spent on the observations of the Galactic Center, which provided a sensitivity in this field of 3−5 mCrab in the energy range 40−150 keV (Churazov *et al.* 1994). At present, using the IBIS telescope of the INTEGRAL observatory, we are able to repeat the hard X-ray survey of the Galactic Center with an appreciably better sensitivity in the energy range 20−150 keV.

In this paper, we analyze the data obtained with the IBIS telescope of the INTEGRAL observatory during a deep survey of the Galactic Center in August and September 2003 aimed at mapping this region and detecting pointlike X-ray sources. The
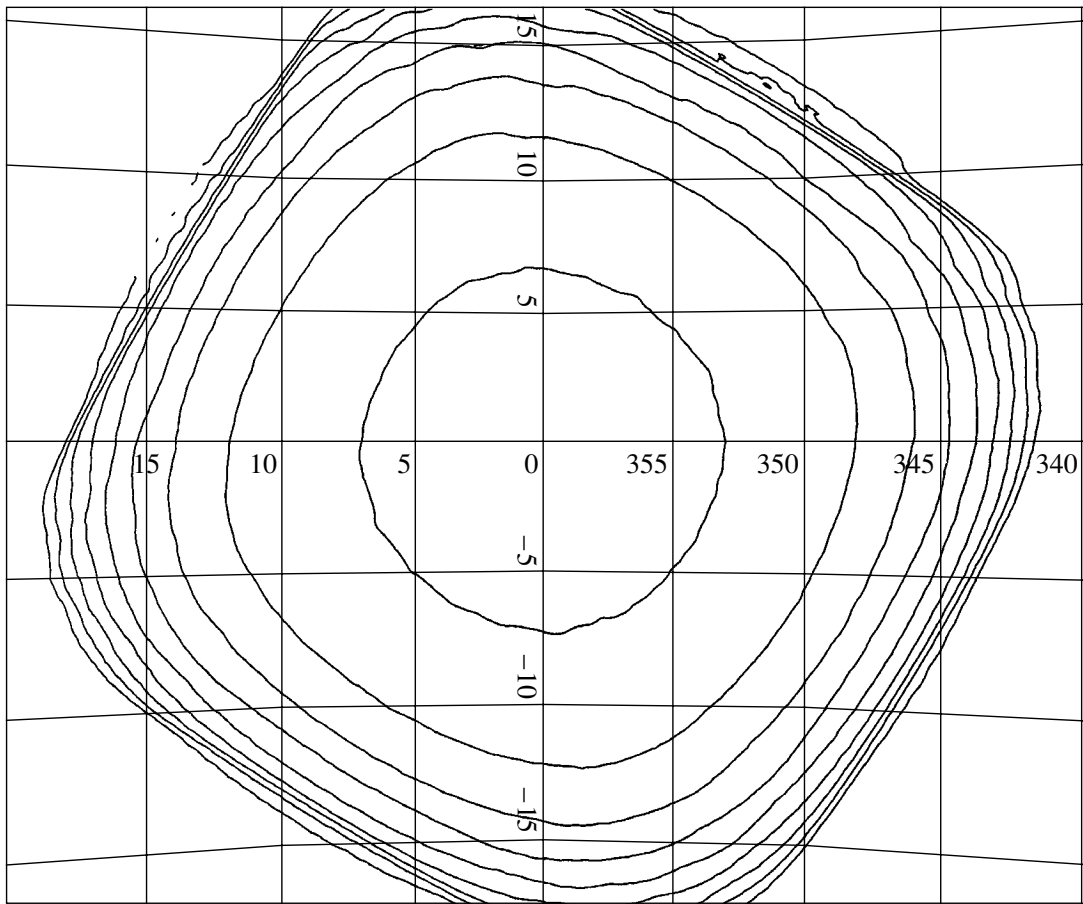
Fig. 1. Map of the sensitivity achieved with the observations used. The contours bound the regions in which the detection threshold is better than 1, 1.5, 2, etc. mCrab.

total exposure of the observations was approximately 2×10^6 s. A more detailed analysis of the radiation parameters for these objects will be carried out in ensuing papers.

DESCRIPTION OF THE INSTRUMENT AND DATA ANALYSIS

The INTEGRAL observatory (Winkler *et al.*, 2003) was launched into orbit by a russian PRO-TON carrier rocket on October 17, 2002 (Eismont *et al.* 2003). The observatory includes four telescopes, but in this paper we will use only data from the ISGRI detector of the IBIS telescope (Ubertini *et al.* 2003). This instrument gives the most favorable (for our purpose) combination of field of view, angular resolution, and sensitivity. The lower detector of the IBIS telescope (PICsIT) has a working energy range above 170 keV and, therefore, is much less sensitive to typical X-ray sources.

The IBIS telescope works on the principle of a coded aperture and can reconstruct the image of a chosen sky region in a $29° \times 29°$ field of view (the full coding region is $9° \times 9°$). The shadow structure on the ISGRI and PICsIT detectors is created by a tungsten mask. The ISGRI position-sensitive detector consists of 16 384 independent CdTe semiconductor pixels. A detailed description of the detector can be found in the paper by Lebrun *et al.* (2003).

The data of all our observations were processed as follows. For each individual observing session, the energies of the recorded events were calculated in accordance with the description of OSA 3.0 (Goldwurm *et al.* 2003) using the GAIN and RISETIME tables of versions 7 and 9, respectively. The events accumulated in the detector coordinates were filtered for the presence of "hot" or "dead" pixels, which led to the rejection of several percent of the detector pixels.

The raw detector images in the energy range 18–60 keV (which provided the best sensitivity to typical X-ray sources) were then regrouped into a new coordinate grid with a pixel size equal to 1/3 of the mask pixel size. This procedure results in an inevitable (although slight) deterioration of the spatial resolution

of the instrument, but it allows us to directly apply standard image reconstruction algorithms based on fast Fourier transform for the convolution operation. The detector images were transformed into sky images using the delta-decoding method (Fenimore and Cannon 1981; see also Skinner *et al.* 1987a). To take into account the spatially nonuniform detector background, we calculated the corresponding matrix of weights. The background used to calculate this matrix was obtained by analyzing a large set of observations, large enough for the contribution of individual pointlike X-ray sources to the result to be negligible.

To take into account the "ghosts" of pointlike sources that arose from incomplete coding, we used an iterative procedure of subtracting bright sources. The resulting images were coadded. The final map was convolved with a Gaussian whose width roughly corresponded to the actual spatial response function of the telescope; the latter is slightly broader than the ideal instrument response function because of the detector pixel regrouping effects and the addition of several images with different spatial orientations.

For calibration and for checking the validity and efficiency of the algorithm used, we performed a similar procedure for several observations of the Crab Nebula, which allowed us to directly compare the derived fluxes from the sources with the reference spectrum of the Crab Nebula.

An analysis of a large set of Crab-Nebula observations with the various positions of this source within the telescope's field of view shows that with the software used in this work, systematic uncertainties in the absolute values of the measured flux remain at a $\sim$10% level. The localization accuracy of the Crab Nebula is approximately $0\rlap{.}'4\,(1\sigma)$. For fainter sources, the localization accuracy decreases to $\sim$2–3′.

In analyzing the images, we considered the presence of a peak with an intensity exceeding a certain threshold as evidence of a pointlike source. The threshold was chosen by taking into account the fact that the systematic effects that can considerably raise the detection threshold relative to the purely statistical level remain in such a densely populated and bright field as the Galactic-Center region.

When the number of independent points on the image is taken into account, the statistical detection level in the field under consideration is on the order of 4σ, which can correspond to one spurious source in our field. In our analysis, we took the detection threshold to be 6.5σ to avoid the strong effect of systematic uncertainties. A sensitivity map for this choice of the detection threshold is shown in Fig. 1.

RESULTS

The table lists the detected sources together with their positions and fluxes in mCrabs. A flux of 1 mCrab in the energy range 18–60 keV corresponds to an energy flux of $\sim$1.4 × 10^{-11} erg s^{-1} cm^{-2} for a source with a power-law spectrum with the photon index $\Gamma = 2.1$. The localization accuracy of the sources in the table is approximately 2′–3′ (90% confidence).

Figure 2 shows the general image of a $\sim$35° × 25° field. In order not to overload the figure, not all the sources detected during our observations are labeled; a complete list is given in the table. A magnified image of the region immediately adjacent to the Galactic Center ($\sim$7° × 5°) constructed from INTE-GRAL/IBIS (18–60 keV) and MIR/KVANT/TTM (2–20 keV) data is shown in Fig. 3. The position of the dynamical Galactic center (the supermassive black hole Sgr A*) is indicated by the cross. Since the spatial resolution of the IBIS telescope is limited, we cannot separate the radiation from the object Sgr A* itself (for more detail, see Baganoff *et al.* 2003; Bélanger *et al.* 2003).

An analysis of the images of the Galactic-Center region in the energy range 18–60 keV with a typical sensitivity of 1–2 mCrab revealed a total of 60 sources. The nature of 51 of them is known; most of them (38 of 51) are low-mass X-ray binaries (LMXB). The majority of these low-mass systems are X-ray bursters (i.e., binaries with neutron stars that occasionally exhibit episodes of unstable nuclear burning on the neutron-star surface). However, the field also contains binary systems (GX5−1, GX9+1, GX9+1, GX340+0) with neutron stars whose accretion rates are high and the thermonuclear burning of the accreted material is steady (there are no bursts).

We detected five X-ray pulsars in the field of view: OAO1657−415, AXJ1749.2−2725, EXO1722−363, SAX J1802.7−2017, and GX1+4—which, except for the last, are members of high-mass X-ray binaries (HMXB)—and one anomalous X-ray pulsar (AXP), 1RXS J170849.0−40091.

Two sources (V1223 Sgr and V2400 Oph) are cataclysmic variables (CV), one source (Oph cluster = 4U 1708−23) is associated with a cluster of galaxies, one (GRS 1734−292) is associated with an active galactic nucleus, one (PKS 1830−211) is associated with a lensed blazar ($z \approx 2.5$), and one (SGR 1806−20) is associated with a soft GRB repeater.

Among the known binaries, only four (1E1740.7−2942, GRS 1758−258, SLX 1746−331, and IGR J17464−3213/H1743−31) contain compact objects that are candidate black holes (BHs).

List of sources detected during the deep survey of the Galactic Center in August and September 2003. The sources are arranged in order of decreasing significance of their detection

No.	α(2000)	δ(2000)	Flux (18−60 keV), mCrab[a]	σ	Identification	Class
1	255.978	−37.841	187.5 ± 0.3	662.5	4U1700−377	HMXB, NS
2	265.977	−29.746	74.8 ± 0.2	491.8	1E1740.7−2942	LMXB, BH
3	270.308	−25.748	78.0 ± 0.2	478.2	GRS 1758−258	LMXB, BH
4	277.370	−23.805	93.6 ± 0.2	392.4	GS1826−238	LMXB, NS
5	270.289	−25.080	42.7 ± 0.2	259.0	GX5−1	LMXB, NS
6	275.917	−30.367	32.3 ± 0.2	169.4	4U1820−303	LMXB, NS
7	256.424	−36.416	38.9 ± 0.2	160.5	GX349+2	LMXB, NS
8	261.887	−30.804	24.5 ± 0.2	151.6	4U1724−307 (Ter 2)	LMXB, NS
9	262.981	−33.831	22.9 ± 0.2	135.8	GX354−0	LMXB, NS
10	255.187	−41.658	59.7 ± 0.5	126.6	OAO1657−415	HMXB, NS
11	276.438	−37.113	29.0 ± 0.2	117.6	4U1822−371	LMXB, NS
12	263.354	−33.381	14.6 ± 0.2	88.4	RAPID BURSTER	LMXB, NS
13	266.991	−26.566	12.6 ± 0.2	81.7	GX3+1	LMXB, NS
14	270.387	−20.523	15.8 ± 0.2	77.2	GX9+1	LMXB, NS
15	266.519	−29.514	10.4 ± 0.2	69.3	A1742−294	LMXB, NS
16	264.560	−26.993	10.0 ± 0.2	64.4	SLX 1735−269	LMXB, NS
17	274.014	−14.037	37.3 ± 0.6	63.1	GX17+2	LMXB, NS
18	266.834	−30.010	7.6 ± 0.2	50.0	SLX1744−299/300	LMXB, NS
19	261.286	−36.280	9.5 ± 0.2	48.4	EXO 1722−363	HMXB?, NS
20	269.958	−22.019	8.6 ± 0.2	46.6	IGR/XTE J17597−2201	LMXB, NS
21	266.543	−32.235	7.2 ± 0.2	45.8	IGR J17464−3213/H1743-322	LMXB, BH?
22	264.729	−44.438	24.5 ± 0.6	43.9	4U1735−444	LMXB, NS
23	278.921	−32.995	10.9 ± 0.2	43.7	R1832−330 (NGC 6652)	LMXB, NS
24	256.540	−43.043	24.5 ± 0.6	43.6	4U1702−429	LMXB, NS
25	266.491	−28.923	6.2 ± 0.2	41.0	1E1742.8−2853	LMXB
26	257.290	−36.394	9.1 ± 0.2	39.4	IGR J17091−3624	?
27	266.404	−29.018	57.4 ± 0.2	37.9	AX J1745.6−2901	LMXB
28	266.580	−28.735	5.6 ± 0.2	37.3	1E1743.1−2843	LMXB
29	264.364	−29.137	5.3 ± 0.2	35.0	GRS1734−292	AGN
30	263.003	−24.747	5.7 ± 0.2	34.3	GX1+4	LMXB, NS
31	267.466	−33.192	5.4 ± 0.2	33.8	SLX 1746−331	LMXB?
32	262.905	−16.991	9.9 ± 0.3	31.7	GX9+9	LMXB, NS
33	257.210	−44.089	17.0 ± 0.7	25.9	4U1705−440	LMXB, NS
34	270.690	−20.272	4.8 ± 0.2	23.0	SAX J1802.7−2017	HMXB, NS
35	273.630	−17.149	7.6 ± 0.3	22.8	GX13+1	LMXB, NS

Table. (Contd.)

| No.	$\alpha(2000)$	$\delta(2000)$	Flux (18−60 keV), mCrab[a]	σ	Identification	Class
36	265.152	−28.303	3.4 ± 0.2	22.4	SLX 1737−282	LMXB
37	273.780	−12.103	23.8 ± 1.2	20.6	M1812−12	LMXB, NS
38	258.140	−23.334	4.2 ± 0.2	20.1	Oph cluster	Cluster of galaxies
39	267.511	−37.061	3.5 ± 0.2	18.1	4U1746−370 (NGC 6441)	LMXB, NS
40	257.528	−28.162	3.5 ± 0.2	18.1	XTEJ1710−281	LMXB
41	258.159	−24.232	3.2 ± 0.2	15.8	V2400 Oph	CV
42	266.261	−28.902	2.3 ± 0.2	15.4	GRS 1741.9−2853	LMXB, NS
43	266.868	−28.370	2.2 ± 0.2	14.8	IGR J17475−2822(new)[b]	?
44	261.317	−32.976	2.5 ± 0.2	14.8	1RXS J172525.5−325717	?
45	266.205	−29.352	2.1 ± 0.2	14.1	KS1741−293	LMXB, NS
46	274.652	−17.040	4.9 ± 0.4	13.6	SAX J1818.6−1703	LMXB?
47	264.802	−30.329	2.0 ± 0.2	13.1	IGR/XTE J17391−3021	HMXB?
48	272.148	−20.446	2.8 ± 0.2	12.8	SGR 1806−20	SGR
49	267.335	−27.511	1.9 ± 0.2	12.7	AX J1749.2−2725	HMXB, NS
50	267.828	−20.174	2.5 ± 0.2	12.2	1RXS J175113.3−201214	?
51	257.294	−32.302	2.4 ± 0.2	12.1	4U1705−32	?
52	258.073	−37.652	2.9 ± 0.2	12.0	SAX J1712.6−3739	LMXB, NS
53	278.379	−21.084	3.3 ± 0.3	10.8	PKS 1830−211	Blazar
54	260.027	−31.288	1.6 ± 0.2	9.2	1RXS J172006.1−311702	?
55	265.745	−36.345	1.7 ± 0.2	9.0	XTE J1743−363	?
56	251.452	−45.609	17.5 ± 1.9	9.0	GX340+0	LMXB, NS
57	283.722	−31.133	4.1 ± 0.5	8.8	V1223 Sgr	CV
58	266.590	−21.543	1.3 ± 0.2	7.0	1RXS J174607.8−213333	?
59	257.245	−40.111	2.2 ± 0.3	6.5	1RXS J170849.0−40091	AXP, NS
60[b]	268.585	−26.335	83.1 ± 2.0	30.0	IGR J17544−2619[c]	?

[a] Only the statistical flux uncertainties are given. The systematic uncertainty in the absolute flux value ($\sim$10%) is not included.

[b] The source lies at a distance of $0\overset{\circ}{.}7$ from the Galactic Center and may be a superposition of several weaker point like sources. Observations with a higher angular resolution are required to clarify this circumstance.

[c] The source was detected only in a short series of observations. The maximum flux and the maximum detection significance in individual observating sessions are listed.

Oph cluster

GX 9+9

V2400 Oph

GX 1+4

GX349+2

M1812−12

SLX 1735−269   4U1724−307

GX 9+1

IGR J17597−2201

GRS 1734−292   IGR J17091−3624   4U1700−37

GX 17+2

GX 13+1   OAO 1657−415

SAX J1802.7−2017   GX 3+1   1E1740.7−2942   GX354−0

20.0   15.0   10.0   5.0   0.0   355.0   350.0   345.0   340.0

GX 5−1   MXB 1730−333   EXO 1722−363   4U1702−429

GRS 1758−258   IGR J17464−3213

4U1705−440

SLX1746−331

GS1826−238   4U1746−370   4U1735−444

4U1820−303

R1832−330   4U1822−371

Fig. 2. Map of the Galactic-Center region averaged over the entire observing period. The energy range is 18–60 keV. The total exposure is ~2×10^{6} s.
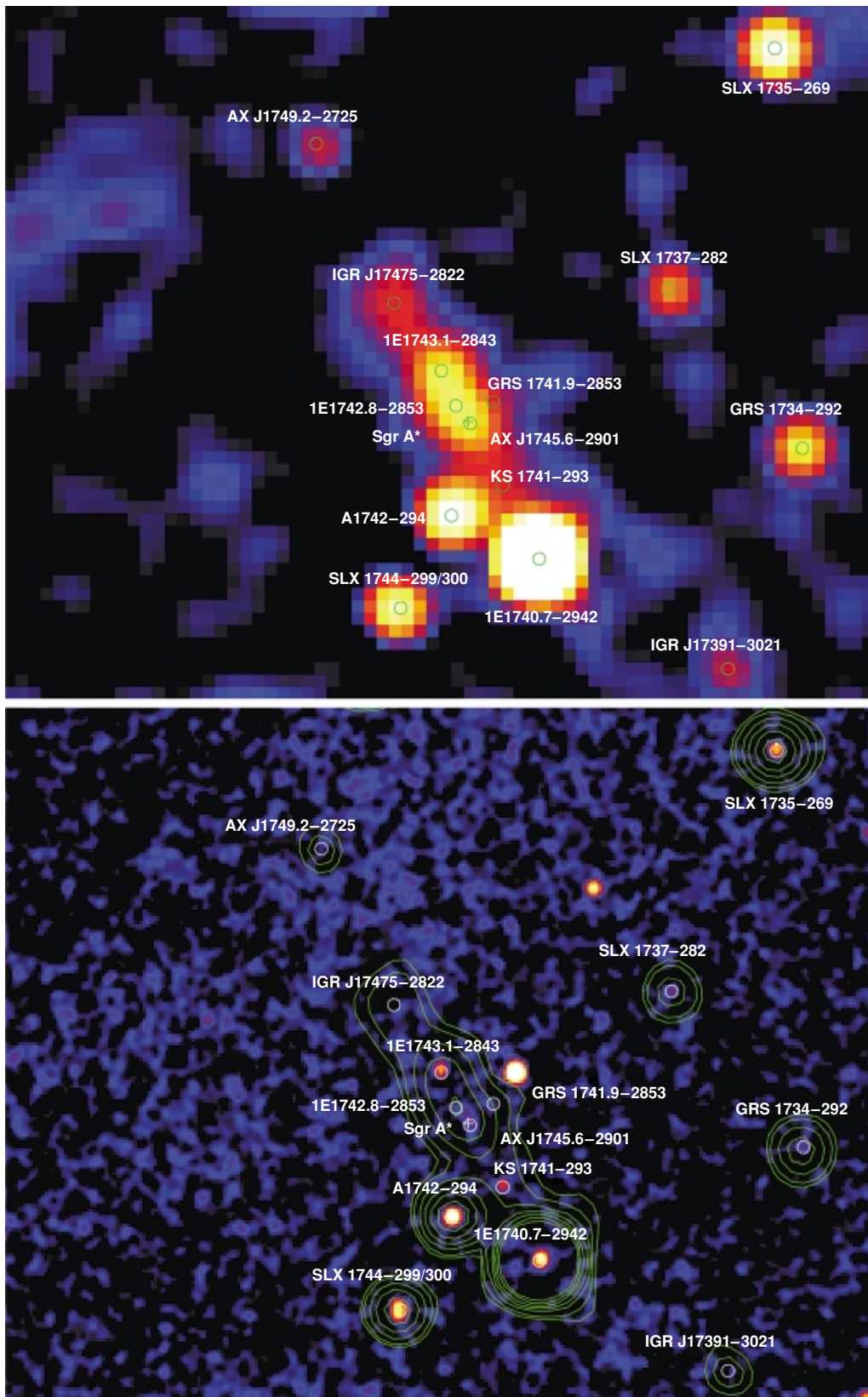
Fig. 3. Map of the region adjacent to the Galactic Center; (top) data from the IBIS telescope of the INTEGRAL observatory (energy range 18–60 keV), (bottom) data from the TTM telescope, the KVANT module of the MIR orbiting station (energy range 2–20 keV). The contours in the bottom panel are drawn over the IBIS image.

Five sources of those listed in the table were first detected by the INTEGRAL observatory; two (IGR J17544−2619, IGR J17475−2822) were found during the observations under consideration (see footnote [b] in the table). The object IGR J17544−2619 is a pronounced transient source that was observed only during a short period (Sunyaev *et al.* 2003; Grebenev *et al.* 2003); it is not detectable on the averaged image of the Galactic-Center region.

Thus, nine of the 60 sources detected during the deep survey of the Galactic Center have an unknown nature. The positions of four of these agree with those of the ROSAT sources.

ACKNOWLEDGMENTS

REFERENCES

1. F. Baganoff, Y. Maeda, M. Morris, *et al.*, Astrophys. J. **591**, 891 (2003).
2. G. Belanger, A. Goldwurm, P. Goldoni, *et al.*, Astron. Astrophys. (2003, in press); astro-ph/0311147.
3. E. Churazov, M. Gilfanov, R. Sunyaev, *et al.*, Astrophys. J., Suppl. Ser. **92**, 381 (1994).
4. B. Cordier, A. Goldwurm, P. Laurent, *et al.*, Adv. Space Res. **11**, 169 (1991).
5. N. A. Eismont, A. V. Ditrikh, G. Janin, *et al.*, Astron. Astrophys. **411**, 37 (2003).
6. E. E. Fenimore and T. M. Cannon, Appl. Opt. **17**, 337 (1978).
7. E. E. Fenimore and T. M. Cannon, Appl. Opt. **20**, 1858 (1981).
8. W. Forman, C. Jones, L. Cominsky, *et al.*, Astrophys. J., Suppl. Ser. **38**, 357 (1978).
9. A. Goldwurm, P. David, L. Foschini, *et al.*, Astron. Astrophys. **411**, 223 (2003).
10. S. Grebenev, A. Lutovinov, and R. Sunyaev, Astron. Telegram, No. 192 (2003).
11. F. Lebrun, J. P. Leray, P. Lavocat, *et al.*, Astron. Astrophys. **411**, 141 (2003).
12. M. N. Pavlinsky, S. A. Grebenev, and R. A. Syunyaev, Pis'ma Astron. Zh. **18**, 291 (1992) [Sov. Astron. Lett. **18**, 116 (1992)]; Pis'ma Astron. Zh. **18**, 570 (1992) [Sov. Astron. Lett. **18**, 228 (1992)].
13. M. Pavlinsky, S. Grebenev, and R. Sunyaev, Astrophys. J. **425**, 110 (1994).
14. G. K. Skinner, T. J. Ponman, A. P. Hammersley, and C. J. Eyles, Astrophys. Space Sci. **136**, 337 (1987a).
15. G. K. Skinner, A. P. Willmore, C. J. Eyles, *et al.*, Nature **330**, 544 (1987b).
16. R. A. Sunyaev, E. Churazov, V. Efremov, *et al.*, Adv. Space Res. **10**, 41 (1990).
17. R. Sunyaev, E. Churazov, M. Gilfanov, *et al.*, Astron. Astrophys. **247**, 29 (1991).
18. R. Sunyaev, S. Grebenev, A. Lutovinov, *et al.*, Astron. Telegram, No. 190 (2003).
19. P. Ubertini, A. Bazzano, M. Cocchi, *et al.*, Astrophys. Lett. Comm. **38**, 301 (1999).
20. P. Ubertini, F. Lebrun, G. Di Cocco, *et al.*, Astron. Astrophys. **411**, 131 (2003).
21. C. Winkler, T. J.-L. Courvoisier, G. Di Cocco, *et al.*, Astron. Astrophys. **411**, 1 (2003).
22. K. S. Wood, J. F. Meekins, D. J. Yentis, *et al.*, Astrophys. J., Suppl. Ser. **56**, 507 (1984).

Translated by G. Rudnitskiĭ

Spatial Correlation of Unidentified Gamma-Ray Sources with Flaring and Wolf−Rayet Stars

A. M. Galper[*] and B. I. Luchkov

Moscow Engineering Physics Institute, Kashirskoe sh. 31, Moscow, 115409 Russia
Received November 22, 2002; in final form, December 15, 2003

Abstract—The spatial positions of unidentified gamma-ray sources ($E > 100$ MeV) were analyzed. This analysis shows that gamma-ray sources with fluxes $>5 \times 10^{-7}$ cm^{-2} s^{-1} correlate with Wolf−Rayet stars, while gamma-ray sources with fluxes $<5 \times 10^{-7}$ cm^{-2} s^{-1} may be associated with flaring stars. © 2004 MAIK "Nauka/Interperiodica".

Key words: *unidentified gamma-ray sources, flaring stars, Wolf−Rayet stars.*

INTRODUCTION

The studies of cosmic gamma-ray emission at energies of tens and hundreds of MeV performed with the COS-B (Swanenburg *et al.* 1981), EGRET (Thomson *et al.* 1995), and COMPTEL (Schonfelder *et al.* 1993) orbital telescopes have revealed a large number of stationary and variable sources. At present, about 300 sources are known in this energy range (Macomb and Gehrels 1999); their angular sizes do not exceed the transfer function of the telescope and are, therefore, considered to be point sources. The sources have been localized in the sky with an accuracy of about 1°. Only a small fraction of them have been identified with known objects (pulsars, supernova remnants, and active galactic nuclei). The nature of the remaining sources is not yet unknown; they cannot be accurately identified, because the angular accuracy of the measurements is relatively low.

In this paper, we compare the celestial distributions of unidentified gamma-ray sources (UGRSs) with energies $E > 100$ MeV from the catalog by Macomb and Gehrels (1999) and some of the types of active stars. Of course, such an analysis cannot be a substitute for the accurate identification of gamma-ray sources, but it can reveal some of the features of and, possibly, indicate one way of searching for their counterparts.

Figure 1 shows the celestial maps (in Galactic coordinates) of UGRSs constructed mainly from EGRET data for bright ($F > 5 \times 10^{-7}$ phot. cm^{-2} s^{-1}) and faint ($F < 5 \times 10^{-7}$ phot. cm^{-2} s^{-1}) sources. As we see from the figure, the spatial distributions of

bright and faint gamma-ray sources differ markedly from one another, which probably indicates that they have different origins and, accordingly, different optical counterparts. Three UGRS components can be identified in these distributions:

(i) an isotropic component consisting of sources uniformly distributed over the sky (Fig. 1b); these sources may be associated with both nearby Galactic and extragalactic objects;

(ii) a chain of sources located near the Galactic equator (Fig. 1a);

(iii) extended groups of sources near the Galactic center and anticenter (Figs. 1a and 1 b), the statistical significance of which is low.

The latter two components strongly suggest that the UGRSs belong to the Galaxy, which gives grounds for the subsequent analysis—a comparison of the constructed gamma-ray maps with the distribution of active stars in the Galaxy. We considered the following two known populations of active stars as possible UGRS counterparts: flaring stars (Gershberg 1978) and Wolf−Rayet (WR) stars (Van der Hacht 2001).

FLARING STARS

These are young low-mass K- and M-type stars exhibiting flares (similar to solar flares, but longer and more powerful) that result from the reconnection of magnetic field lines and the release of magnetic-field energy. Stars of this type show high rotational velocities and anomalous abundances of light elements (lithium, beryllium), indicative of the high rate of nucleosynthesis reactions in the stellar atmospheres. Since flaring stars are difficult to observe, their catalogs are incomplete (especially in the Southern
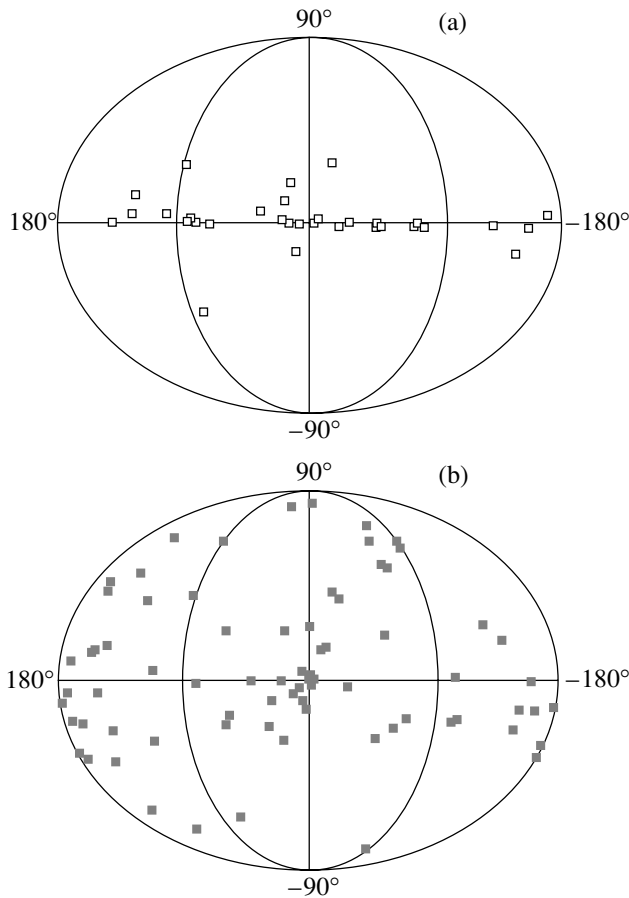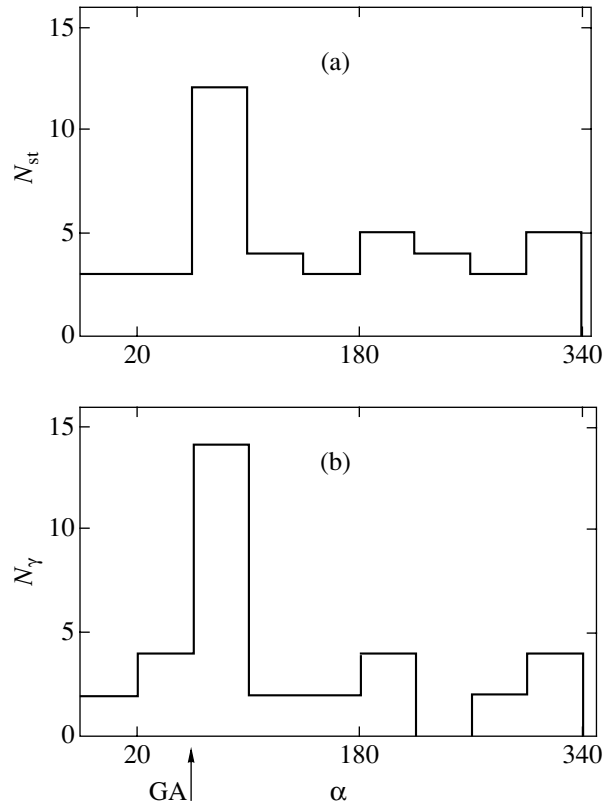
Fig. 1. Galactic coordinate maps of unidentified gamma-ray sources ($E \geq 100$ MeV): (a) bright ($F \geq 5 \times 10^{-7}$ phot. cm^{-2} s^{-1}) and (b) faint ($F \leq 5 \times 10^{-7}$ phot. cm^{-2} s^{-1}) sources.

Fig. 2. Right-ascension distributions of flaring stars ($r \geq 10$ pc) (a) and faint UGRSs (b) in the Northern Hemisphere. The arrow indicates the position of the Galactic anticenter (GA).

Hemisphere) and contain only nearby objects (within 50 pc). The enhanced activity of flaring stars suggests that they are very likely candidates for identification with UGRSs.

Figure 2 shows the results of our comparative analysis of the distributions of UGRSs and flaring stars in the Northern Hemisphere (Gershberg 1978). There is a correlation for flaring stars with parallaxes $\pi < 0.1$ (heliocentric distances $r > 10$ pc) and faint gamma-ray sources: both distributions have a noticeable peak in the range $\alpha = 60°-100°$ (the region of the Galactic anticenter). This grouping of flaring stars and the accompanying UGRSs may originate from the Orion spiral arm, the nearest to the Sun, where the star-formation rate is high.

As we see from Fig. 1a, bright UGRSs show no correlation with flaring stars. Bright UGRSs should be attributed to more distant active stars, for example, WR stars.

WOLF−RAYET STARS

WR stars, which are high-mass O- and B-type stars with strong (optically thick, high-velocity) stellar winds at the final stage of stellar evolution before a supernova explosion (Cherepashchuk 2001), can undoubtedly also be considered as candidates for stellar UGRS counterparts. WR stars are formed in the Galactic spiral arms, where gas has been preserved in sufficient amounts and star formation goes on. For this reason, none of these objects are present in the solar neighborhood; they are distributed within a narrow band $|b| < 10°$ and strongly concentrated toward the equator: their mean Galactic latitude is $b = 1°.3$ and $b = -1°.7$ for $b > 0$ and $b < 0$, respectively. Bright UGRS are also concentrated toward the Galactic equator (Fig. 1a).

A more detailed analysis shows that the similarity between the distributions of bright UGRSs and WR stars is not accidental.

We considered cases of close positions (coincidences) of WR stars and UGRSs (within the angular accuracy of the latter, 1°) in the band $|b| < 2°$, where the bulk of the WR-stars are concentrated. The number of coincidences was found to be relatively

Coordinates of UGRSs: possible locations to search for WR stars

l	b
7°.5	−2°.5
13.6	0.6
17.4	2.4
65.7	0
75.3	−1.2
78.1	2.1
313.3	0.3
333.5	1.0
358.7	−1.3
358.8	1.7

large: 12 of the 20 UGRSs within this band coincided with WR stars, yielding an observed probability of $P = 0.60 \pm 0.11$. The accuracy of the coincidences is rather high: the mean coordinate differences between the coincident UGRSs and WR stars are $\Delta l = 0°.5$ and $\Delta b = 0°.4$. The area of coincidence is $s = \Delta l \Delta b = 0.2$ sq. deg, whereas the area per one WR star (their number is 152 in the band under consideration) is $S_{WR} = 6.3$ sq. deg. Consequently, the expected probability of coincidence is $P_{ch} = 0.03$. The discrepancy of 5 standard deviations between the observed (P) and expected (P_{ch}) probabilities is too large to be attributable to random fluctuations (the corresponding probability is $\approx 10^{-6}$).

The main result of our analysis is that active stars can actually be discrete high-energy gamma-ray sources. The positions of bright UGRSs often coincide with those of WR stars, whereas faint UGRSs show a correlation with flaring stars. These active stars are probably not the only UGRS counterparts. The search for alternative counterparts (pulsars, other types of eruptive stars) should be continued.

The following conclusion may be considered as a secondary but important conclusion of our analysis: "strong" UGRSs along the Galactic equator with no WR stars found in their vicinity can serve as a guide for a more thorough search (within the localization accuracy, $\approx 1°$). The corresponding locations are listed in the table.

ACKNOWLEDGMENTS

REFERENCES

1. A. M. Cherepashchyuk, Astron. Zh. **38**, 145 (2001).
2. R. E. Gershberg, *Flaring Low-Mass Stars* (Nauka, Moscow, 1978) [in Russian].
3. D. J. Macomb and N. Gehrels, Astrophys. J., Suppl. Ser. **120**, 335 (1999).
4. V. Schonfelder, K. Bennett, H. Aarts, *et al.*, Astrophys. J., Suppl. Ser. **86**, 657 (1993).
5. B. N. Swanenburg, K. Bennett, J. F. Bignami, *et al.*, Astrophys. J. Lett. **243**, L69 (1981).
6. D. J. Thompson, D. L. Bertsch, B. L. Dingus, *et al.*, Astrophys. J., Suppl. Ser. **102**, 259 (1995).
7. K. A. Van der Hacht, New Astron. Rev. **45**, 135 (2001).

Translated by A. Dambis

Influence of Accelerated Particles on the Large-Scale Magnetic Field in Young Supernova Remnants

I. N. Toptygin[*]

St. Petersburg State Technical University, ul. Politekhnicheskaya 29, St. Petersburg, 195251 Russia

Received December 17, 2003

Abstract—We offer a possible explanation for the observational data on the magnetic-field structure in young supernova remnants (SN 1006, Tycho, Kepler, Cas A) that have been obtained by analyzing the polarizations of electromagnetic radiation in the radio, infrared, and other wavelength ranges. The authors of observational works interpret these data as evidence that the ordered magnetic-field component is predominantly radial, but it can be much smaller in amplitude than the stochastic field component that accounts for the bulk of the total magnetic energy. We calculate the magnetic field in supernova remnants by taking into account the shock compression of the primary field and the generation of a large-scale magnetic field by the particles accelerated at the shock front. The assumption that the field in the supernova remnant is the explosion-compressed primary field near the star is inconsistent with observational data, because the tangential (relative to the shock front) field component perpendicular to the radius must prevail in this case. However, allowing for the generation of an additional magnetic field by the electric current of the particles accelerated by a strong shock front leads us to conclude that the field components parallel to the front are suppressed by accelerated particles by several orders of magnitude. Only the component perpendicular to the front remains. Such a field configuration for uniform injection does not lead to the generation of an additional magnetic field, and, in this sense, it is stable. This explains the data on the radial direction of the ordered field component. As regards the stochastic field component, we show that it is effectively generated by accelerated particles if their injection into acceleration at the shock front is nonuniform along the front. Injection nonuniformity can be caused by upstream density nonuniformities. A relative density nonuniformity of the order of several percent is enough for an observable magnetic field with scales on the order of the density nonuniformity scales to be generated. © *2004 MAIK "Nauka/Interperiodica".*

Key words: *supernova remnants, particle acceleration, radiation polarization, magnetic field.*

INTRODUCTION AND FORMULATION OF THE PROBLEM

The polarization of electromagnetic radiation from supernova remnants (SNRs) has now been measured with a high spatial resolution. Reynolds and Gilmore (1993) investigated the polarization of radio emission from SNR 1006 at frequencies $\nu = 1370$ and 1665 MHz (wavelengths of 18 and 22 cm) with an angular resolution as high as 24 arcsec, which corresponds to the spatial resolution of regions with sizes of less than 0.2 pc at the assumed distance (1.7 kpc). The authors found a polarization of $\sim 11\%$ from the brightest SNR regions. The spectral index of the radio emission from this SNR had been previously estimated to be $\alpha = 0.6$, which corresponds to the index of the energy spectrum $\gamma = 2.2$ for relativistic electrons and confirms the synchrotron nature of the emission. Linear polarization of the emission suggests the presence of a regular quasi-uniform field

in SNRs. In the absence of a regular field, the polarization would be zero. If the entire magnetic field is uniform, then the polarization Π of the emission from electrons with a power-law spectrum does not depend on frequency and is determined by the spectral index (Ginzburg and Syrovatskiĭ 1963) $\Pi = (\gamma + 1)/(\gamma + 7/3) \approx 71\%$ for the conditions under consideration.

However, observational data show that the polarization from telescope-resolvable regions (less than 0.2 pc) is several times lower than the expected polarization for a uniform magnetic field. The authors interpret this as evidence that, in addition to the regular magnetic-field component, there is also a disordered field component on these scales. A similar pattern (but with a lower resolution) is observed in other young SNRs: Kepler ($\Pi \approx 4\%$ at $\nu = 5$ GHz; Matsui *et al.* 1984) and Tycho ($\Pi \approx 10-15\%$ at $\nu = 5$ GHz; Duin and Strom 1975; Dickel *et al.* 1991). For SNR Cassiopeia A, Down and Thomson (1972) measured $\Pi \approx 17\%$ at frequency $\nu = 3.1$ GHz; Jones *et al.* (2003) performed measurements at frequencies

[*]E-mail: `cosmos@IT10242.spb.edu`

of 5 GHz and 1.36×10^5 GHz ($\lambda = 2.2\ \mu$m). In both cases, the polarizations were comparable in magnitude and equal to $\Pi \approx 4-10\%$. Thus, in all cases, the polarization proved to be several times lower than might be expected for a quasi-uniform magnetic field; the regular field component is radial in most cases.

As regards the magnetic field, these data require an explanation of the following two main points:

(i) Why is the regular field radial, although the simple assumption regarding the shock compression of the primary field leads to a severalfold enhancement of the tangential component, but not the component normal to the front?

(ii) What is the origin of the stochastic but large-scale ($l \leq 0.2$ pc) field that causes the polarization of the synchrotron radiation to decrease severalfold?

Using most of the available data, Reynolds and Gilmore (1993) estimated the energy of the disordered field to be a factor of 4 to 5 higher than the energy of the regular field component. To explain the stochastization of the primary field that existed in the vicinity of the presupernova, the authors invoked Rayleigh−Taylor instability, which was considered for SNRs by Gull (1973), Dickel *et al.* (1989), and several other authors. However, this explanation cannot be considered to be natural. The conditions for the growth of Rayleigh−Taylor instability are not satisfied at the strongest primary SNR shock front if this front propagates through a homogeneous medium. For example, the presence of clouds with significant overdensities (Jun and Jones 1999) is needed for the required instability to emerge. Models that assume the dominance of the ejected envelope in the SNR can evidently chain to describe only the initial SNR expansion phase and are inapplicable at the Sedov phase, when the SNR mass is much larger than the ejection mass. In addition, in the models with the regular primary field destroyed by Rayleigh−Taylor instability, the field must be ordered again at the subsequent phase to explain the presence of an observable radial regular field component. The qualitative reasoning by Duin and Strom (1975) about the possibility of such ordering in the Sedov model cannot be considered as conclusive.

In our opinion, the addition of another source of magnetic-field generation, the electric current of the particles accelerated at the primary shock front, can provide a more plausible explanation for the observed properties of the radio emission from young SNRs. During intensive acceleration, energy that accounts for several tens of percent of the gasdynamic flow energy can be transferred to relativistic particles (Axford *et al.* 1978; Krymskiĭ 1981; Völk and McKenzie 1982). If part of this energy is transformed into magnetic energy, then the field will be strong enough to explain many observed phenomena. The possibility

of magnetic-field generation by accelerated particles depends significantly on the symmetry properties (i.e., anisotropy and inhomogeneity) of the medium (Dolginov and Toptygin 2003; Dolginov *et al.* 2004). The latter authors have shown that the particles accelerated at a strong shock front in the case of their uniform injection at the front into acceleration produce a secondary field that suppresses the primary field component tangential to the front. Under these conditions, only the field component normal to the front (i.e., radial for a quasi-spherical SNR) remains upstream and downstream of the shock front. This effect explains the presence of an ordered radial field component in young SNRs. There are strong shock fronts and particle acceleration in these SNRs, as suggested by the synchrotron radiation over a wide frequency range. Therefore, the generation of a magnetic field by accelerated particles is highly likely.

The suggested mechanism can also account for the presence of a large-scale ($l \leq 0.2$ pc; Reynolds and Gilmore 1993) disordered magnetic field. It can be generated by the current of accelerated particles during their nonuniform injection into acceleration. Injection nonuniformity can be produced by density nonuniformities upstream of the front. A density nonuniformity of no more than a few percent, which can be produced by linear low-amplitude perturbations in the absence of Rayleigh−Taylor instability, will suffice to generate fields of observable strength ($\sim 10^{-5}$ G).

In this paper, we have performed calculations to substantiate the picture outlined above. In the next section, based on the Sedov self-similar solution, we find a self-similar solution for the magnetic field in a SNR. The solution applies to the general case where a primary static magnetic field of arbitrary structure existed in the SNR expansion region. Subsequently, we analyze the field structure in the SNR and the changes made by an allowance for the secondary field generated by particles. We consider the case of weakly nonuniform injection of accelerated particles. We calculate the field generated by these particles, its geometry and magnitude under typical conditions and discuss the polarization of the radiation. We show that the ratio of the energies of the regular and stochastic magnetic-field components cannot be reliably estimated from the available observational data. Our conclusions are formulated in the final section.

THE LARGE-SCALE FIELD IN A SUPERNOVA REMNANT

If the magnetic field is ignored, then the self-similar solutions for a central explosion in a homogeneous or spherically symmetric medium are spherically symmetric; i.e., the plasma velocity is perpendicular to the front. In the presence of a magnetic

field, tangential velocity components will emerge in accordance with the boundary conditions in the frame of the front,

$$j\{\mathbf{v}_t\} = \frac{B_n}{4\pi}\{\mathbf{B}_t\}, \qquad B_n\{\mathbf{v}_t\} = j\{V\mathbf{B}_t\}, \quad (1)$$

where $j = \rho_0 v_s = v_s/V_0$ is the density of the mass flux through the front, V_0 is the specific volume of the upstream matter, and v_s is the velocity of the upstream matter, which is equal in magnitude to the velocity of the shock front relative to the stationary medium. The braces denote the jump in the corresponding quantity at the front. Introducing the Alfvén velocity $\mathbf{v}_A = \mathbf{B}/\sqrt{4\pi\rho_0}$ and the Alfvén Mach numbers $M_{An} = v_s/v_{An}$ and $M_{At} = v_s/v_{At}$, we obtain an estimate of $v_t/v_s \approx (M_{An}M_{At})^{-1}$ from the first equation in (1). Thus, the deviation from spherical symmetry for a strong shock is $M_A^{-2} \ll 1$. Disregarding these terms, we find the boundary conditions at a strong shock front

$$B_n^s = B_n^0, \qquad B_t^s = B_t^0 \frac{\rho_s}{\rho_0}, \qquad (2)$$

where the index s denotes the values of the quantities in the perturbed region on the inside of the front. For a strong shock front in plasma, $\sigma = \rho_s/\rho_0 \geq 4$; values larger than 4 can be reached through a significant number of relativistic particles.

The Reynolds magnetic number in SNRs is very large: $\mathrm{Re}_m = ul/\nu_m \approx 10^9$ if $u \approx 3 \times 10^8$ cm s^{-1} (Lozinskaya 1986), the scale length of the motion is $l \approx 1$ pc, and the magnetic viscosity is $\nu_m \approx 10^{18}$ cm^2 s^{-1} (Ruzmaǐkin $et\ al.$ 1988). Therefore, the dissipation-free approximation may be used to calculate the field,

$$\frac{\partial \mathbf{B}}{\partial t} = \nabla \times [\mathbf{u} \times \mathbf{B}], \quad \nabla \cdot \mathbf{B} = 0. \qquad (3)$$

Below, we assume that the velocity in the perturbed region ($r < R_s(t)$, where $R_s(t)$ is the front radius) is directed radially and does not depend on the angles: $u_r = u(r,t)$, $u_\vartheta = u_\alpha = 0$. Equations (3) may be written as

$$\frac{\partial B_r}{\partial t} = -\frac{u(r,t)}{r^2}\frac{\partial}{\partial r}r^2 B_r, \quad \frac{\partial B_\vartheta}{\partial t} = -\frac{1}{r}\frac{\partial}{\partial r}ru(r,t)B_\vartheta, \qquad (4)$$

$$\frac{\partial B_\alpha}{\partial t} = -\frac{1}{r}\frac{\partial}{\partial r}ru(r,t)B_\alpha.$$

The general solution of these equations can be easily found if the function $u(r,t)$ is factorized: $u(r,t) = p(r)q(t)$. Introducing new dependent variables,

$$b_r(r,t,\vartheta,\alpha) = r^2 B_r(r,t,\vartheta,\alpha), \qquad (5)$$
$$b_\vartheta(r,t,\vartheta,\alpha) = rp(r)B_\vartheta(r,t,\vartheta,\alpha),$$
$$b_\alpha(r,t,\vartheta,\alpha) = rp(r)B_\alpha(r,t,\vartheta,\alpha)$$

and new independent variables,

$$\tau(t) = \int q(t)dt, \qquad s(r) = \int \frac{dr}{p(r)}, \qquad (6)$$

we verify that all of Eqs. (4) take the same form

$$\frac{\partial b_i}{\partial \tau} + \frac{\partial b_i}{\partial s} = 0, \qquad i = r, \vartheta, \alpha. \qquad (7)$$

The solutions of these equations are arbitrarily differentiable functions $b_i(\varphi, \vartheta, \alpha)$ of the self-similar variable $\varphi(r,t) = s(r) - \tau(t)$. Of course, this self-similar variable differs from the Sedov self-similar variable $r/R_s(t)$. The dependence of b_i on φ can be determined from the boundary conditions if the primary field is time-independent. The dependence on ϑ and α can also be determined from the boundary conditions and from the second equation of system (3).

In the Sedov solution, for a pointlike explosion in a homogeneous medium,

$$R_s(t) = \beta\left(\frac{Et^2}{\rho_0}\right)^{1/5}, \qquad (8)$$

where $\beta \approx 1$ is a dimensionless factor, E is the total mechanical energy of the explosion (Sedov 1972), and the derivative $\dot{R}_s(t) = v_s(t)$ is the front velocity. The velocity field downstream of the front of a blast wave can be well (to within a few percent) fitted by a linear function of the radius:

$$u(r,t) = \mu\frac{r\dot{R}_s(t)}{R_s(t)}, \qquad \mu = 1 - \sigma^{-1}. \qquad (9)$$

Here, σ is the compression ratio of the matter at the front introduced above. Formulas (8) and (9) are also valid when there are relativistic particles and $\sigma > 4$ (Toptygin 2000). If the acceleration is weak, then $\sigma = (\gamma + 1)/(\gamma - 1) = 4$, where $\gamma = 5/3$ in a nonrelativistic plasma. In this case, $\mu = 2/(\gamma + 1)$, and (9) at $r = R_s$ yields the Sedov boundary condition for the velocity at the front (Sedov 1972).

Using (8) and (9), we obtain

$$p(r) = r, \quad q(t) = \frac{\mu\dot{R}_s(t)}{R_s(t)}, \qquad (10)$$

$$\varphi(r,t) = \ln\left(\frac{r}{R_s^\mu(t)}\right).$$

Clearly, without loss of generality, we may take the following quantity as the self-similar variable:

$$\xi(r,t) = e^{\varphi(r,t)} = \frac{r}{R_s^\mu(t)}. \qquad (11)$$

We use this quantity below and write the solution using (5) and (10) as

$$B_i(r,t,\vartheta,\alpha) = \frac{1}{r^2}b_i(\xi(r,t),\vartheta,\alpha). \qquad (12)$$

In writing the boundary conditions at the moving front, we should take into account the dependence of the initial magnetic field $\mathbf{B}_0$ in the SNR expansion region on the radius and the angles. For this purpose, it is convenient to expand this field into a complete system of vector spherical functions—spherical vectors (see Berestetskiĭ *et al.* 1989):

$$\mathbf{B}_0(r,\vartheta,\alpha) = \sum_{lmk} a_{lm}^{(k)}(r)\mathbf{Y}_{lm}^{(k)}(\vartheta,\alpha). \quad (13)$$

Here,

$$\mathbf{Y}_{lm}^{(1)}(\vartheta,\alpha) = [l(l+1)]^{-1/2}\nabla_{\vartheta\alpha}Y_{lm}(\vartheta,\alpha), \quad (14)$$

$$\mathbf{Y}_{lm}^{(3)}(\vartheta,\alpha) = \mathbf{n}Y_{lm}(\vartheta,\alpha),$$

$$\mathbf{Y}_{lm}^{(2)}(\vartheta,\alpha) = [l(l+1)]^{-1/2}\hat{\mathbf{l}}Y_{lm}(\vartheta,\alpha), \quad (15)$$

$$l = 1,2,\ldots, \quad \mathbf{Y}_{00}^{(1)} = \mathbf{Y}_{00}^{(2)} = 0,$$

where $\mathbf{n} = \mathbf{r}/r$, $\hat{\mathbf{l}} = -i\mathbf{n}\times\nabla_{\vartheta\alpha}$, $\nabla_{\vartheta\alpha}$ is the angular part of the gradient operator, and $Y_{lm}(\vartheta,\alpha)$ are the Legendre spherical functions. The spherical vectors form a complete orthonormal system of functions:

$$\int \mathbf{Y}_{l'm'}^{(k')*}(\vartheta,\alpha)\cdot\mathbf{Y}_{lm}^{(k)}(\vartheta,\alpha)d\Omega = \delta_{ll'}\delta_{mm'}\delta_{kk'}. \quad (16)$$

The spherical vectors are directed along the radius for $k = 3$ and perpendicular to the radius for $k = 1,2$. Therefore, for the normal and tangential (to the front) components of the field $\mathbf{B}_0$ at $r = R_s(t)$, the expansions are

$$\mathbf{B}_{0n} = \sum_{lm} a_{lm}^{(3)}(R_s(t))\mathbf{Y}_{lm}^{(3)}(\vartheta,\alpha), \quad (17)$$

$$\mathbf{B}_{0\tau} = \sum_{lm,k=1,2} a_{lm}^{(k)}(R_s(t))\mathbf{Y}_{lm}^{(k)}(\vartheta,\alpha).$$

Let us write solution (12) at the front ($r = R_s(t)$, $\xi = R_s^{1/\sigma}(t)$) as similar expansions:

$$\mathbf{B}_r^s = \frac{1}{R_s^2(t)}\sum_{lm} b_{lm}^{(3)}(R_s^{1/\sigma}(t))\mathbf{Y}_{lm}^{(3)}(\vartheta,\alpha), \quad (18)$$

$$\mathbf{B}_\tau^s = \frac{1}{R_s^2(t)}\sum_{lm,k=1,2} b_{lm}^{(k)}(R_s^{1/\sigma}(t))\mathbf{Y}_{lm}^{(k)}(\vartheta,\alpha).$$

Using the boundary conditions (2), we find a relationship between the functions $b_{lm}^{(k)}$ and $a_{lm}^{(k)}$:

$$b_{lm}^{(k)}(R_s^{1/\sigma}) = \sigma R_s^2 a_{lm}^{(k)}(R_s), \quad k = 1,2; \quad (19)$$

$$b_{lm}^{(3)}(R_s^{1/\sigma}) = R_s^2 a_{lm}^{(3)}(R_s).$$

These equations have a structure of the type $f(x^{1/\sigma}) = F(x)$, where $F(x)$ and $f(x)$ are the known and unknown functions, respectively. We have $f(x) =$

$F(x^\sigma)$ and find the magnetic field in the cavity $r \leq R_s(t)$ for the general case using (12), (17), and (19):

$$\mathbf{B}_r = \left(\frac{r}{R_s}\right)^{2\sigma-2}\sum_{lm} a_{lm}^{(3)}(r^\sigma/R_s^{\sigma-1})\mathbf{Y}_{lm}^{(3)}(\vartheta,\alpha), \quad (20)$$

$$\mathbf{B}_\tau = \sigma\left(\frac{r}{R_s}\right)^{2\sigma-2}\sum_{lm,k=1,2} a_{lm}^{(k)}(r^\sigma/R_s^{\sigma-1})\mathbf{Y}_{lm}^{(k)}(\vartheta,\alpha).$$

Let us now consider the most important special cases.

(1) A **uniform field $\mathbf{B}_0$** in the vicinity of a supernova. In the cavity,

$$B_r(r,t,\vartheta) = B_0\left(\frac{r}{R_s(t)}\right)^{2\sigma-2}\cos\vartheta, \quad (21)$$

$$B_\vartheta(r,t,\vartheta) = -\sigma B_0\left(\frac{r}{R_s(t)}\right)^{2\sigma-2}\sin\vartheta, \quad r \leq R_s(t).$$

At $\sigma = 4$, we obtain $2\sigma - 2 = 6$. Thus, the radial magnetic field is swept up from the explosion region together with plasma; the attenuation factor is $(r/R_s(t))^6$. The tangential field is also swept up, but it is enhanced at the front by a factor $\sigma \geq 4$ compared to its unperturbed value. Therefore, the tangential field dominates in the cavity. Solution (21) is inapplicable in the central part of the cavity, because the heat conduction and the ejection of mass Δm from the star are disregarded in the Sedov solution. It appears that (21) faithfully describes the field at distances

$$r > R_0 = (3\Delta m/4\pi\rho_0)^{1/3}, \quad (22)$$

when the swept-up mass is on the order of or larger than the mass of the ejected envelope.

(2) The presupernova produced a **dipole field** in the surrounding space $r > a$,

$$B_{0r}(r,t,\vartheta) = \frac{2M\cos\vartheta}{r^3}, \quad B_{0\vartheta}(r,t,\vartheta) = \frac{M\sin\vartheta}{r^3}, \quad (23)$$

$$B_{0\alpha}(r,t,\vartheta) = 0.$$

The field inside the star ($r < a$) is nondipolar and nonsingular. The general solution (20) for this case takes the form

$$B_r(r,t,\vartheta) = \frac{2M\cos\vartheta}{r^3}\left(\frac{R_s(t)}{r}\right)^{\sigma-1}, \quad (24)$$

$$B_\vartheta(r,t,\vartheta) = \frac{\sigma M\sin\vartheta}{r^3}\left(\frac{R_s(t)}{r}\right)^{\sigma-1},$$

$$B_\alpha(r,t,\vartheta) = 0,$$

where M is the magnetic dipole moment of the star. This solution formally yields a large increase of the field with time at any distance from the explosion center for $R_s(t) \gg r$, because the primary field (23)

is expelled from the singularity $r \to 0$. Therefore, the boundary between the dipole $(r > a)$ and quasi-uniform fields inside the star $(r < a)$ should be taken into account in solution (24).

Let the shock front reach the $r = a$ surface at $t = t_a$. Starting from this time, the boundary between the fields is entrained in the plasma motion, and its radius increases as

$$R_a(t) = a + \int\limits_{t_a}^{t} u(R_a(\tau), \tau) d\tau, \quad t \geq t_a;$$

whence we obtain using (9)

$$R_a(t) = a \left[\frac{R_s(t)}{a} \right]^{\mu} \geq a, \quad t \geq t_a. \quad (25)$$

Since the shock front moves faster than the downstream matter, $R_s(t) > R_a(t)$ at $t > t_a$. In the region $R_a \leq r \leq R_s$, solution (24) is applicable for a magnetic dipole. At $r < R_a(t)$, solution (21) is applicable if the primary field at $r < a$ may be considered uniform. After the introduction of the above constraint, the field decreases with time everywhere in the cavity. It reaches the largest value on the $r = R_a(t)$ surface, on which it also decreases with time:

$$B_r(R_a(t), t, \vartheta) = \frac{2M \cos\vartheta}{R_a^3(t)} \left(\frac{R_s(t)}{R_a(t)} \right)^{\sigma-1} \quad (26)$$

$$= \frac{2M \cos\vartheta}{a^3} \left(\frac{a}{R_s(t)} \right)^{2\mu},$$

$$B_\vartheta(R_a(t), t, \vartheta) = \sigma \frac{M \cos\vartheta}{R_a^3(t)} \left(\frac{R_s(t)}{R_a(t)} \right)^{\sigma-1} \quad (27)$$

$$= \sigma \frac{M \cos\vartheta}{a^3} \left(\frac{a}{R_s(t)} \right)^{2\mu}.$$

For the solution obtained, constraint (22) remains valid. Once the shock front has reached a given distance r, both field components increase with time to the point specified by the condition $r = R_a(t)$ and reach (26) and (27) and then decrease.

(3) **Inhomogeneous medium.** An explosion into the cavity produced by the stellar wind from the pre-supernova. In this case, $\rho_0 \propto r^{-2}$ and, according to Sedov (1972), $R_s(t) \propto t^{2/3}$ if the stellar wind velocity is ignored. A simple model of the magnetic field in the solar wind was first considered by Parker (1963). The generalization of his solution that resembles the field of a distorted dipole is

$$B_r(r, t, \vartheta, \alpha) \quad (28)$$

$$= F\left(a, \alpha - \frac{(r-a)\Omega}{u_w} + \Omega t \right) \left(\frac{a}{r} \right)^2 2 \cos\vartheta,$$

$$B_\vartheta(r, t, \vartheta, \alpha)$$

$$= p \frac{\partial}{\partial \alpha} F\left(a, \alpha - \frac{(r-a)\Omega}{u_w} + \Omega t \right) \left(\frac{a^2 \Omega}{u_w r} \right) \sin\vartheta,$$

$$B_\alpha(r, t, \vartheta, \alpha)$$

$$= q F\left(a, \alpha - \frac{(r-a)\Omega}{u_w} + \Omega t \right) \frac{a^2 \Omega}{u_w r} 2 \cos\vartheta \sin\vartheta.$$

Here, Ω is the angular velocity of the star, u_w is the constant velocity of the solar wind, a is a radius up to which the partial corotation of magnetic field lines with the star is preserved, and the constants p and q must satisfy the condition $p + q = 1$. The function $F(a, \alpha)$ defines the field strength on the $r = a$ sphere. The field downstream of the front of a blast wave can be calculated only if there is no dependence on the angle α:

$$B_r = \left(\frac{a}{r} \right)^2 B_r^0(a, \vartheta), \quad (29)$$

$$B_\alpha = \sigma \left(\frac{r}{R_s(t)} \right)^{\sigma-1} \left(\frac{a^2 \Omega}{u_w r} \right) B_r^0(a, \vartheta) \sin\vartheta,$$

$$B_\vartheta = 0, \quad a \leq r \leq R_s(t),$$

where $B_r^0(a, \vartheta) = 2F(a) \cos\vartheta$. The radial field component is not perturbed, while the azimuthal component after the jump at the front is attenuated with the factor $(r/R_s(t))^{\sigma-1}$.

It follows from the above analysis that allowing for the field compression downstream of the front of a blast wave leads to an enhancement of the tangential field component compared to the radial component in a layer with a thickness of $0.1-0.2$ of the SNR radius, i.e., in the region with the largest number of accelerated particles.

SUPPRESSION OF THE TANGENTIAL FIELD COMPONENT NEAR THE FRONT BY ACCELERATED PARTICLES

The previous analysis took into account the possibility of particle acceleration at the shock front only in the sense that the compression ratio σ could be larger than the standard value for a nonrelativistic plasma, $\sigma = (\gamma + 1)/(\gamma - 1) = 4$, if the particles are accelerated to relativistic energies. Meanwhile, the electric current produced by accelerated particles can generate a magnetic field that must be added to the explosion-distorted primary field calculated in the preceding section.

In the model of a plane stationary front, this problem has been solved by Dolginov *et al.* (2004). They considered the possibility of the generation of a static magnetic field with a scale length on the order of the prefront thickness, $L \approx \kappa_1/u_1$, by the electric current

of accelerated relativistic particles. Here, κ_1 is the relativistic particle diffusion tensor component normal to the front, and u_1 is the normal component of the hydrodynamic plasma velocity. For nonrelativistic shocks, this scale length is much larger than the Larmor radius of relativistic particles.

Let a plane shock front ($z = 0$) be the source of accelerated relativistic protons. Since atomic nuclei heavier than protons and electrons account for a small fraction of the accelerated particles, we disregard them. The background plasma and the background neutral medium are also assumed to be purely hydrogen ones. The plasma moves along the Oz axis, and its normal velocity component undergoes a jump $\Delta u = u_z(0) - u_2 > 0$ at the front and is constant downstream of the front. The velocity $u_z(z)$ upstream of the front ($z < 0$) can smoothly decrease from u_1 far from the front to $u_z(0) < u_1$ if an appreciable part of the shock energy is spent on the particle acceleration and the magnetic-field generation.

Since the particles are accelerated near the front, the source of energetic particles was specified at the front in the form

$$Q(z) = q_0\delta(z), \qquad (30)$$

which corresponds to uniform particle injection from the background plasma into acceleration by the shock front. The injection rate q_0 can be expressed in terms of the dimensionless parameter $\chi < 1$—the fraction of the particle flux injected into acceleration: $q_0 = n_0 u_1 \chi$, where n_0 is the total density of the ions and neutral atoms upstream of the front. The neutral atoms are ionized at the front. The accelerated protons are drawn from the thermal background; therefore, we should specify the sink Q_{th} of thermal protons at the front,

$$Q_{\text{th}}(z) = -Q(z), \qquad (31)$$

which ensures that the electric charge and the number of particles are conserved.

We assumed that there were an initial large-scale magnetic field $\mathbf{B}_1$ upstream of the front, whose direction was specified by the polar angles θ and α, and turbulent pulsations containing random particle-scattering small-scale magnetic fields. In a turbulent medium, the relativistic and thermal particles will walk randomly. It is important that the magnetic-field direction would not coincide with the direction of the normal to the front, because in this case, the current can flow along along the Oz axis when the particles are uniformly injected into acceleration at the front and, by symmetry, will not produce any magnetic field. The diffusion coefficients κ of the relativistic protons and the analogous coefficients D^p and D^e of the background nonrelativistic protons and electrons

are different along and across the large-scale magnetic field. In addition, they are different upstream and downstream of the front.

Calculations of the current upstream of the front that is produced by accelerated protons as well as by thermal protons and electrons yield the following results:

$$j_x = eu_z(z)\left\{\frac{D_{xz}^e + D_{xz}^p}{D_1^e + D_1^p} - \frac{\kappa_{xz}}{\kappa_1}\right\} N(z), \qquad (32)$$

$$j_y = eu_z(z)\left\{\frac{D_{yz}^e + D_{yz}^p}{D_1^e + D_1^p} - \frac{\kappa_{yz}}{\kappa_1}\right\} N(z),$$

$$j_z = 0,$$

if the diffusion coefficients of the thermal particles are negligible, $D_1^{p,e} \ll \kappa_1$. If the latter condition is not satisfied but the thermal particle diffusion is ambipolar, as is the case in neutral clouds and in the warm phase (Ruzmaĭkin *et al.* 1988), then the protons and electrons diffuse together with equal diffusion coefficients $D_{\mu\nu}^e \approx D_{\mu\nu}^p$, which are close to the smallest of them in order of magnitude. In this case,

$$j_x = eu_z(z)\left\{\frac{D_{xz}^p}{D_1^p} - \frac{\kappa_{xz}}{\kappa_1}\right\} N(z), \qquad (33)$$

$$j_y = eu_z(z)\left\{\frac{D_{yz}^p}{D_1^p} - \frac{\kappa_{yz}}{\kappa_1}\right\} N(z),$$

$$j_z = 0.$$

For ambipolar diffusion, expressions (32) and (33) are identical. The function $N(z)$ in them describes the distribution of relativistic protons upstream of the front:

$$N(z) = N_0 e^{-\zeta(z)}, \quad N_0 = \frac{q_0}{u_2}, \qquad (34)$$

$$\zeta(z) = \int_z^0 \frac{u_z(z')dz'}{\kappa_1(z')}, \quad z \le 0.$$

The magnetic field can be calculated from the equations

$$\frac{\partial \mathbf{B}}{\partial t} = -\nabla \times (\nu\nabla \times \mathbf{B} \qquad (35)$$

$$+ \nabla \times [\mathbf{u} \times \mathbf{B}] + \frac{4\pi}{c}\nabla \times \nu_m\mathbf{j},$$

$$\nabla \cdot \mathbf{B} = 0.$$

Here, ν_m is the collisional magnetic viscosity averaged over an ensemble of turbulent pulsations, $\nu_{\text{turb}} = \langle u'^2\rangle\tau_c/3$ is the turbulent magnetic viscosity, $\nu = \nu_{\text{turb}} + \nu_m$ is the total viscosity, $\mathbf{u}$ is the bulk velocity of the medium, $\mathbf{u}'$ is the turbulent velocity, and τ_c is the turbulence correlation time. In a galactic disk, the turbulent viscosity is generally several orders of

magnitude larger than the collisional viscosity due to the large correlation scale (about 100 pc). However, the situation changes near a separate shock front. Strong Alfvén turbulence with $\delta B \approx B$ is assumed to grow near the front; we estimate the turbulent magnetic viscosity as $\nu_{\text{turb}} \approx u_A r_g$, where u_A is the Alfvén velocity, and r_g is the gyroradius of a relativistic proton ($\mathcal{E} \approx 1$ GeV). Using the parameters for the most important phases of the interstellar medium (the warm phase and cold neutral clouds) in this problem, we verify that ν_{turb} is two orders of magnitude smaller than ν_m. Therefore, we assume below that $\nu \approx \nu_m$.

The quantities ν_m and $\mathbf{u}$ in an inhomogeneous system, which is what the upstream plasma is, depend on the z coordinate. The curl of the current $\mathbf{j}$ produced by accelerated particles, which is the source of an additional magnetic field, appears on the right-hand side of the first equation.

The self-consistent solution of Eqs. (35) that includes the dependence of the particle diffusion coefficients $\kappa_{\alpha\beta}$ and $D^{p,e}_{\alpha\beta}$ and the magnetic viscosity ν_m on the total field $\mathbf{B}$ (Dolginov $et~al.$ 2004) yields the following results. If the inequality $\nu_m \gg \kappa_1$ holds, then the resulting field at the front ($z = 0$) is given by

$$B_x(0) = -\frac{B_{1y}B_{1z}}{|B_{1z}|}\frac{\delta}{\xi(1+\delta^2)}, \quad B_y(0) = \frac{B_{1y}}{\xi(1+\delta^2)}. \quad (36)$$

Here,

$$\xi = b^2/B_{1z}^2, \quad b^2 = 2\pi n_0 m_p u_1^2 \eta + \frac{B_1^2}{4}, \quad (37)$$

$$\delta = \frac{d-1}{d+1}, \quad d = \frac{D_\perp^p}{D_\parallel^p - D_\perp^p} \geq 0.$$

The primary field far from the front has the $B_{1x} = 0$, B_{1y}, and B_{1z} components. The quantity b has the dimensions of magnetic induction and represents, in order of magnitude, the field that can emerge if the fraction

$$\eta = \frac{P_c(0) + B^2(0)/8\pi - B_1^2/8\pi}{n_0 m_p u_1^2} \quad (38)$$

of the energy density $n_0 m_p u_1^2/2$ of the gasdynamic flow is transformed into magnetic energy. The quantity $P_c(0)$ is the pressure of the accelerated particles at the front.

For a moderate ($\eta = 0.1$) acceleration rate and typical conditions in the warm phase and in neutral clouds, $\xi \approx 10^4 \gg 1$ and $0 \leq \delta^2 \leq 1$. Therefore, the parallel components of the primary field at the front turn out to be suppressed by the secondary field generated by the electric current of accelerated particles. The suppression factor ($\sim 10^4$ for the conditions under

consideration) is large. Even if the fraction of the energy transferred to the accelerated particles decreases to $\eta = 10^{-4}$, the tenfold suppression of the field components along the front is preserved.

If the condition $\nu_m \gg \kappa_1$ opposite to that considered above is satisfied, then, instead of (36), the field at the front takes the form

$$B_x(0) = B_{1y}\frac{2B_1^2 B_{1z}\delta}{B_{1z}^2 H(1-\eta)(1+\delta^2)}, \quad (39)$$

$$B_y(0) = -B_{1y}\frac{2B_1^2}{|B_{1z}|H(1-\eta)(1+\delta^2)}.$$

Here,

$$H = \frac{e\nu_0(8\pi n_0 m_p u_1^2 \eta + B_1^2)}{2(\gamma_c - 1)c\overline{T}}, \quad (40)$$

ν_0 is the collisional magnetic viscosity at typical magnetic field strengths in the corresponding phase ($\nu_0 \approx 5 \times 10^{21}$ cm^2 s^{-1} in neutral clouds and $\nu_0 \approx 5 \times 10^{21}$ cm^2 s^{-1} in the warm phase; see Ruzmaĭkin $et~al.$ 1988), $\overline{T}$ is the mean kinetic energy of the accelerated particles, and $\gamma_c \approx 4/3$ for relativistic particles. The parameter $H/B_1 \approx 10^2 - 10^5 \gg 1$ at typical parameters in the warm phase and in neutral clouds. Thus, in this case, as in the previous one, only the magnetic field component normal to the front remains near the front. The state in which only the field component normal to the front exists for uniform particle injection is stable against the subsequent field generation: the generation is not possible, since the system is symmetric.

Results (36) and (39) apply to the case where there is a field component normal to the front, $B_{1z} \neq 0$. In this case, the tangential component is suppressed almost completely. At $B_{1z} = 0$, we cannot rule out states with a nonzero tangential component, but they are probably unstable (for more detail, see Dolginov $et~al.$ 2004).

Applying the result obtained to a spherical SNR, we may assert that only the radial large-scale field remains near the front when the particles are appreciably accelerated at the front, while the tangential components are suppressed on most of the front surface (with the possible exception of the equatorial region in which there is no or very weak radial field). The upstream field rearranged by accelerated particles is drifted by the plasma flow downstream of the front. For the conditions under consideration, there must be no large-scale tangential field components in the cavity either. Actually, however, various disregarded small-scale inhomogeneities can be present in the matter through which the shock front propagates, and instabilities that are capable of generating transverse (relative to the dominant velocity) stochastic field

components are possible near the front. One of the possible mechanisms of this generation is considered in the next section.

THE GENERATION OF TANGENTIAL FIELD COMPONENTS FOR NONUNIFORM INJECTION

If the particle injection into acceleration by the shock front is nonuniform along the front, then the distribution function of the accelerated particles will depend on the transverse (relative to the normal to the front) coordinates, and a diffusive current of accelerated particles directed along the front will appear. This current is capable of generating tangential (relative to the front) magnetic-field components.

Density nonuniformity of the upstream matter may serve as a natural cause of nonuniform injection, because a fraction $\chi < 1$ of the mass flow onto the front is injected into acceleration. The simplest and most commonly seen situation is probably the presence of small random density nonuniformities in the upstream matter. In this case, the injection is not only nonuniform, but also unsteady. To estimate the magnitude of the possible effect, let us consider the simplest steady-state case and use a source of the particles accelerated at the front that, in contrast to (30), depends on two coordinates:

$$Q(x, z) = q_0(1 + \epsilon \sin kx)\delta(z), \qquad \epsilon \ll 1. \quad (41)$$

As in the previous section, a compensating sink of thermal protons at the front is required: $Q_{\text{th}}(x, z) = -Q(x, z)$. The parameters k and ϵ specify the scale length of the density nonuniformity and its relative value. In our approach, the density nonuniformity scale length $L = 2\pi/k$ cannot be chosen to be too small. The particle acceleration time scale is of the order of $\tau_a \approx \kappa_1/u_1^2$, and a particle can diffuse in this time to a distance of the order of the prefront thickness $l \approx \sqrt{\kappa_1\tau_a} \approx \kappa_1/u_1$. For nonuniform injection to be preserved in the spatial distribution of the accelerated particles, the condition $L \gg l$ must be satisfied, i.e.,

$$k \ll u_1/\kappa_1. \quad (42)$$

The initial magnetic field is assumed to be normal to the front (the Oz axis). The problem will be solved in a non-self-consistent way, i.e., by assuming that the generated field is weak compared to the initial field.

The proton and electron currents satisfy the equations

$$\nabla \cdot \mathbf{j}_{\text{rel}}^p = eQ(x, z), \quad \nabla \cdot \mathbf{j}_{\text{th}}^p = -eQ(x, z), \quad (43)$$
$$\nabla \cdot \mathbf{j}^e = 0;$$

the currents themselves are expressed in terms of the particle distribution functions N, n^p, and n^e by the diffusion formulas:

$$(\mathbf{j}_{\text{rel}}^p)_\alpha = -e\kappa_{\alpha\beta}\frac{\partial N}{\partial x_\beta} + eu_\alpha N, \quad (44)$$

$$(\mathbf{j}_{\text{th}}^p)_\alpha = -eD_{\alpha\beta}^p\frac{\partial n^p}{\partial x_\beta} + eu_\alpha n^p + \sigma^p E_\alpha, \quad (45)$$

$$(\mathbf{j}^e)_\alpha = +eD_{\alpha\beta}^e\frac{\partial n^e}{\partial x_\beta} - eu_\alpha n^e + \sigma^e E_\alpha, \quad (46)$$

where the self-consistent electric field was included in the current of background particles, and $\sigma^{p,e}$ are the electric conductivities. The electric field has no appreciable effect on the motion of the relativistic particles because of their high energy. The electric field can be expressed in terms of the electrostatic potential:

$$\mathbf{E} = -\nabla\varphi, \qquad \triangle\varphi = -4\pi(N + n^p - n^e). \quad (47)$$

The subsequent calculations were performed following the scheme used previously by Dolginov and Toptygin (2003) and Dolginov *et al.* (2004). The distribution function of the accelerated particles can be determined from the first equation in (43), the condition for the solution being bounded, and the boundary conditions at the front, which in our case take the form

$$N|_{z=-0} = N_{z=+0}, \quad \kappa_\parallel\frac{\partial N}{\partial z}\bigg|_{z=-0} - \kappa_\parallel\frac{\partial N}{\partial z}\bigg|_{z=+0} \quad (48)$$
$$- (u_1 - u_2)N = q_0(1 + \epsilon \sin kx).$$

Upstream of the front ($z < 0$),

$$N(x, z) = \frac{q_0}{u_2}(1 + \epsilon \sin kx)e^{u_1 z/\kappa_{\parallel,1}}, \quad (49)$$

where condition (42) is used.

The distribution functions of the nonequilibrium background particles can be determined from the remaining equations (43)–(47) and have a structure similar to (49), which is not given here to save space. Their dependence on coordinates is the same as that for relativistic particles, because the plasma perturbation adjusts to the energetic accelerated component.

According to (35), the magnetic field in the steady-state case and in a homogeneous medium ($\nu = \text{const}$, $\nu_m = \text{const}$) can be calculated from the equation

$$\triangle\mathbf{B} + \frac{1}{\nu_m}\nabla \times [\mathbf{u} \times \mathbf{B}] = -\frac{4\pi}{c}\nabla \times \mathbf{j}. \quad (50)$$

The curl of the total current $\mathbf{j} = \mathbf{j}_{\text{rel}}^p + \mathbf{j}_{\text{th}}^p + \mathbf{j}^e$ on the right-hand side of the equation can be calculated

Table 1

Phase	Observed field B_{obs}, G	Calculated field B_y^0, G	Product of small parameters $\epsilon\chi(kl)$
Cold $n_0 = 20$ protons cm^{-3} $\nu_m = 5 \times 10^{21}$ cm^2 s^{-1}	1.5×10^{-5}	$8 \times 10^4 \epsilon\chi(kl)$	2×10^{-8}
Warm $n_0 = 0.2$ protons cm^{-3} $\nu_m = 3 \times 10^{20}$ cm^2 s^{-1}	3×10^{-6}	$50\epsilon\chi(kl)$	6×10^{-8}

using formulas (43)–(45) and can be expressed upstream of the front as

$$[\nabla \times \mathbf{j}]_x = -ek\epsilon q_0 \frac{u_1 \kappa_H}{u_2 \kappa_\parallel} e^{u_1 z/\kappa_\parallel} \cos kx, \qquad (51)$$

$$[\nabla \times \mathbf{j}]_y = ek\epsilon q_0 \frac{u_1}{u_2} \qquad (52)$$
$$\times \left\{ 1 - \frac{\kappa_\perp}{\kappa_\parallel} + \frac{D_\parallel^p - D_\perp^p + D_\parallel^e - D_\perp^e}{D_\parallel^p + D_\parallel^e} \right\}$$
$$\times e^{u_1 z/\kappa_\parallel} \cos kx,$$

$$[\nabla \times \mathbf{j}]_z = ek^2 \epsilon q_0 \frac{\kappa_H}{u_2} e^{u_1 z/\kappa_\parallel} \sin kx. \qquad (53)$$

Here, in addition to (42), we use the inequalities $\kappa_\parallel \gg D^{p,e}$ and discard the terms of the order of $D^{p,e}/\kappa_\parallel$. All of the diffusion coefficients pertain to the upstream region. It follows from the structure of the derived expressions that the curl of the current becomes zero in an isotropic medium (in which $\kappa_\perp = \kappa_\parallel$ and $\kappa_H = 0$ and similar relations hold for the background particles). However, there is a large-scale magnetic field in SNRs, and the curl of the current is nonzero.

We find the magnetic-field components from Eq. (50):

$$B_\alpha(x, z) = -\frac{4\pi\nu_m \kappa_\parallel^2}{cu_1^2(\nu_m - \kappa_\parallel)} [\nabla \times \mathbf{j}]_\alpha. \qquad (54)$$

The constant factors (amplitudes) are

$$B_x^0 = \frac{4\pi e n_0 \nu_m \kappa_H \kappa_\parallel}{cu_2(\nu_m - \kappa_\parallel)} k\epsilon\chi, \qquad (55)$$

$$B_z^0 = -\frac{4\pi e n_0 \nu_m \kappa_H \kappa_\parallel^2}{cu_1 u_2(\nu_m - \kappa_\parallel)} k^2 \epsilon\chi,$$

$$B_y^0 = -\frac{4\pi e n_0 \nu_m \kappa_\parallel^2}{cu_2(\nu_m - \kappa_\parallel)} \qquad (56)$$
$$\times \left\{ 1 - \frac{\kappa_\perp}{\kappa_\parallel} + \frac{D_\parallel^p - D_\perp^p + D_\parallel^e - D_\perp^e}{D_\parallel^p + D_\parallel^e} \right\} k\epsilon\chi.$$

Clearly, the relation $\nu_m = \kappa_\parallel$ for which solutions (55) and (56) are inapplicable is highly unlikely. Excluding this possibility from our analysis, let us estimate the most representative B_y^0—the magnetic field component for the two limiting cases: $\kappa_\parallel \gg \nu_m$ and $\kappa_\parallel \ll \nu_m$. The boundary between them is established, in order of magnitude, by the relations $\nu_m \approx \kappa_\parallel$ and $|\nu_m - \kappa_\parallel| \approx \nu_m$; when these relations hold, the magnetic field is strongest:

$$B_y^0 \approx \frac{4\pi e n_0 \nu_m \sigma}{c} \epsilon\chi(kl). \qquad (57)$$

The expression in the braces of formula (56) is probably close to unity. The results of our field calculations for this case are presented in Table 1. This table also lists the parameters of the interstellar medium taken from the monograph by Ruzmaĭkin *et al.* (1988). The last column of Table 1 gives the product of the small parameters whose value ensures an observable field strength. These parameters can vary over a significant range while remaining very small. For example, if the relative density nonuniformity is $\epsilon \approx 10^{-2}$ and if the nonuniformity scale length λ is two orders of magnitude larger than the prefront thickness ($kl = 2\pi l/\lambda \approx 0.1$), then it will suffice to inject into acceleration a fraction $\chi \approx 10^{-4}$ of the background particles to generate an observable field. In fact, the field estimate probably remains valid even at $\lambda \approx l$, which allows ϵ and χ to be decreased further.

The result obtained shows that small density nonuniformities in the ambient medium upstream of the front produce random magnetic-field nonuniformities. The field components parallel to the shock front will probably reach their largest values, because the radial component $B_z^0 = B_r^0$ contains the factor $kl < 1$. The mechanism considered above is also sufficient for the generation of much stronger fields than those given in Table 1 (e.g., Jones *et al.* (2003) assumed a field of ~ 500 μG in SNR Cas A).

POLARIZATION OF RADIO EMISSION

In conclusion, let us attempt to solve the inverse problem: to determine the possible relations between

Table 2

$\sin^2 \beta$	1.0	0.8	0.67	0.6	0.5	0.33	0.2	0.1
s_1^2	1.27	1.35	1.41	1.45	1.54	2.23	2.45	4.13
s_2^2	0.81	0.75	0.71	0.68	0.62	0.56	0.081	

the regular and stochastic magnetic-field components from the observed polarization of the synchrotron radiation for SNR 1006 studied by Reynolds and Gilmore (1993). We use the paper by Korchak and Syrovatskiĭ (1961), who calculated the polarization of the synchrotron radiation from electrons with a power-law energy spectrum for two magnetic-field models. If the field in the system may be considered as the superposition of a uniform component $\mathbf{B}_0$ and a statistically isotropic random field $\mathbf{B}_1$, then the degree of polarization for $s^2 = B_0^2/B_1^2 \ll 1$ is given by

$$\Pi = \frac{(\gamma + 1)(\gamma + 3)(\gamma + 5)}{32(\gamma + 7/3)} \tag{58}$$
$$\times \left[1 - \frac{\gamma^2 + 8\gamma + 3}{24} s^2 \sin^2 \beta\right] s^2 \sin^2 \beta.$$

Here, γ is the index of the electron energy spectrum, and β is the angle between $\mathbf{B}_0$ and the line of sight.

The particle spectral index, $\gamma = 2.2$, and the degree of polarization, $\Pi \approx 11\%$, are known from observations of the synchrotron radiation. Expression (58) yields $s^2 \sin^2 \beta \approx 0.15$. The value of $s^2 \approx 0.25$ given by Reynolds and Gilmore (1993) is obtained at a fixed observing angle $\sin^2 \beta \approx 0.6$. In fact, the angle β is probably different in different SNR regions, as is the degree of polarization. Therefore, the above numerical values should be considered as only rough estimates.

The second case of a nonisotropic constant field considered by Korchak and Syrovatskii is more suitable for our system, in which, according to the results of the previous section, there is an anisotropic random field directed predominantly perpendicular to the radial regular field. In this case, the degree of polarization calculated by these authors is described by the formula

$$\Pi = \frac{15(\gamma + 1)(\gamma + 5)|\varrho| \sin^2 \beta}{2(\gamma + 7/3)[4(\gamma + 7) + 5(\gamma + 1)\varrho(1 - 3\cos^2 \beta)]}, \tag{59}$$

where

$$\varrho = \frac{\langle B_\|^2 \rangle - \langle B_\perp^2 \rangle}{\langle B_\|^2 \rangle + \langle B_\perp^2 \rangle}, \qquad |\varrho| \le 1 \tag{60}$$

is the parameter that characterizes the degree of field anisotropy between the radial and tangential (to the

front) directions and simultaneously the relation between the energies of the regular and random components, because the radial component is mainly regular in our case. It follows from (59) that the observed degree of polarization ($\sim 11\%$) can be reached at different signs of ϱ and, hence, for different relations between the regular and random field components. In addition, the angle β between the axis of symmetry of the field and the line of sight still remains uncertain. Table 2 gives two values of the ratio $s^2 = \langle B_\|^2 \rangle / \langle B_\perp^2 \rangle$ obtained from (59) at $\Pi \approx 11\%$ and $\gamma = 2.2$ for each angle.

The above results for the second field model differ greatly from those for the first field model. The observed polarization can be explained in terms of the second (anisotropic) field model both by assuming that $B_\| < B_\perp$ and in the opposite case $B_\| > B_\perp$. Therefore, the conclusion reached by Reynolds and Gilmore (1993) that the stochastic component accounts for about 80% of the entire field energy cannot be considered reliable. The results obtained here show that a quantitative relation between the energies of the regular and random magnetic field components can be derived only after refining the field structure and obtaining more accurate values with a better resolution for the polarization of the radiation.

CONCLUSIONS

We have obtained a self-similar solution for the magnetic field in a supernova remnant at the Sedov phase. The particle acceleration at shock fronts is shown to have a significant effect on the structure of the regular and stochastic magnetic fields in SNRs. Allowing for the secondary magnetic field that is generated by the electric current of accelerated particles makes it possible to qualitatively explain the observational data on the polarization of synchrotron radio emission. However, reliable quantitative relations between the energies of the regular and stochastic fields can be derived only after improving the SNR field model and obtaining more accurate observational polarization data.

ACKNOWLEDGMENTS

REFERENCES

1. W. I. Axford, E. Leer, and G. Scandron, in *Proceedings of X Leningrad Seminar on Cosmophysics* (Izd. Fiz. Tekh. Inst. Ioffe, Leningrad, 1978), p. 125.
2. V. B. Berestetskiĭ, E. M. Lifshits, and L. P. Pitaevskiĭ, *Quantum Electrodynamics*, 2nd ed. (Nauka, Moscow, 1989; Pergamon Press, Oxford, 1982).
3. J. R. Dickel, J. A. Eilek, E. M. Jones, and S. P. Reynolds, Astrophys. J., Suppl. Ser. **70**, 497 (1989).
4. J. R. Dickel, W. J. M. van Breugel, and R. G. Strom, Astron. J. **101**, 2151 (1991).
5. A. Z. Dolginov and I. N. Toptygin, Pis'ma Astron. Zh. **29**, 426 (2003) [Astron. Lett. **29**, 374 (2003)].
6. A. Z. Dolginov, N. I. Podol'skaya, and I. N. Toptygin, Pis'ma Astron. Zh. **30**, 196 (2004) [Astron. Lett. **30**, 169 (2004)].
7. R. M. Duin and R. G. Strom, Astron. Astrophys. **39**, 33 (1975).
8. V. L. Ginzburg and S. I. Syrovatskiĭ, *The Origin of Cosmic Rays* (Izd. Akad. Nauk SSSR, Moscow, 1963).
9. S. F. Gull, Mon. Not. R. Astron. Soc. **161**, 47 (1973).
10. T. J. Jones, L. Rudnick, T. DeLaney, and J. Bowden, Astrophys. J. **587**, 227 (2003).
11. B.-I. Jun and T. W. Jones, Astrophys. J. **511**, 774 (1999).
12. A. A. Korchak and S. I. Syrovatskiĭ, Astron. Zh. **38**, 885 (1961) [Sov. Astron. **5**, 679 (1961)].
13. G. F. Krymskiĭ, Izv. Akad. Nauk SSSR, Ser. Fiz. **45**, 461 (1981).
14. T. A. Lozinskaya, *Supernovae and Star Wind. Interacion with Glactic Gas* (Nauka, Moscow, 1986) [in Russian].
15. Y. Matsui, K. C. Long, J. R. Dickel, and E. W. Greisen, Astrophys. J. **287**, 295 (1984).
16. E. N. Parker, *Interplanetary Dynamical Processes* (New York, 1963; Mir, Moscow, 1965).
17. S. P. Reynolds and D. M. Gilmore, Astron. J. **106**, 272 (1993).
18. A. A. Ruzmaĭkin, D. D. Sokolov, and A. M. Shukurov, *Galactic Magnetic Fields* (Nauka, Moscow, 1988) [in Russian].
19. L. I. Sedov, *Similarity and Dimension Methods in Mechanics* (Nauka, Moscow, 1972) [in Russian].
20. I. N. Toptygin, Pis'ma Astron. Zh. **26**, 421 (2000) [Astron. Lett. **26**, 356 (2000)].
21. H. J. Völk and J. M. McKenzie, Astron. Astrophys. **116**, 191 (1982).

Translated by V. Astakhov

The Role of Epithermal Neutrons in AGB Stars: Boron Synthesis

A. I. Shapiro*

Sobolev Astronomical Institute, St. Petersburg State University, St. Petersburg, Russia
Received August 6, 2003

Abstract—We consider the influence of the capture of epithermal neutrons on the nucleosynthesis in asymptotic giant branch stars (the Petrov–Shlyakhter effect). We show that epithermal neutrons can be captured by nitrogen through the hitherto unanalyzed channel $^{14}\text{N}(n, \alpha)^{11}\text{B}$. Since the proton concentration in the partial mixing zone is low, this process results in an appreciable boron concentration. This boron can be brought to the stellar surface by peculiar processes. We analyze the boron concentration as a function of the assumed parameters for the partial mixing zone. © *2004 MAIK "Nauka/Interperiodica".*

Key words: *stars, physical processes, nucleosynthesis.*

INTRODUCTION

The main natural furnaces where neutron capture reactions take place are asymptotic giant branch (AGB) stars. The structure of these stars and the pattern of nucleosynthesis in them were described in detail by Straniero *et al.* (1995), Blocker (1999), Olofsson (1999), Mowlavi (1999), and Goriely and Mowlavi (2000).

The main source of neutrons in moderately massive ($M \leq 6M_\odot$) stars is the reaction $^{13}\text{C}(\alpha, n)^{16}\text{O}$. The neutrons produced in this reaction have an initial energy (~ 2 MeV) much higher than the thermal energy in the partial mixing zone (~ 10 keV). Thus, before being thermalized, the neutrons undergo several scatterings by heavy nuclei, gradually losing their energy. Therefore, apart from thermal neutrons (with a Maxwellian energy distribution), more energetic slowing-down neutrons will be present in the spectrum. They will form a peculiar peak in its epithermal region (see Fig. 1). The fraction of such neutrons is very low (see the end of Section 3). However, the capture cross sections for some of the reactions increase greatly with neutron energy. Therefore, despite the small number of epithermal neutrons, the rates of these reactions can increase significantly. This idea was first formulated by Petrov and Shlyakhter (1986, 1988). Below, the increase in the reaction rates due to the presence of epithermal neutrons is called the Petrov–Shlyakhter effect.

An outgrowth of this approach is the idea of considering the usually disregarded reactions that can proceed *only* on epithermal neutrons. The cross sections for these reactions must be equal to zero in the thermal region and must be significant in the epithermal region. One of these reactions is the boron synthesis reaction $^{14}\text{N}(n, \alpha)^{11}\text{B}$. In the region of the epithermal peak, its cross section is fairly large (~ 300 mb). Therefore, one might expect this reaction to be able to produce an appreciable amount of boron and to be a new boron synthesis mechanism in the Universe. In this paper, we investigate the suggested mechanism of boron synthesis on epithermal neutrons.

The paper is structured as follows. Section 1 gives general information about the structure of AGB stars and the formation of the partial mixing zone required for nucleosynthesis. Section 2 describes the con-
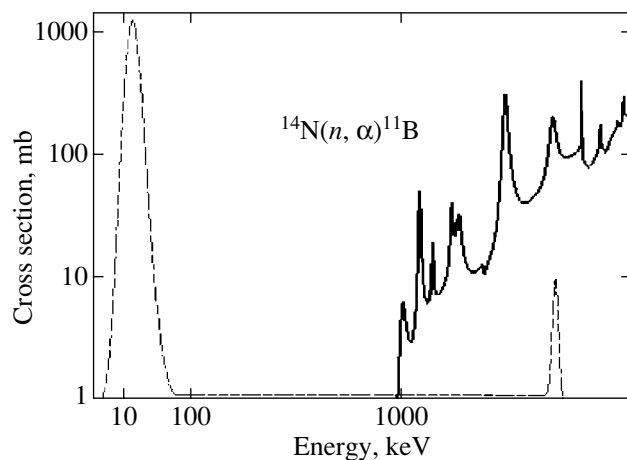
Fig. 1. Cross section $\sigma_a(E)$ for the reaction $^{14}\text{N}(n, \alpha)^{11}\text{B}$ (solid curve) in comparison with $\Phi(E)E$ (dashed curve; not to scale).

*E-mail: AlexSh82@mail.ru

struction of an improved neutron spectrum (including epithermal neutrons). Section 3 is devoted directly to boron synthesis. It constitutes the main part of this paper. Subsequently, we describe the influence of temperature variations on boron synthesis. In conclusion, we estimate the total amount of synthesized boron and its removal from the partial mixing zone.

1. THE PARTIAL MIXING ZONE IN AGB STARS

A carbon−oxygen core is located at the center of an AGB star. This core is surrounded by very light (a few thousandths of the solar mass) shell energy sources, helium and hydrogen. They are separated by a moderately massive intermediate helium shell. An extended hydrogen envelope lies above the sources.

For the neutron production reaction $^{13}C(\alpha, n)^{16}O$ to proceed, carbon and hydrogen must be mixed into the helium shells. The key point is that the burning of the helium source is unsteady. Helium does not burn most of the time, but flashes occur approximately once in 10^4 yr. During a flash, the helium source releases much energy and becomes convective together with the intermediate helium region. Concurrently, the helium shells are enriched with carbon.

Hydrogen enrichment is a slightly more complex process. Hydrogen is not mixed to the helium shells during a flash, because the boundary of the outer hydrogen convective envelope recedes from the core, running away from the inner convection zone between the nuclear sources. As a result, no mixing of the helium and hydrogen shells takes place.

After the completion of a helium flash, when convection in the inner shells has already been damped out but the hydrogen source has not yet ignited, the boundary of the outer convective hydrogen envelope begins to return to its original location, to the shells that were also involved in convective mixing (in inner convective shells). Thus, it approaches a region with a jump in chemical composition and, hence, with a jump in opacity; the boundary of the convection region is unstable. Convective overshooting beyond the Schwarzschild boundary takes place. As a result, the jump in chemical composition begins to move inward, and convection affects more and more new shells. A detailed qualitative description of this process was given by Mowlavi (1999). The so-called third (convective) dredge-up takes place. It lasts for about a hundred years. One of the consequences of this dredge-up is that carbon and nucleosynthesis products are brought to the surface.

The convective dredge-up alone is not enough for the production of neutrons. A mechanism capable of bringing protons deep into the shell sources is required. The presence of a shell weakly contaminated by protons is also of great importance, because much nitrogen that captures almost all of the neutrons, leaving nothing for the s-process, is produced at high proton concentrations. This mechanism was introduced by Iben and Renzini (1982) and named partial mixing. During the convective dredge-up, hydrogen penetrates deep into the region between the shell sources through partial mixing. It should be emphasized that the physical causes of partial mixing are not yet completely clear. There are several different hypotheses (see, e.g., Denissenkov and Tout 2003).

In this paper, as in most of the papers devoted to the s-process in AGB stars, an exponentially (inward) falling proton concentration profile is used to describe the degree of contamination. Goriely and Mowlavi (2000) qualitatively analyzed the errors to which an arbitrarily taken exponential profile can lead. It should be noted that the influence of the pattern of the proton contamination profile on the boron synthesis is much weaker than it is on the standard synthesis of elements in the s-process (for a discussion, see the first part of Section 5).

Partial mixing gives rise to a zone that simultaneously contains hydrogen, helium, and carbon—the so-called partial mixing zone. The first two reactions of the standard CNO cycle proceed in this zone: $^{12}C(p, \gamma)^{13}N(\beta^+\nu)^{13}C$. The ^{13}C being produced reacts with helium ($^{13}C(\alpha, n)^{16}O$), supplying neutrons for the nucleosynthesis in the partial mixing zone between successive convective dredge-ups. This reaction is the main source of neutrons for moderately massive ($M \leq 6M_\odot$) stars.

It should be noted that the temperature in the partial mixing zone in more massive stars is higher, and that the reaction $^{22}Ne(\alpha, n)^{25}Mg$ plays a major role in the neutron production. This reaction is also important in less massive stars during a secondary neutron flash, when the nucleosynthesis products of the partial mixing zone diffuse downward toward the hotter shells and interact with helium to produce ^{22}Ne, which immediately burns out on helium nuclei (Goriely and Mowlavi 2000). However, the influence of the secondary flash on the overall nucleosynthesis is generally believed to be weak. In addition, the energy of the neutrons being produced during neon burning (≈ 0.5 MeV) is much closer to the thermal energy than that during carbon burning (≈ 2 MeV), so the correction to the spectrum for "neon" neutrons must be much smaller. Therefore, we consider the Petrov−Shlyakhter effect only for the reaction $^{13}C(\alpha, n)^{16}O$.

2. THE NEUTRON SPECTRUM

The energy of the neutrons being produced in the reaction $^{13}\text{C}(\alpha,n)^{16}\text{O}$ is determined by the relative velocity of the ^{13}C and ^{4}He nuclei before their interaction, their center-of-mass velocity, and the scattering angle (Williams 1971; Petrov and Shlyakhter 1986, 1988).

The spectrum of the neutrons being produced can be fitted by the expression

$$f(E) = \frac{2}{\sqrt{\pi}\Delta} e^{-\left(\frac{E-E_0}{\Delta/2}\right)^2}, \qquad (1)$$

$$E_0 = \lambda\left(Q + 0.00122\left(Z_1^2 Z_2^2 A_r T_6^2\right)^{1/3}\right),$$

where Q is the energy released in the reaction; $\lambda = 1 - \frac{1}{A}$; $A_r = \frac{A_1 A_2}{A_1 + A_2}$; $A = A_1 + A_2$; and A_1, A_2 and Z_1, Z_2 are, respectively, the relative masses and charges of the ^{13}C and ^{4}He nuclei.

The dispersion is given by

$$\Delta = \sqrt{\Delta_1^2 + \Delta_2^2}, \quad \Delta_1 = \frac{4}{\sqrt{3}}(\epsilon_0 kT)^{\frac{1}{2}},$$

$$\Delta_2 = \frac{4\sqrt{kTE_0}}{\sqrt{A}\lambda},$$

where $\epsilon_0 = (bkT/2)^{2/3}$ is the most probable interaction energy of the ^{13}C and ^{4}He nuclei, and $b = 31.28 Z_1 Z_2 A^{1/2}$ keV$^{1/2}$.

Immediately after their production, the neutrons undergo elastic collisions, mainly with ^{4}He. Clearly, such collisions (scatterings) will slow down the neutrons, and their energy will gradually approach the thermal energy.

An asymptotic expression for the spectrum of the epithermal neutron flux $\phi_f(E)$ (Weinberg and Wigner 1959; Petrov and Shlyakhter 1988) can be derived from statistical considerations (the number of neutrons with a given energy E is constant):

$$\phi_f(E) = \frac{f(E)}{\Sigma_s(E)} + \frac{1}{\xi\Sigma_s(E)E}\int\limits_E^\infty f(E')dE', \quad (2)$$

where $\Sigma_s(E)$ is the scattering cross section, $\xi = 1 + \varepsilon\ln\varepsilon/(1-\varepsilon)$, $\varepsilon = ((A_s - 1)/(A_s + 1))^2$, and A_s is the atomic weight of the moderator. Here, the first term corresponds to the neutrons being produced with energy E, and the second term corresponds to the neutrons that gained this energy after several scatterings. The model of a spherically symmetric scattering is used to derive (2). The absorption of epithermal neutrons is disregarded.

During the scattering, the thermal velocities of the ^{4}He nuclei begin to have an effect near the thermal

energy. After the scattering, the neutron energy can both decrease and increase. As a result, scatterings lead to the establishment of a Maxwellian distribution,

$$\phi_{\text{th}}(E) = \phi_{\text{th}}\frac{E}{T^2}e^{-E/T}. \qquad (3)$$

An approximate form of the spectrum can be obtained as follows. We choose such a boundary energy E_G that $\phi_f(E_G) = \phi_{\text{th}}(E_G)$. Next, we assume that

$$\phi(E) = \begin{cases} \phi_f(E), & E \geq E_G \\ \phi_{\text{th}}(E), & E \leq E_G. \end{cases} \qquad (4)$$

Clearly, this representation describes roughly the transition between the thermal spectrum and the spectrum of the slowing-down neutrons. In addition, the slowing-down neutrons also slightly change the thermal spectrum. This change is equivalent to a slight increase in the temperature of the Maxwellian spectrum (Malaney 1988). However, in the subsequent calculations, the inaccuracy that results from the assumption of (4) may be ignored.

It now remains to relate expressions (2) and (3) for the flux via the normalization factor ϕ_{th}. In essence, this factor is responsible for the fraction of epithermal neutrons in the total spectrum. It can be determined from the condition that the number of neutrons being produced per unit time is equal to the number of absorbed neutrons. Since the spectrum of the neutrons being produced is normalized to unity, the following condition must be satisfied:

$$\phi_{\text{th}}\int\limits_0^{E_G} \frac{E}{T^2}e^{-E/T}\sigma_a(E)dE = 1, \qquad (5)$$

where $\sigma_a(E)$ is the neutron capture cross section.

The (n,γ) reactions and the reaction $^{14}\text{N}(n,p)^{14}\text{C}$ serve as the main neutron absorption mechanisms. The rates of these reactions were taken from the paper by Bao et al. (2000) and the database at http://www.nndc.bnl.gov, respectively.

The quantity γ, called hardness, which is proportional to the fraction of epithermal neutrons in the total spectrum, is used to characterize the spectrum:

$$\gamma = \frac{\Sigma_a}{\xi\Sigma_s}, \qquad (6)$$

where Σ_a and Σ_s are, respectively, the total neutron absorption and scattering cross sections per unit volume.

For a layer with solar chemical composition after the CNO-cycle reactions in its material at temperature $T_6 = 90$ and mixing of 23% of ^{12}C (see,

e.g., Goriely and Mowlavi 2000), we obtain $\gamma \approx 10^{-5}$. Clearly, the hardness increases with total neutron absorption cross section, and the fraction of epithermal neutrons in the spectrum increases.

As we pointed out above, the Petrov−Shlyakhter effect can significantly increase the rates of some of the reactions and, thus, can affect the nucleosynthesis in AGB stars.

Initially, a list from the paper by Denissenkov and Tout (2003), which includes the reactions on nuclei with small atomic numbers (from ^{1}H to ^{28}Si), was used to search for such reactions. Clearly, including epithermal neutrons can greatly increase the reaction rate if the reaction is accompanied by the production of two charged particles, because in this case the cross section can increase sharply with energy (even if the resonance effects are disregarded). Thus, it makes no sense to consider, for example, the (n, γ) reactions, because their cross section for nuclei with small atomic numbers is approximately inversely proportional to the relative velocity of the neutron and the nucleus.

Therefore, the calculations were carried out for the following three reactions: ^{14}N$(n, p)^{14}$C, ^{21}Ne$(n, \alpha)^{18}$O, and ^{25}Mg$(n, \alpha)^{22}$Ne. It turned out that, despite the significant increase in the rate of the latter reaction, epithermal neutrons change the pattern of nucleosynthesis only slightly for all of the nuclides involved in these reactions. This is because the rate of this reaction is extremely low. Allowing for the increase in its rate has virtually no effect on the concentrations of both magnesium and neon. However, this does not rule out the possible changes in the nucleosynthesis kinetics when the reactions on heavier nuclei are included (a list of candidates for such reactions with estimates of the increase in their rates at various temperatures and spectral hardnesses is given in the paper by Petrov and Shlyakhter (1986, 1988)).

Subsequently, we considered several reactions that could proceed *only* on epithermal neutrons: ^{19}F$(n, \alpha)^{16}$N$(\beta^-\overline{\nu})^{16}$O, ^{24}Mg$(n, \alpha)^{21}$Ne, ^{23}Na$(n, \alpha)^{20}F(\beta^-\overline{\nu})^{20}$Ne, and ^{14}N$(n, \alpha)^{11}$B. When averaged over the thermal spectrum, the rate of these reactions is found to be equal to zero, and they have not included previously in nucleosynthesis calculations. Including the last reaction leads to the most pronounced consequences. Its cross section (taken from the electronic database at http://www.nndc.bnl.gov) is shown in Fig. 1. It increases significantly precisely near E_0 (see formula (1)). Our calculations indicate that its flux-averaged cross section at $\gamma = 10^{-5}$ is $\approx 0.7 \times 10^{-3}$ mb; when recalculated to 10^6 helium atoms, it is ≈ 2.5 mb. Of course, this value is very low compared to the total neutron cross section calculated at this γ for the same 10^6 helium atoms ($\approx 16b$) and, thus, cannot change the neutron exposure for heavy elements. However, the capture of epithermal neutrons can play a significant role in boron production, especially if we take into account the fact that γ can increase considerably during nucleosynthesis.

3. BORON SYNTHESIS

To calculate the amount of boron being produced, we calculated the evolution of the chemical composition in the partial mixing zone between successive convective dredge-ups for a $3M_\odot$ AGB star.

We considered a homogeneous partial mixing zone with a mass density of 1000 g cm^{-3}. We assumed that there was one ^{12}C atom for ten ^{4}He atoms (Mowlavi 1999). The fraction of heavy elements was taken in accordance with the metallicity of the star. We assumed that the temperature of the matter did not change during the entire period between the flashes and that its value was $T_6 = 90$, which corresponds to an energy of about 10 keV. Detailed calculations of the chemical evolution were performed for the following elements: ^{4}He, ^{12}C, ^{13}C, ^{14}C, ^{14}N, ^{15}N, ^{16}O, ^{17}O, ^{18}O, ^{21}Ne, ^{22}Ne, ^{21}Na, ^{23}Na, ^{23}Mg, ^{24}Mg, ^{26}Mg, ^{27}Al, ^{19}F, ^{11}B. In addition, we considered two groups of elements: the first group with elements from ^{28}Si to ^{55}Mn and the second group with elements heavier than ^{54}Fe. The averaged neutron capture rate taken from the paper by Denissenkov and Tout (2003) were used for these two groups. The calculations were performed as if this was not the whole group of elements, but only one element with an averaged neutron capture cross section. A total of 65 reactions were included in the network of differential nucleosynthesis kinetic equations. We considered the following boron burning reactions: ^{11}B$(p, \alpha)^{24}$He, ^{11}B$(p, \gamma)^{12}$C, ^{11}B$(\alpha, n)^{14}$N, and ^{11}B$(\alpha, p)^{14}$C. It should be noted that, because of its high rate, the reaction ^{11}B$(p, \alpha)^{24}$He plays a major role in the boron depletion. Basic data on the reaction rates were taken from the NACRE (http://pntpm.ulb.ac.be/nacre.htm) and Caughlan and Fowler Izotope List (http://www.phy.ornl.gov/astrophysics/data/cf88/nuclei.html) databases.

It turned out that including the reaction ^{14}N$(n, \alpha)^{11}$B in the network actually gave rise to an appreciable boron concentration in the partial mixing zone. This seems rather strange at first glance, because boron is generally known to burn out even at a temperature on the order of several million Kelvins, while the temperature in the partial mixing zone is much higher.

This apparent paradox can be resolved as follows. The injected protons burn out on ^{12}C already in a few days. This gives rise to the so-called ^{13}C pocket, which interacts with helium via the reaction ^{13}C$(\alpha, n)^{16}$O to yield neutrons for the s-process. Thus, the lifetime of an intense neutron flux is determined by the lifetime of ^{13}C, which is preserved for a fairly long period even after a significant decrease in the proton concentration. As a result, the proton concentration decreases significantly almost immediately after the convective dredge-up, while the neutron flux remains high, and precisely this is required for the boron production. Indeed, the main boron depletion mechanism is the reaction of its burning on protons (p, α), while boron is produced from nitrogen through the capture of epithermal neutrons— ^{14}N$(n, \alpha)^{11}$B. Consequently, in the period under consideration, boron continues to be effectively produced, but there is virtually nothing on which it can burn: the number of protons is very small, while the rates of the boron burning reactions on helium are low.

Interestingly, the proton concentration does not reduce to zero due to the interaction of nitrogen with already thermal neutrons: ^{14}N$(n, p)^{14}$C. As a result, the boron concentration can reach 10^{-10} of the helium concentration or more. Since the observed boron concentration is of the same order of magnitude, this value is significant.

We see from Fig. 2 that the boron concentration reaches its equilibrium value about a year after the convective dredge-up (this also applies to almost all of the remaining nuclides). The question of how the equilibrium boron concentration depends on the fraction of proton contamination is of considerable interest. To answer this question, we performed appropriate calculations. Their main results are presented in Fig. 3.

In Fig. 3a, the spectral hardness γ is plotted against the mass fraction of proton contamination. Initially, the hardness rapidly increases with increasing fraction of injected protons. This is because the concentration of the main neutron absorber, ^{14}N, increases (the stronger the contamination, the more effective the reaction ^{13}C$(p, \gamma)^{14}$N, because the number of protons is enough for the CNO cycle to continue) (see Fig. 3b). When the number of protons becomes enough for the conversion of the entire ^{12}C into ^{14}N, the hardness ceases to increase. The slight decrease in hardness as the proton contamination increases further is attributable to an increase in the helium concentration and, hence, the scattering cross section. Here, the reaction ^{14}N$(p, \gamma)^{15}$O$(\beta^+\nu)^{15}$N may be ignored.

The curve in Fig. 3c can be explained by writing the balance equation for the proton and ^{11}B

concentrations. It is easy to show that the equilibrium boron concentration is proportional to the product of the hardness and the total proton capture cross section. Protons are mainly absorbed in the CN-cycle reactions: ^{12}C$(p, \gamma)^{13}$N$(\beta^+\nu)^{13}$C, ^{13}C$(p, \gamma)^{14}$N, ^{14}N$(p, \gamma)^{15}$O$(\beta^+\nu)^{15}$N, and ^{15}N$(p, \alpha)^{12}$C. For strong proton contamination, the cycle reaches an equilibrium regime, and the ^{12}C, ^{13}C, ^{14}N, and ^{15}N concentrations cease to depend on the mass fraction of the injected protons and can be easily calculated. Thus, we see from Fig. 3b that the ^{12}C and ^{14}N concentrations reach their equilibrium values even at a mass fraction of the injected protons of ~ 0.1 (the slight decrease in the mass fractions as the proton contamination increases further is attributable to the dilution of the matter in the partial mixing zone by the injected protons). Clearly, the equilibrium cross section for the reaction ^{15}N$(p, \alpha)^{12}$C per unit volume accounts for a quarter of the total proton capture cross section per unit volume. Therefore, for strong proton contaminations (≥ 0.25), the capture of about a quarter of the protons will be accompanied by the production of helium nuclei.

Ignoring the other reactions involving helium and taking the equilibrium values for the nitrogen and carbon concentrations, we can easily derive an asymptotic expression for the spectral hardness: $\gamma \sim 10^{-3}/(4 + 5X_p)$, where X_p is the mass fraction of the injected protons (see Fig. 3a). The boron mass fraction at maximum γ is $\sim 10^{-10}$. The decrease in the boron mass fraction with increasing proton contamination for strong contamination can be explained both by a decrease in hardness and by proton dilution.

The following important conclusion can be drawn from the derived dependence: regions highly enriched with hydrogen where much nitrogen is produced are most favorable for the boron production. It is interesting to note that, in contrast, a large amount of nitrogen reduces significantly the efficiency of the standard s-process, because the neutron exposure is approximately inversely proportional to the ^{14}N concentration. For this reason, the s-process can effectively proceed only in a small part of the proton contamination zone with a mass fraction of the injected protons of ~ 0.001, as distinct from boron that is produced virtually *in this entire* zone.

We see from Fig. 2 that the amount of produced boron weakly depends on the metallicity of the star even at a mass fraction of the injected protons of 0.001. At a higher initial proton concentration, the differences will be even smaller (the greater the number of injected protons, the more intense the formation of heavy elements; since the concentrations of most of these elements reach their steady-state values, the
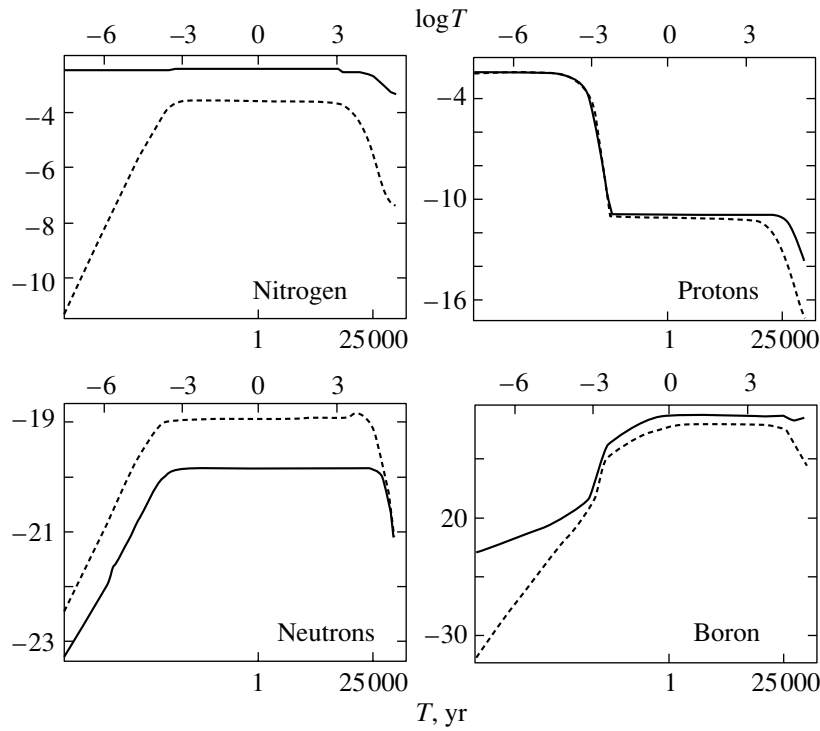
Fig. 2. Concentrations of the most important nuclides versus time (in years). The common logarithm of the ratio of the nuclide and helium concentrations is along the vertical axis. The dotted and solid lines correspond to a star of zero and solar metallicities, respectively. The mass fraction of the injected protons is 0.001.
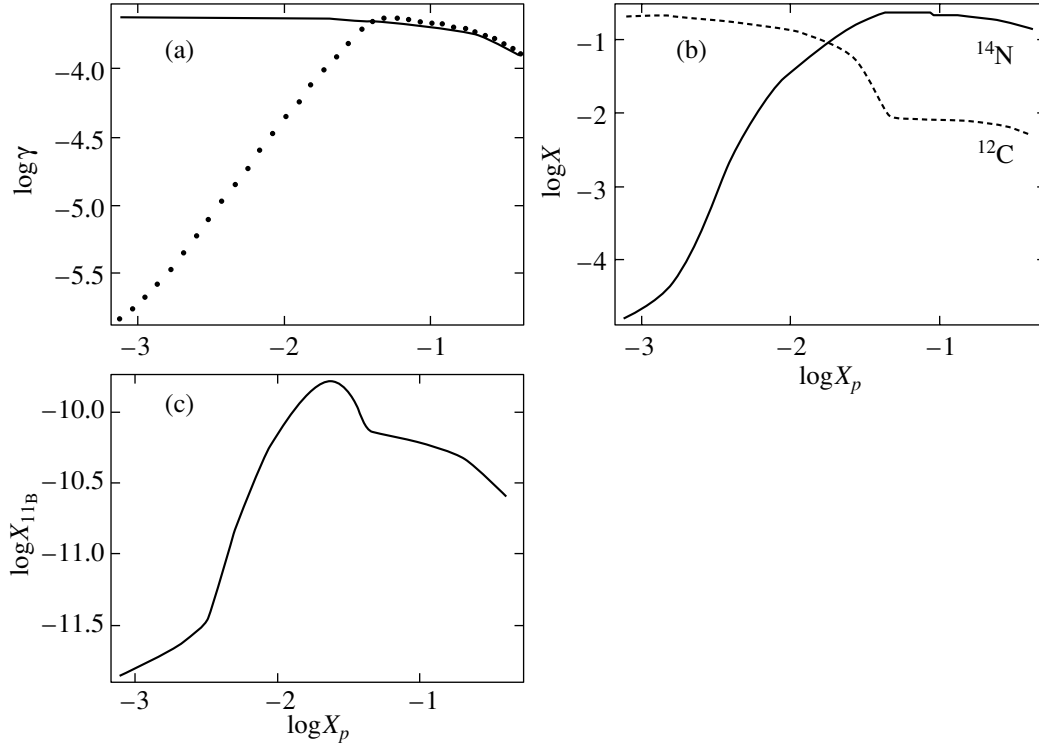
Fig. 3. Basic quantities defining the equilibrium boron concentration versus mass fraction of the injected protons X_p: (a) spectral hardness (the dots and the solid curve represent the calculated and asymptotic values, respectively); (b) the nitrogen and carbon mass fractions; and (c) the boron mass fraction.

logT
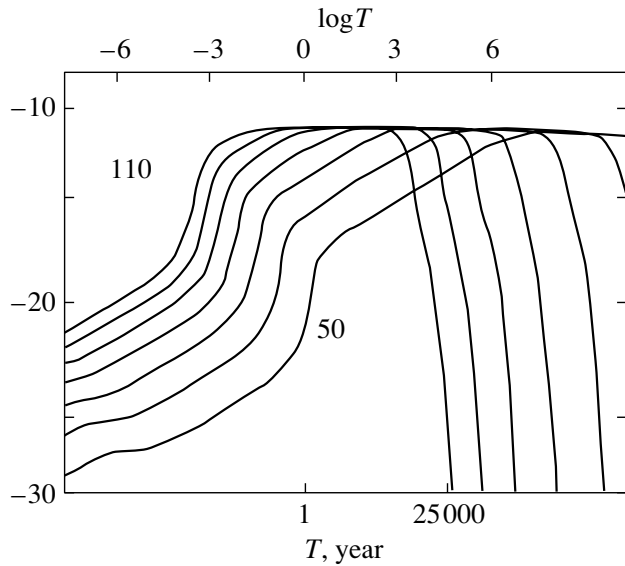
Fig. 4. Boron concentration in the partial mixing zone (vertical axis) versus time (horizontal axis) at various temperatures T_6. The units are the same as those in Fig. 2.

system virtually forgets the initial chemical composition).

4. THE TEMPERATURE DEPENDENCE OF THE BORON YIELD IN THE PARTIAL MIXING ZONE

All of the previous results were obtained for a model with a constant temperature throughout the partial mixing zone. Its value was fixed and equal to $T_6 = 90$. The question of how the boron yield depends on temperature is of considerable interest from two points of view. First, from a quantitative point of view, the rates of the main reactions change significantly even if the temperature changes slightly, and this must seemingly greatly change the concentration of the boron being produced. Second, as was noted above, the boron concentration is significant only before complete ^{13}C depletion. Many authors (see, e.g., Herwig and Langer 2000; Goriely and Siess 2001) point out that the ^{13}C-pocket completely burns out in the period between flashes, and, thus, no boron will be brought to the surface during the convective dredge-up. Our calculations have revealed that the ^{13}C lifetime at $T_6 = 90$ is slightly longer than the period between flashes, and, hence, boron will be brought to the surface. This discrepancy apparently arises from differences in the chosen parameters of the partial mixing zone. The above authors may have

taken into account the temperature rise during nucleosynthesis. It should also be noted that, for definiteness, the boron concentration in our calculations was calculated 25 000 yr after the convective dredge-up. In fact, the time interval between the dredge-ups depends on the core mass and decreases from flash to flash. The longest interval is believed to be no larger than 10^5 yr (Mowlavi 1999; Straniero *et al.* 1993). In this worst case, the boron concentration already becomes nonequilibrium, but its decrease is still moderately large (for moderate proton contaminations, no more than a factor of 10). In any case, bearing in mind the uncertainties both in the temperature and density in the partial mixing zone and in the ^{13}C burning rate, the assertions about its complete depletion by the end of the nucleosynthesis between flashes seem too categorical.

Clearly, the ^{13}C burning time strongly depends on temperature. Therefore, performing calculations at its various values, we can establish the range of temperatures at which boron is effectively brought to the surface.

In Fig. 4, the boron concentration is plotted against time at various temperatures. The extreme right curve corresponds to the lowest temperature. The temperature then rises by 10^7 K for each following curve. The proton mass fraction is 0.01. We see that the maximum boron concentration is virtually independent of temperature. In contrast, the time after which boron is completely depleted strongly depends on temperature. In fact, only the nucleosynthesis time scale changes with temperature. This is because the rates of some of the main reactions on charged particles increase with temperature approximately equally, while the neutron capture reaction rates decrease only slightly. Finally, the rate of the boron production reaction ^{14}N$(n, \alpha)^{11}$B is virtually independent of temperature, because this reaction proceeds only on epithermal neutrons. Therefore, nucleosynthesis will proceed as if the temperature in the partial mixing zone did not change, but the decrease in time scale accompanied by an approximately equal decrease in the rates of all neutron capture reactions occurred. Clearly, the latter will just increase the neutron concentration, but will not change the concentrations of other nuclides in any way.

Our calculations lead us to conclude that boron will be effectively brought to the surface if $T_6 \leq 100$ (see Fig. 4).

5. BORON REMOVAL FROM THE PARTIAL MIXING ZONE

All of the previous models contained the mass fraction of the injected protons as a free parameter.

For the total amount of produced boron to be calculated, its concentration must be averaged over the entire proton contamination zone.

Clearly, the part of the partial mixing zone closer to the hydrogen source must be contaminated more strongly. However, since the nature of the partial mixing through which contamination takes place is not yet clear, the depth profile of the proton concentration cannot be accurately described. For definiteness, the proton mass fraction is commonly assumed to decrease exponentially from 0.7 at the upper boundary of the proton contamination zone to 10^{-6} at its lower boundary (Mowlavi 1999; Goriely and Siess 2001; Denissenkov and Tout 2003). It should be noted that the assumption about an exponential behavior of the contamination has no reliable physical justification. In general, it is pointed out that the proton concentration profile weakly affects the synthesis of elements in the s-process (Goriely and Mowlavi 2000). This is not quite clear, because the s-process, as we noted above, intensively proceeds only in a rather narrow range of proton concentrations. In contrast, the mass of the matter contaminated with the appropriate proton concentration for nucleosynthesis, obviously, depends on the shape of the profile. On the other hand, boron is synthesized virtually throughout the proton contamination zone, and its concentration depends modestly on the fraction of the injected protons. Therefore, the influence of the proton concentration profile on the boron synthesis is much weaker than it is on the synthesis of s-process elements, and the arbitrary assumption of an exponential profile will not lead to a significant error. The mean boron mass fraction obtained with this profile is 3×10^{-11}.

Two main parameters are responsible for the total amount of boron removed from the partial mixing zone. The first parameter, λ_{PM} (PM stands for partial mixing), specifies the ratio of the mass of the partial mixing zone to the mass of the matter between the shell sources ($\sim 0.02 M_\odot$). In fact, this parameter describes the semi-convection intensity. The second parameter, λ_{DUP}, directly specifies the intensity of the matter removal during a convective dredge-up. It is defined as the ratio of the mass removed during a convective dredge-up to the total mass of the matter between the shell sources. It is commonly assumed that $\lambda_{PM} = 0.05$ and $\lambda_{DUP} = 0.1-1$ (Blocker 1999). Using all of these numbers, we can easily estimate the boron mass that will be removed during each convective dredge-up, $\sim 10^{-13} M_\odot$.

We can also estimate the total amount of boron supplied by one AFB star. Clearly, if the boron concentration in the stellar envelope is equal to the mean boron concentration in the partial mixing zone, then the total boron mass in the envelope will not change after a convective dredge-up (the amount of boron removed during the dredge-up will be equal to its amount produced during nucleosynthesis between flashes). Therefore, if the number of dredge-ups is enough for an equilibrium to be established, the boron mass fraction in the stellar envelope will be $\sim 3 \times 10^{-11}$. Due to intense stellar wind, a $3 M_\odot$ star can supply $\sim 10^{-10} M_\odot$ of boron to the interstellar medium. However, this estimate is rather speculative. Nevertheless, one may probably think that the mechanism of nucleosynthesis on epithermal neutrons under consideration, together with the standard spallation reactions, can play a significant (though apparently not crucial) role in the overall pattern of boron production in the Universe.

We specially emphasize that of greatest interest is not so much our quantitative result as the fact that we have suggested a new physical mechanism of boron synthesis *solely* on epithermal neutrons, which can effectively operate in AGB stars. It may be capable of competing with the standard spallation reactions.

The material presented in our paper is described in more detail in an expanded version of this paper accessible at http://www.astro.spbu.ru/astro/publications/agb.zip.

ACKNOWLEDGMENTS

REFERENCES

1. Z. Y. Bao, H. Beer, F. Kappeler, *et al.,* At. Data Nucl. Data Tables **76**, 70 (2000).

2. T. Blocker, *IAU Symp. No. 191: Asymptotic Giant Branch Stars,* Ed. by Le Bertre, A. Lebre, and C. Waelker (Astron. Soc. Pac., 1999), p. 21.

3. P. A. Denissenkov and C. A. Tout, Mon. Not. R. Astron. Soc. **340**, 722 (2003).

4. S. Goriely and N. Mowlavi, Astron. Astrophys. **362**, 599 (2000).

5. S. Goriely and L. Siess, astro-ph/0109091 (2001).

6. F. Herwig and N. Langer, astro-ph/0007390 (2000).

7. I. Iben, Jr. and A. Renzini, Mon. Not. R. Astron. Soc. **263**, L23 (1982).

8. R. A. Malaney, Mon. Not. R. Astron. Soc. **231**, 657 (1988).

9. N. Mowlavi, Astron. Astrophys. **344**, 617 (1999).

10. H. Olofsson, *IAU Symp. No. 191: Asymptotic Gi-
    ant Branch Stars,* Ed. by Le Bertre, A. Lebre, and
    C. Waelkons (Astron. Soc. Pacific, 1999), p. 3.

11. Yu. V. Petrov and A. I. Shlyakhter, Preprint No. 1189,
    LIYaF (Leningrad Institute of Nuclear Physics, 1986).

12. Yu. V. Petrov and A. I. Shlyakhter, Astrophys. J. **327**,
    294 (1988).

13. O. Straniero, R. Gallino, M. Busso, *et al.*, Astrophys.
    J. **440**, L85 (1995).

14. M. M. R. Williams, J. Nucl. Energy **25**, 489 (1971).

15. A. M. Weinberg and E. P. Wigner, *The Physical The-
    ory of Neutron Chain Reactors* (Univ. of Chicago
    Press, Chicago, 1959).

Translated by V. Astakhov

Kinematics and Parameters of the Gas in the Vicinity of TW Hya

S. A. Lamzin[1*], A. S. Kravtsova[1], M. M. Romanova[2], and C. Batalha[3]

[1]*Sternberg Astronomical Institute, Universitetskiĭ pr. 13, Moscow, 119992 Russia*
[2]*Astronomy Department, Cornell University, Ithaca, NY 14853, USA*
[3]*Brazil National Observatory, Rua General José Cristino 77, Rio de Janeiro, Brazil*
Received November 17, 2003

Abstract—The following conclusions about the kinematics and parameters of the gas in the vicinity of TW Hya have been drawn from an analysis of optical and ultraviolet line profiles and intensities. The accreting matter rises in the magnetosphere to a distance $z > R_*$ above the disk plane and falls to the star near its equator almost perpendicular to its plane. The matter outflows from a disk region with an outer radius of ≤ 0.5 AU. The [OI], [SII], and H_2 lines originate in the disk atmosphere outside the outflow region, where the turbulent gas velocity is close to the local speed of sound. In the formation region of the forbidden lines, $T \simeq 8500$ K and $N_e \simeq 5 \times 10^6$ cm^{-3}, and the hydrogen is almost neutral: $x_e < 0.03$. The absorption features observed in the blue wings of some of the ultraviolet lines originate in the part of the wind that moves almost perpendicular to the disk plane, i.e., in the jet of TW Hya. The V_z gas velocity component in the jet decreases with increasing distance from the jet axis from 200 to 30 km s^{-1}. The matter outflowing from the inner disk boundary, moves perpendicular to the disk plane in the formation region of blue absorption line components, at a distance of ~ 0.5 AU from the axis of symmetry of the disk. This region of the wind is collimated into the jet at a distance of < 3 AU from the disk plane. The gas temperature in the formation region of absorption components is $\simeq 2 \times 10^4$ K, and the gas density is $< 3 \times 10^6$ cm^{-3}. This region of the jet is on the order of several AU away from the disk plane, while free recombination in the jet begins even farther from the disk. The mass-loss rate for TW Hya is $\dot{M}_w < 7 \times 10^{-10} M_\odot$ yr^{-1}, which is a factor of 3 lower than the mean accretion rate. The relative abundance of silicon and aluminum in the jet gas is at least an order of magnitude lower than its standard value. © *2004 MAIK "Nauka/Interperiodica"*.

Key words: *stars—variable and peculiar; TW Hya, T Tauri stars, spectra, disk accretion, disk wind, jets.*

INTRODUCTION

TW Hya is one of the most active classical T Tauri stars (CTTSs); the equivalent width of the Hα line in its spectrum is $\simeq 200$ Å (Herbig and Bell 1988). Its age, ~ 10 Myr (Webb *et al.* 1999), is anomalously old for this type of young stars. TW Hya is the nearest known CTTS: its distance d is about 56 pc (Wichmann *et al.* 1998). According to Batalha *et al.* (2002), the spectral type of the star is K7—M1, the mass is $M_* = 0.7 M_\odot$, the radius is $R_* = 0.8 R_\odot$, and the luminosity is $L_* = 0.16 L_\odot$. The star is surrounded by a gas—dust disk; judging by the shape of its optical (Krist *et al.* 2000), infrared (Kuhn *et al.* 2001), and radio (Wilner *et al.* 2000) images, the axis of symmetry of the disk is inclined at an angle i of $5°—15°$ to the line of sight. We will assume that the rotation axes of the star and the disk coincide and that $i = 10°$.

Alencar and Batalha (2002) found a correlation between the intensity variations of the veiling continuum and the emission in the He I and Na D lines and the red Balmer line wings, which led them to conclude that they have a common origin in the accreting matter. The blue Balmer line wings also exhibited large variations. However, they do not correlate with light variations, and the authors believe variable absorption in the stellar wind to be responsible for them. In the Hubble Space Telescope (HST) and FUSE ultraviolet spectra of the star, the wind shows up much more clearly: several lines in the blue wing exhibit an absorption component that sinks below the continuum level (Herczeg *et al.* 2002).

There is no doubt that the activity of TW Hya is governed by disk accretion accompanied by mass outflow. However, the pattern of motion of the accreting and outflowing gas in the vicinity of the star has not yet been studied, nor has it been studied in young stars as a whole, which is attributable both to

*E-mail: `lamzin@sai.msu.ru`

theoretical problems and to difficulties in interpreting the CTTS spectra.

Modeling accretion requires three-dimensional MHD calculations, because the magnetic axis in CTTSs appears to be greatly inclined to the stellar rotation axis. The first calculations of this type (Romanova *et al.* 2003) have shown that, if the star has a dipole magnetic field, then even at small angles between the axes, the accretion flow loses its axial symmetry and breaks up into at least two dense streams that strike the star near its magnetic poles. The situation may turn out to be qualitatively different if the magnetic field of the star differs significantly from the dipole configuration, which seems quite possible (Smirnov *et al.* 2003). Thus, the information about the gas kinematics in the magnetosphere of TW Hya that we have obtained from observations seems of great importance.

It is generally believed that matter outflows from the accretion disk surface under the combined action of magnetic and centrifugal forces. Two types of models that describe this process are currently considered; roughly speaking, the difference between them reduces to the role of the stellar magnetic field in the wind formation (see Shu *et al.* 2000; Königl and Pudritz 2000). However, all of the models predict that matter outflows from the disk at a comparatively small angle to its surface, and, subsequently, the wind is collimated at some distance from the starting point into a quasi-cylindrical jet whose axis is perpendicular to the disk plane. Since no reliable information about viscosity and conductivity is available, the disk wind models are phenomenological, i.e., they contain a set of free parameters on which the shape of the streamlines as well as the temperature and density distributions in the wind depend. The questions about the size of the disk region from which the wind blows and about the distance at which the wind is collimated into a jet are yet to be answered. We hope that our constraints on the wind parameters of TW Hya, to some extent, will allow us to answer the above questions and to impose nontrivial constraints on the class of models and/or their free parameters.

The spectra of CTTSs in general and TW Hya in particular are difficult to interpret, because the line profiles are generally formed in several spatially separated regions with distinctly different physical and kinematic characteristics. Therefore, we give special attention to elucidating the relative contribution of various regions to the formation of a particular spectral line.

We analyze the spectra that have been studied and published previously: by Alencar and Batalha (2000) in the optical range and by Herczeg *et al.* (2002) in the ultraviolet range. A description of the observing and data reduction techniques can be found in the

above papers, and we point out only the following. The optical spectra were taken in April 2000, cover the range 3500 to 9100 Å, and have a resolution $R = \lambda/\Delta\lambda \simeq 5 \times 10^4$. The ultraviolet spectra were taken with the HST/STIS spectrograph on May 7/8, 2000, in two wavelength ranges: 2300−3100 Å ($R \simeq 3 \times 10^4$) and 1150−1720 Å ($R \simeq 5 \times 10^4$). All of the line profiles given below were corrected for the radial velocity of the star, which was assumed to be $+12.5$ km s^{-1} (Alencar and Batalha 2002).

ACCRETION

Following Alencar and Batalha (2002), we assume that the red wings of emission lines with high excitation potentials originate in the matter falling to TW Hya. Judging by the extent of the red wings of the C IV $\lambda1550$ Å, N V $\lambda1238$ Å, and O VI $\lambda1032$ Å lines (see Figs. 1a and 1b as well as Fig. 7 from Herczeg *et al.* 2002), the gas infall velocity for TW Hya reaches 400 km s^{-1}. This is possible at a magnetosphere radius $R_m > 2R_* \simeq 10^{11}$ cm. If the magnetic field strength on the stellar surface is $B \simeq 2$ kG (Johns 2002) and if the accretion rate is $\dot{M}_{ac} \simeq 2 \times 10^{-9} M_\odot$ yr^{-1} (Alencar and Batalha 2002), then it follows from formula (1) in the paper by Shu *et al.* (2000) that $R_m \sim 3 \times 10^{11}$ cm. We take this value as an estimate of the inner radius of the disk around TW Hya.

In some of the Fe II lines, for example, in the $\lambda = 2755.7$ Å line (see Fig. 1c), the red wing exhibits an absorption feature that sinks below the continuum level and extends to 400 km s^{-1}. This means that the matter falling to the star that has already reached its maximum velocity is projected onto a hot accretion spot, which is the source of emission in the continuum. Since the line of sight makes a small angle ($i = 10°$) with the axis of symmetry of the disk, we may conclude that, having entered the magnetosphere, the matter rises to a significant height ($z > R_*$) above the disk plane and falls to the star almost perpendicular to the disk plane (see Fig. 2).

For such a geometry, the magnetospheric regions that lie below the disk plane for the observer will also be seen from the Earth. Therefore, we will see the infalling matter that moves toward the observer and, hence, may be responsible for the formation of the blue emission line wings. At the same time, the magnetospheric matter above the disk plane will emit in the red wings. In addition, part of the line emission must originate downstream the accretion shock front, where the gas temperature is only a factor of 2 to 3 higher than T_{eff} and where the gas velocity relative to the photosphere is close to zero. This transition
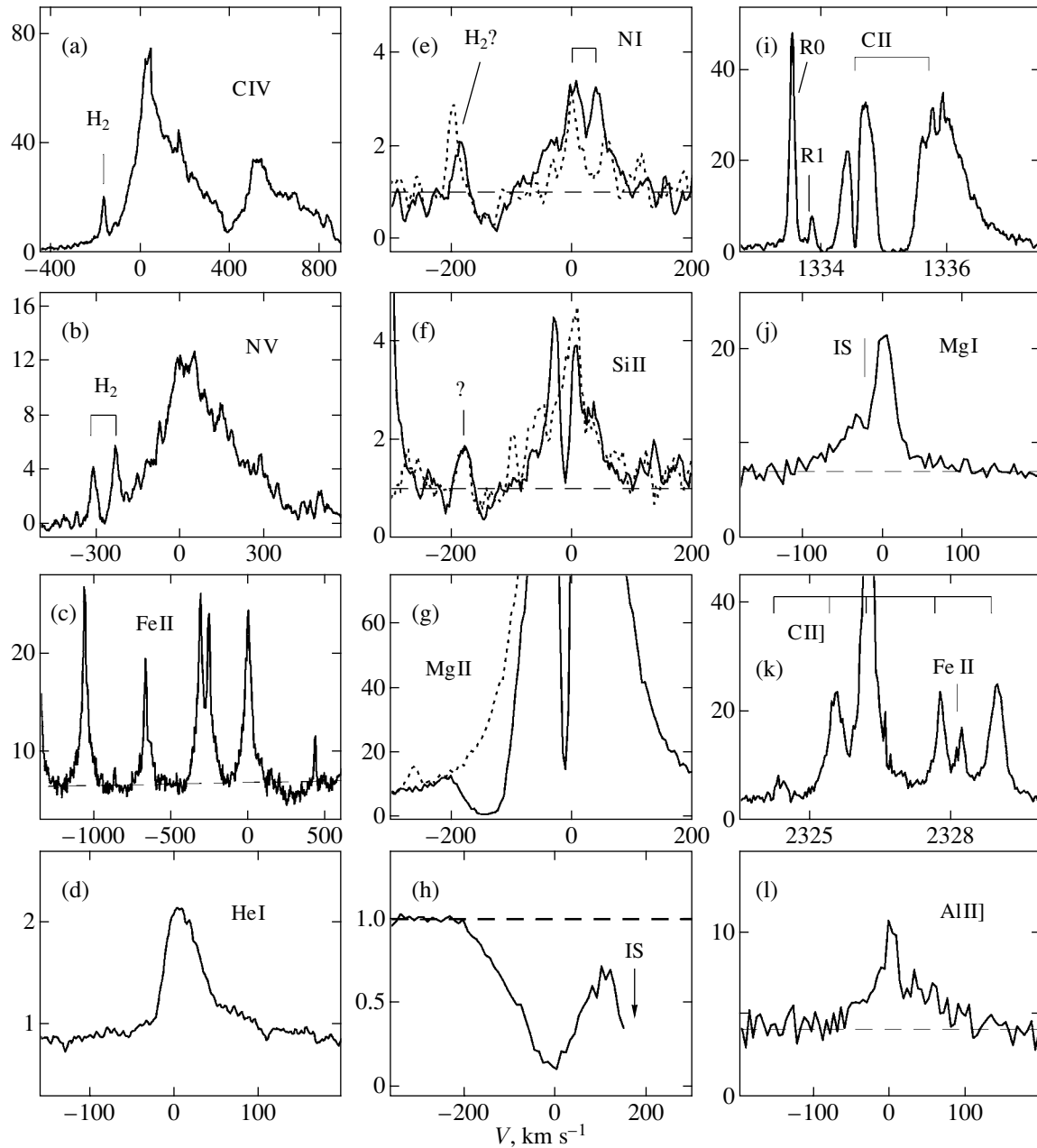
Fig. 1. Line profiles in the spectrum of TW Hya. The spectral flux density, in units of 10^{-14} erg s^{-1} cm^{-2} Å^{-1}, is along the vertical axis. Panels (d) and (h), where the fluxes were normalized to the continuum, constitute an exception. The interstellar absorption lines are marked as IS.

region between the accretion shock and the stellar atmosphere is similar to a chromosphere, because the gas in this region is almost in hydrostatic equilibrium and its temperature increases outward (Lamzin 1998, 2003). We believe that this is precisely the reason why the emission line profiles in the spectrum of TW Hya are more or less symmetric relative to the star with the peak at $V_r = 0$.

The larger the ion charge, the closer the region in which this ion has an appreciable abundance to the accretion shock front. Therefore, the star's shielding of the part of the magnetosphere below the disk plane will have a much stronger effect on the C IV $\lambda 1550$ Å, N V $\lambda 1238$ Å, and O VI $\lambda 1032$ Å lines than it will on the lines of ions with a smaller charge. This conclusion is consistent with the fact that the emission lines of, for example, Fe II have almost symmetric profiles, while the blue wings of hot lines are less intense and less extended than their red wings.

We see from Fig. 2 that, even in stars observed
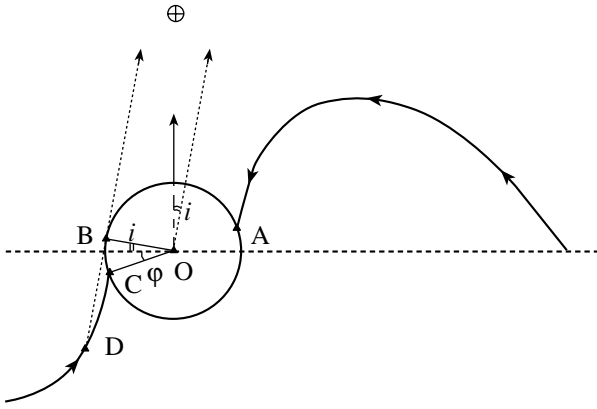
Fig. 2. Gas motion in the magnetosphere of TW Hya. Two paths along which matter falls to the stellar surface to produce a hot spot at points A and C are shown. The dashed line indicates the plane of symmetry of the disk that passes through the stellar center O. The dotted lines specify the direction to the Earth. Since line BD touches the stellar surface, segment CD of the path is not seen from the Earth.

nearly pole-on, the C^{+3}, N^{+4}, and O^{+5} lines will have relatively extended blue wings only if matter falls to a region near the stellar equator. This is probably the case for TW Hya, for which Batalha *et al.* (2002) found from an analysis of photometric data that the hot spot is located at an angular distance of $\phi \sim 20°$ from the equator.

Thus, we believe that the extended blue wings of the C III $\lambda977$ Å, C IV $\lambda1550$ Å, N V $\lambda1238$ Å, and O VI $\lambda1032$ Å emission lines originate not in a hot $(T \gg 2 \times 10^4$ K), high-velocity (up to 350 km s^{-1}) wind, but in the magnetosphere of TW Hya, i.e., in the infalling gas.

The HeI line profiles are worthy of a separate note: their blue and red wings extend to -50 and $+100$ km s^{-1}, respectively (see Fig. 1d, which shows the profile of the HeI $\lambda5876$ Å line). Since the blue wings of these lines change their shape on a time scale of the order of several hours, it would be natural to assume that they also originate in the stellar magnetosphere (Alencar and Batalha 2002).

OUTFLOW OF MATTER

Observational Manifestations of the Wind from TW Hya

As has been noted above, the blue wings of several ultraviolet lines exhibit absorption features that sink below the continuum level. Consequently, absorption takes place in the matter that moves toward the observer and that lies between the star and the Earth. Hence, it would be natural to assume that the blue

absorption features originate in the gas outflowing from the neighborhood of TW Hya.

The lines with an absorption component in their blue wings include the following: C III $\lambda977$ Å, H I Lα, the O I $\lambda1305$ Å, C II $\lambda1335$ Å, N I $\lambda1493$ Å, and Si II $\lambda1533$ Å triplet lines, as well as the Mg II $\lambda2800$ Å doublet lines and, possibly, the C I $\lambda1656$ Å line (see Fig. 7 from Herczeg *et al.* (2002) and our Figs. 1e−1g and 1f). We specially note that the blue wings of the C IV $\lambda1550$ Å, N V $\lambda1238$ Å, and O VI $\lambda1032$ Å lines exhibit no absorption component.

The absorption component in all of the lines probably extends to the shorter wavelengths up to $V_a^{min} \simeq -200$ km s^{-1}. Unfortunately, the long-wavelength boundary V_a^{max} cannot be accurately established, because the central emission feature of the line is clearly superimposed on the absorption component. To demonstrate this effect, we reflected the red wing of the Mg II h line relative to the $V_r = 0$ axis (see the dotted line in Fig. 1g) and subtracted it from the blue wing. The subtraction result is shown in Fig. 1h, where the dashed line indicates the continuum level. We now clearly see that V_a^{max} is not equal to -100 km s^{-1}, as may be concluded from Fig. 1g, but is much lower in magnitude. In this case, an accurate determination of V_a^{max} is hindered by the blending with an interstellar absorption line and, for the nonresonant lines, the superposition of H_2 emission lines and/or the low signal-to-noise ratio. Our estimate is $V_a^{max} \simeq -30$ km s^{-1}; this value probably refers to the absorption components of all of the above lines. Thus, the impression is that the absorption components of the lines with widely differing excitation potentials lie within the same velocity range $V_a^{min} - V_a^{max}$, from where we conclude that they originate in the same region of the wind.

Since the line of sight that connects TW Hya with the observer makes a small angle ($i \simeq 10°$) with the disk (Z) rotation axis, only the matter that moves almost perpendicular to the disk plane can cross this line of sight. Thus, we conclude that the blue absorption components for TW Hya originate in the part of the wind that has already been collimated into a jet. The matter that moves almost along the Z axis makes an angle $\leq i$ with the line of sight, and since it is small, we may assume that the z component of the wind velocity, V_z, and its component along the line of sight, $\simeq V_z \cos i$, are virtually equal. It thus follows that the jet of TW Hya contains streamlines that correspond to the range of velocities V_z from 30 to 200 km s^{-1}.

The Size of the Disk Wind Formation Region

Herczeg *et al.* (2002) identified 143 emission lines of molecular hydrogen in the ultraviolet spectrum of TW Hya that are excited by HI Lα photons. The H_2 lines have a symmetric shape with a full width at half maximum (FWHM) $\Delta v \simeq 12$ km s^{-1} and, within the limits of the measurement errors (2−3 km s^{-1}), the same radial velocities as those of the star's photospheric lines. Thus, it was concluded that the H_2 lines originate in the disk; an analysis of the spatial extent of the emission showed that the size of the emitting region was $R_{H_2} < 1.4$ AU. On the other hand, the absence of a double-peaked structure in the lines implies that, if the rotation in the disk is Keplerian, then (Ardila *et al.* 2002; Kravtsova and Lamzin 2002)

$$2\sqrt{\frac{GM_*}{R_{H_2}}}\sin i < \Delta v;$$

whence it follows that $R_{H_2} > 0.5$ AU.

Thus, for TW Hya, the H_2 lines are formed at a distance of $\simeq 1$ AU from the star. At the same time, the temperature in this region is $\sim 2000-3000$ K (Herczeg *et al.* 2002); therefore, the emission region is most likely the disk atmosphere heated by Lα photons. Assuming that $\Delta v \simeq 1.67 V_t$, we obtain $V_t \simeq 7.2$ km s^{-1}, which is a factor of about 1.5 higher than the thermal velocity of the H_2 molecules at this temperature. Consequently, there is turbulence in the disk region under consideration with a mean velocity close to the thermal one.

In the theory of a thin α-disk (Shakura and Sunyaev 1973), the characteristic disk thickness H_p at distance r from the star is

$$H_p = V_t r^{3/2}(GM_*)^{-1/2} \qquad (1)$$
$$\simeq 0.2 r^{3/2}\left(\frac{M_*}{0.7 M_\odot}\right)^{-1/2}\frac{V_t}{10} \text{ AU},$$

where, for numerical estimation, r is given in AU, and V_t is given in km s^{-1}. The angle β at which the disk atmosphere is seen from the star at distance $R_{H_2} = 1$ AU is then $\simeq H_p/R_{H_2} \simeq 12°$.

The total H_2 line luminosity is $\sim 7.6 \times 10^{29}$ erg s^{-1} (Herczeg *et al.* 2002). Since a fraction $\beta^2/2 \sim 0.02$ of the Lα photons flying away from the star fall within the region where these lines originate, the Lα line luminosity of TW Hya will be $\sim 4 \times 10^{31}$ erg s^{-1}, i.e., $L_{L\alpha} \sim 0.06 L_*$. This value is almost equal to the $L_{L\alpha}$ estimate obtained by Blondel *et al.* (1993) from an analysis of IUE spectrum for the star.

The absence of a noticeable blueshift in the H_2 line profiles implies that there is no wind in this region of the disk; i.e., the outer radius of the disk region from where the wind blows is $R_L < 1$ AU. The upper limit

for R_L can be refined by analyzing the intensity of the [O I] $\lambda 5577$, 6300, 6364 Å, and [S II] $\lambda 4068$ Å lines that are observed in the star's optical spectrum. The profiles of these lines are almost identical to the H_2 line profiles: they have the same FWHM Δv and a zero radial velocity relative to the star.

We calibrated the optical spectra of TW Hya in flux by calculating the mean B, V, R_c, and I_c magnitudes using values from the database by Herbst *et al.* (1994) and the corresponding constants (Allen 1973; Bessel 1979). The following continuum fluxes were obtained (in units of 10^{-13} erg s^{-1} cm^{-2} Å^{-1}): $F^c_{4400} = 1.0$, $F^c_{5500} = 1.5$, $F^c_{6400} = 2.0$, and $F^c_{7900} = 2.5$. Having determined the equivalent widths W of the lines concerned or their upper limits, we transformed W to absolute units using the dependence $F^c_\lambda(\lambda)$. Since the interstellar extinction for TW Hya is $A_V \simeq 0$ (Batalha *et al.* 2002), the ratio of the fluxes F for two lines is equal to the ratio of their luminosities L and $L = 4\pi d^2 F$.

To determine the physical conditions in the formation region of the forbidden lines, we calculated the atomic and ionic level populations. We took the transition probabilities A_{ik} and the strengths of collisional transitions Υ_{ik} for the C and O atoms from the database by Pradhan (2003); for the S atom, we took A_{ik} from the NIST database (http://physics.nist.gov) and Υ_{ik} from the paper by Zatsarinny and Tayal (2002). Similar data for the O II, C II, Si II, and S II ions were taken from the CHIANTI database (Young *et al.* 2003). The relative elemental abundance ξ_a is the standard one (Allen 1977), unless specified otherwise.

The luminosity of the optically thin line that corresponds to the $i \leftrightarrow k$ transition may be written as

$$L^{ion}_{ik} = E_{ik} A_{ik} \xi_a n_{ion} n_k N U, \qquad (2)$$

where E_{ik} is the photon energy, n_{ion} is the relative ion abundance, n_k is the relative upper-level population of the transition, N is the number of nuclei of all elements in cm^3, and U is the volume of the emitting region. Below, we always denote the absolute and relative number densities by N and n, respectively.

We estimated the fluxes in the [O I] $\lambda 5577$ and 6300 Å lines to be 1.0×10^{-14} and 8.1×10^{-14} erg s^{-1} cm^{-2}, respectively. The solid and dashed lines in Fig. 3a indicate the calculated luminosity ratio of these lines as a function of the electron density N_e for three temperatures $T_4 = T/10^4$: 0.5, 0.8, and 2.0; the dotted line indicates the observed flux ratio of $\simeq 0.12$. The intersection of the theoretical curves with the dotted straight line specifies the relationship $N_e = N_e(T)$ between the admissible values of T and N_e in the [O I] line formation region (see Fig. 3b).
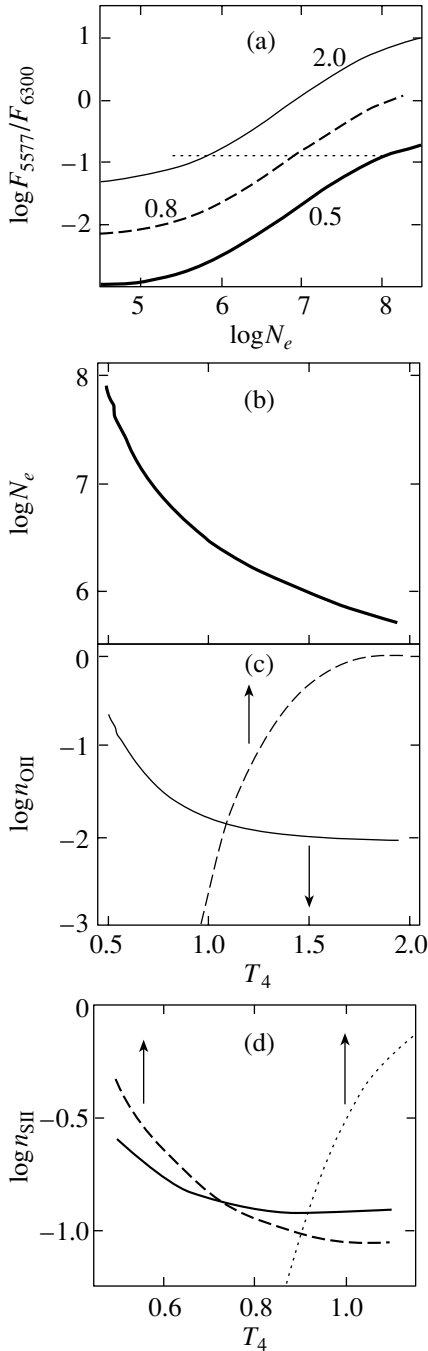
Fig. 3. Diagnostic diagrams to determine the physical conditions in the formation region of the forbidden lines for TW Hya.

We found the upper limit for the flux in the [O II] λ2470.3 Å line from the HST/STIS spectrum of the star to be 10^{-15} erg s^{-1} cm^{-2}. Using formula (2), we calculated an upper limit for the relative O$^+$ abundance for a admissible set of T and $N_e(T)$ from the ratio of the fluxes in the [O II] λ2470 Å and [O I] λ6300 Å lines. The derived dependence $n_{\mathrm{O\,II}}(T)$ is

indicated in Fig. 3c by the solid curve. Since the rate of the charge exchange reaction O$^+$ +H^0 $\longleftrightarrow$ O^0 +H$^+$ is very high and $N_e \simeq N_{H^+}$, we may assume (Osterbrock 1989) that

$$\frac{N_{\mathrm{O\,I}}}{N_{\mathrm{O\,II}}} \simeq \frac{9}{8}\frac{N_{\mathrm{H\,I}}}{N_e}.$$

Under these conditions, the relative O$^+$ abundance is approximately equal to the relative electron density $x_e = N_e/(N_e + N_{\mathrm{H\,I}})$.

The dashed curve in Fig. 3c indicates the O$^+$ abundance calculated in the coronal approximation using data from Mazzotta *et al.* (1998). Since the possibility of ionization by radiation was disregarded in these calculations (see below), the dashed curve should be considered as a lower limit for $n_{\mathrm{O\,II}}$. The intersection of the curves makes it possible to find an upper limit for the temperature in the region concerned: $T < 11\,000$ K. If the temperature in this region exceeds 5000 K, then it also follows from the figure that $n_{\mathrm{O\,I}} \simeq 1$.

The observed flux in the [S II] λ4068.6 Å line is $\simeq 5 \times 10^{-15}$ erg s^{-1} cm^{-2}. Since the profile of this line is similar to the profile of the [O I] lines, they must all originate in the same region. Calculations show that at the values of T and $N_e(T)$ concerned and at the observed F_{4069}, the fluxes in other forbidden S II lines will not exceed our estimated upper limits. Comparing the fluxes in the [O I] λ6300 Å and [S II] λ4069 Å lines using (2), we calculated the sulfur ionization fraction on condition that $n_{\mathrm{O\,I}} = 1$; to be more precise, we derived the dependence $n_{\mathrm{S\,II}} = n_{\mathrm{S\,II}}(T)$ indicated in Fig. 3d by the solid curve. The dotted curve in the same figure indicates the dependence $n_{\mathrm{S\,II}}(T)$ derived in the coronal approximation (Mazzotta *et al.* 1998), which, according to the aforesaid, should be considered as a lower limit for the S$^+$ abundance. The absence of the [S I] λ7725.1 Å line ($W < 0.020$ Å, $F < 5 \times 10^{-15}$ erg s^{-1} cm^{-2}) in the spectrum of TW Hya allows us, as in the case of oxygen, to find another lower limit for the S$^+$ abundance using (2); the corresponding dependence is indicated by the dashed curve in Fig. 3d. Judging by the pattern of intersection of the curves in the figure, the temperature in the formation region of the forbidden lines is $\simeq 8500$ K, in accordance with the initial assumption that $T > 5000$ K. It then follows from Figs. 3b and 3c that $N_e \simeq 5 \times 10^6$ cm^{-3} and $x_e < 3 \times 10^{-2}$.

The absence of the [C I] λ8727.1 Å line ($W < 0.02$ Å, $F < 6 \times 10^{-15}$ erg s^{-1} cm^{-2}) in the spectrum of the star allows us to find an upper limit for the abundance of neutral carbon using the technique described above: $n_{\mathrm{C\,I}} < 0.1$. Thus, hydrogen and sulfur in the region under consideration are weakly ionized,

while carbon is strongly ionized, although the ionization potential for carbon (11.26 eV) is higher than that for sulfur (10.36 eV). This fact can be explained if the ionization in the region concerned is mainly attributable to Lα photons with energy of $\simeq 10.2$ eV. In this case, hydrogen is ionized from the 2s and 2p levels whose population can be comparatively large due to Lα-photon pumping, while sulfur and carbon are ionized from the first excited metastable $^1D_2$ level whose populations at the derived values of T and N_e are 0.04 and 0.09, respectively. At $T = 8500$ K, the recombination coefficient for the reaction $S^+ \rightarrow S^0$ is a factor of about 1.5 smaller than that for the reaction $C^+ \rightarrow C^0$ (Nahar and Pradhan 1997; Verner and Ferland 1996), while the cross section for C^0 photoionization from the $^1D_2$ level by Lα photons must be much larger than that for neutral sulfur, for which this process has an intercombination nature; this is why sulfur has a low ionization fraction.

Thus, we have reason to believe that the heating and ionization balance in the formation region of the forbidden lines are determined mainly by Lα-photon absorption rather than by heat release in the disk. This means that, if matter outflowed from this region, then it would be heated by external radiation in the same way as would the disk atmosphere. Therefore, the absence of an extended blue wing in the [O I] λ6300 Å line, for example, implies that matter does not outflow from this region of the disk.

The luminosity in the [O I] λ6300 Å line is $\simeq 3 \times 10^{28}$ erg s^{-1}. Since $N = N_e/x_e$, for the values of T and N_e determined above and for the constraint on x_e, we find using (2) that the volume of the emitting region is $U \simeq 2 \times 10^{40} x_e < 5 \times 10^{38}$ cm^3. If the optical forbidden lines originate in the disk atmosphere, then, according to (1),

$$U = \int_{R_1}^{R_2} 2\pi r H_{\mathrm{p}} dr \simeq 1.2 \times 10^{39} \left(R_2^{7/2} - R_1^{7/2} \right) \text{ cm}^3,$$

(3)

where R_1 and R_2 are the radii of the inner and outer boundaries of the region, which are given in AU for numerical estimation. Since we have no reason to believe that only a narrow ring-shaped region emits in the disk, it would be natural to assume that R_1 is appreciably smaller than R_2. Disregarding $R_1^{7/2}$ in (3), we then obtain $R_2 < 0.7$ AU. Thus, the radius of the region where the disk wind is formed probably does not exceed 0.5 AU, which is consistent with the absence of a double-peaked structures attributable to disk rotation in the optical forbidden lines.

Fig. 4. Schematic view of the model of a cylindrical disk wind.

Line Profiles in a Cylindrical Jet

The blue absorption components of the lines in the spectrum of TW Hya originate in the part of the wind where the gas moves almost perpendicular to the disk. To estimate the parameters of this outflow region, let us consider a cylindrical, axisymmetric wind (jet) model. We introduce a cylindrical coordinate system with a star of radius R_* located at its origin whose Z axis is perpendicular to the plane of symmetry of the disk and the $\varphi = 0$ plane passes through the Z axis and the line connecting the stellar center with the Earth (see Fig. 4). The position of point K will then be specified by three coordinates: r, φ, and z.

The gas is assumed to move along the Z axis; i.e., instead of the real streamlines of the disk wind, say, ABC in Fig. 4, we assume that the gas moves along line DBC. We also assume that the wind occupies the region of space with $z \geq 0$ and $r \geq r_0 > R_*$ and that the gas velocity is constant along the z coordinate and varies with $x = r/r_0$ as a power law:

$$V = V_0 x^{-p},$$

(4)

where p is a parameter of the problem.

We will consider the formation of absorption lines in the wind in Sobolev's approximation (Sobolev 1985) by assuming that only the wind emits in the spectral line under consideration and that the star is a continuum emission source. We also assume that the absorption coefficient α_j is constant within the range $|\nu - \nu_0| < \Delta\nu/2$ and is equal to zero outside it; $\Delta\nu = 2V_{\mathrm{D}}/\lambda_0$, where V_{D} is the mean thermal

and/or turbulent velocity of the emitting atoms, and $\lambda_0 = c/\nu_0$. If the population of the upper level of the $i \leftrightarrow k$ transition is much smaller than that of its lower level N_i, then

$$\alpha_j = \sigma_0 f_{ik} \frac{N_i}{\Delta\nu}, \qquad (5)$$

where $\sigma_0 = \pi e^2/m_e c$.

We assume that the value of N_i in the jet region concerned is constant along the Z axis and varies across the jet as a power law:

$$N_i = N_i^0 x^{-k} = N_0 \xi_a n_{\rm ion}^0 n_i^0 x^{-k}, \qquad (6)$$

where N_0, $n_{\rm ion}^0$, and n_i^0 are, respectively, the gas number density (cm^{-3}), the relative ion abundance, and the relative lower-level population of the line under consideration at the inner jet surface, i.e., at $r = r_0$. In contrast to the parameter p in (4), the parameter k generally has different values for different lines.

Let $\mathbf{l}$ be a unit vector parallel to the line connecting the star with the observer (see Fig. 4). The radial velocity of the gas is then $V_l(r) = \mathbf{V} \cdot \mathbf{l} = -V(r)\cos i$, where i is the angle between the Z axis and the line of sight. In Sobolev's approximation, the line emission of the star with frequency ν will be absorbed in the wind regions located on both sides of the cylindrical $V_l = $ const surface specified by the equation

$$\nu = \nu_0 + \frac{\nu_0}{c} V_l(r).$$

The distance $\Delta l/2$ of the boundaries of this region from the cylindrical surface along the line of sight must correspond to the change in frequency by $\pm\Delta\nu/2$. Given (4), it thus follows that

$$\Delta l(r, \varphi) = 2V_D \left| \frac{dV_l}{dl} \right|^{-1} = \frac{4V_D r_0}{pV_0 |\cos\varphi| \sin 2i} x^{p+1}. \qquad (7)$$

In essence, Sobolev's approximation suggests that the stellar emission at frequency ν is absorbed in a close vicinity of the point at which the vector $\mathbf{l}$ crosses the corresponding $V_l = $ const surface; more specifically, the x and φ coordinates of this point enter into relation (7). Since the change in α_j on the segment Δl may be ignored in this case, the optical depth of the jet τ at frequency ν along the vector $\mathbf{l}$ will be $\alpha_j \Delta l$. Let $u = -V_l/V_0 \cos i$ be the radial velocity normalized to the maximum value, so that $0 \leq u \leq 1$. We then obtain from (4) and (6)

$$\tau(\nu) = \tau(u) = \frac{\tau_0}{|\cos\varphi|} u^\gamma, \quad \gamma = \frac{k - p - 1}{p}, \qquad (8)$$

$$\tau_0 = \sigma_0 f_{ik}\lambda_0 \frac{N_0 r_0}{pV_0 \sin i}(\cos i)^{(k-2p-1)/p} n_i^0 n_{\rm ion}^0 \xi_a. \qquad (9)$$

Denote the intensity of the radiation from a stellar surface element, which is assumed to be constant for simplicity, by I_c. Disregarding the jet emission, we then find that the observed monochromatic flux is

$$F_\nu = \frac{I_c}{d^2} \int_{S_*} e^{-\tau} \cos\psi \, dS_*, \qquad (10)$$

where d is the distance to the star, $\psi = \psi(r, \varphi, z)$ is the angle between the local normal to the stellar surface and the vector $\mathbf{l}$, and the integration is over the stellar hemisphere facing the Earth.

Let us introduce a spherical coordinate system whose origin coincides with the stellar center and whose polar axis $\theta = 0$ is directed toward the Earth. Only the lines of sight for which $\sin\varphi \leq R_*/r_0$ will cross the star; therefore, if $R_* \ll r_0$, then $\cos\psi \simeq \cos\theta$. Since $dS_* = 2\pi R_*^2 \sin\theta \, d\theta$, we find for the continuum-normalized absorption line profile $\mathcal{F}_u = F_\nu/F_c$ that

$$\mathcal{F}_u = \exp\left(-\tau_0 u^\gamma\right). \qquad (11)$$

According to the initial assumptions, this relation describes the line profile only for $-1 \leq -u \leq -u_{\rm min} \leq 0$, while outside this range, $\mathcal{F}_u \equiv 1$.

The shape of the absorption line profile described by Eq. (11) depends on the sign of γ. For $\gamma > 0$, the depth of the absorption feature monotonically increases with u: $\mathcal{F}_u = \exp(-\tau_0)$ reaches its minimum at $V_l = V_l^{\rm min} = -V_0 \cos i$, i.e., at $u = 1$. If, alternatively, $\gamma < 0$, then the depth of the absorption line will monotonically decrease from the center $u = 0$ toward the edge, with $\mathcal{F}_u(V_l^{\rm min})$ being still equal to $\exp(-\tau_0)$. However, the observed absorption components have bell-shaped profiles; i.e., the calculated profiles are dissimilar to the observed profiles at any value of γ (see Fig. 1). It would be natural to assume that the fact that we disregarded the jet emission is responsible for this dissimilarity. Repeating the reasoning given in Section 28 of the book by Sobolev (1985), we can show that when the jet emission is taken into account, the line profile must have a shape described by the equation

$$\mathcal{F}_u = \exp\left(-\tau_0 u^\gamma\right) + \begin{cases} A \cdot u^\delta, & \tau \gg 1 \\ \pi\tau_0 A/2 \cdot u^{\delta+\gamma}, & \tau \ll 1. \end{cases} \qquad (12)$$

Here, A and δ are the additional free parameters of the problem by varying of which (together with γ and τ_0), we were able to reproduce the observed shape of the *absorption components* of the lines whose profiles are shown in Fig. 1.

However, there are two reasons why it makes no sense to quantitatively compare the calculated profiles (12) with the observed ones. First, the stream-

lines of a disk wind at small z cannot be perpendicular to the $z = 0$ plane; i.e., the wind cannot be immediately collimated (Blandford and Payn 1982) (see the "real" streamline ABC in Fig. 4). In addition, at small z, the gas velocity must change appreciably along the streamlines. These factors are disregarded in the model under consideration. Second, all of the theoretical jet models predict the presence of a toroidal velocity component, V_φ, in the jet matter that is comparable in magnitude to the poloidal velocity V_z (Shu *et al.* 2000; Königl and Pudritz 2000). We also disregarded this circumstance.

Thus, our model is too simple for a quantitative comparison with observations. Any attempt to make it more complex will lead to the appearance of many free parameters, which will make the "improved" model virtually useless. It would be more appropriate to use the dependences $V_z(r, z)$, $V_\varphi(r, z)$, $N(r, z)$, and $T(r, z)$ derived from the calculations of the jet structure in terms of various theories to model the profiles. Garcia *et al.* (2001) followed this path by modeling the forbidden line profiles, but this allows the jet structure to be investigated only at distances >10 AU from the star due to the limited resolution of modern telescopes.

The relations derived above for a cylindrical jet with $V_\varphi = 0$ may still be used to estimate the jet parameters, because the very presence (or absence) of an absorption dip in the continuum implies that $\tau_0 > 1$ (<1) for the line in question. Indeed, at small angles i, the region at the base of the jet does not affect the formation of absorption components in the blue line wing. In addition, if $R_* \ll r_0$, then the toroidal velocity component along the line of sight is equal to zero for any dependence $V_\varphi = V_\varphi(r, z)$; therefore, relations (7)–(9) also remain valid for $V_\varphi \neq 0$. In particular, this suggests that the maximum value of the V_z velocity component in the jet of TW Hya is $V_0 \simeq 200$ km s^{-1}.

In the spectrum of TW Hya, only the H I Lα line and the C II $\lambda1335$ Å multiplet lines have an absorption dip with a flat bottom in their blue wings (see Fig. 7 from Herczeg *et al.* (2002) and our Fig. 1i). This is indicative of a large optical depth of these lines in the jet. For the Lα line, the optical depth τ is probably so large that the absorption component is broadened by the diffusion of photons into the opaque Lorenz wings of the profile (Adams 1972). In other words, we assume that the extent of the absorption dip in the Lα line up to -500 km s^{-1} is attributable to transfer effects rather than to the presence of mass flows with such a velocity. Since the optical depth for the C II $\lambda1335$ Å line is not so large, there is no absorption any longer at $V > V_0 \simeq 200$ km s^{-1}: this follows from the fact that, in contrast to the

H$_2$ $\lambda1333.80$ Å line ($\Delta V_r = 165$ km s^{-1}) discussed below, the H$_2$ $\lambda1333.48$ Å line located in the blue wing of the C II $\lambda1334.53$ Å line at distance $\Delta V_r = 235$ km s^{-1} from its center is not distorted by absorption.

Estimating the Wind Parameters

At $V_0 = 200$ km s^{-1} and $i \simeq 10°$, relation (9) takes the form

$$\tau_0 \simeq 8.0 \times 10^{-20} p^{-1} \frac{f_{ik}}{0.1} \frac{\xi_a}{10^{-5}} \frac{\lambda_0(\text{Å})}{10^3} n_i n_{\text{ion}} N_0 r_0. \tag{13}$$

In what follows, we omit the subscript 0 in n_i and n_{ion} for convenience, but these quantities still refer to the inner $r = r_0$ surface of the cylindrical jet.

For the resonance lines, we may set $n_i = 1$, but the subordinate N I $\lambda1411.9, 1492.6, 1492.8$, and 1494.7 Å lines observed in the spectrum of TW Hya require a special analysis. The first of these lines is a close blend of lines whose lower levels belong to the ^{2}P term with the excitation potential $E_i = 3.58$ eV. The presence of an absorption component in the blue wing of this blend is doubtful, but it is clearly present in the three remaining lines whose lower levels belong to the ^{2}D term with $E_i = 2.38$ eV. Like the ground ^{4}S term, ^{2}D and ^{2}P are the terms of the ground N I configuration; therefore, radiative transitions between them have a low probability ($A_{ik} < 10^{-2}$ s^{-1}). For this reason, at the densities concerned, the populations of these terms must be close to the Boltzmann population. On the other hand, the ionization potential of N I is too high to be ionized by Lα or Lβ photons from the ground metastable levels. Therefore, the ionization balance of nitrogen may be considered in the coronal approximation, as was done, for example, by Mazzotta *et al.* (1998)[1].

Consider the situation with the blend of the N I $\lambda1492.6$ and 1492.8 Å lines ($f_{ik} \simeq 0.047$). At $T_4 > 1.0$, the population of the ^{2}D term (n_{2D}) increases with temperature, while the abundance of nitrogen atoms (n_{NI}) decreases, so the product $n_{NI}n_{2D}$ is a nonmonotonic function of the temperature that reaches its maximum at $T_4 \simeq 1.3$. The presence of an absorption component implies that $\tau_0 > 1$ for this

---

[1]The role of gas photoionization in the jet by short-wavelength radiation from the accretion shock is unlikely to be significant: since, as was noted above, the line of sight crosses the accretion stream from TW Hya, photons with $\lambda < 912$ Å must be strongly absorbed while passing through the stellar magnetosphere.
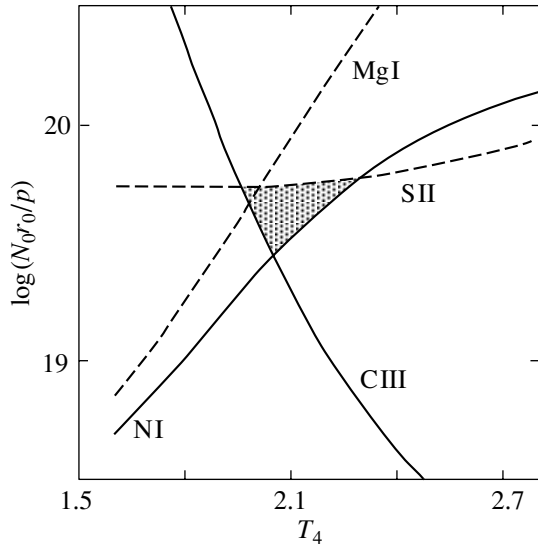
Fig. 5. Parameter $N_0 r_0/p$ versus temperature $T_4 = T/10^4$ for the N I $\lambda 1493$ Å, C III $\lambda 977$ Å, Mg I $\lambda 2852$ Å, and S II $\lambda 1260$ Å lines. The solid and dashed lines specify the lower and upper limits for $N_0 r_0/p$, respectively. The region corresponding to the admissible parameters is hatched.

blend. Therefore, relation (13) may be written in this case as

$$\frac{N_0 r_0}{p} > \frac{5.9 \times 10^{17}}{n_{\text{N I}} n_{\text{2D}}} \equiv f_N(T). \qquad (14)$$

Thus, the $f_N(T)$ curve shown in Fig. 5 specifies the lower limit for $N_0 r_0/p$ as a function of the gas temperature at the point where the line of sight to the star crosses the inner jet boundary.

A similar curve for the lower limit of $N_0 r_0/p$ is shown in Fig. 5 for the C III $\lambda 977$ Å resonance line whose blue wing also exhibits an absorption component. For this line, $n_i = 1$ and the T dependence of n_{CIII}, as in all the succeeding cases, was taken from the paper by Mazzotta *et al.* (1998). The absence of absorption dips in the blue wings of the Mg I $\lambda 2852$ Å and S II $\lambda 1260$ Å lines implies that $\tau_0 < 1$ for these lines. Thus, we can draw the curves that limit $N_0 r_0/p$ from above; these curves are indicated by dashed lines in Fig. 5. Since the intersection of the four curves highlights the domain of admissible T and $N_0 r_0/p$, we may say with confidence that $N_0 r_0/p \simeq 4 \times 10^{19}$ cm^{-2} and $T \simeq 2 \times 10^4$ K.

For these parameters, the value of τ_0 calculated for several resonance lines with large f_{ik} using formula (13), such as Ca II K, P I $\lambda 1680$ Å, P II $\lambda 1311$ Å, C IV $\lambda 1548$ Å, S I $\lambda 1487$ Å, and some others, proves to be much smaller than unity, which explains the absence of absorption components in

their blue wings. Relation (13) also predicts that, if the population of the Fe$^+$ lower ($E_i < 4.7$ eV) levels is described by the Boltzmann distribution[2], then even the strongest Fe II lines will not have absorption components, which is actually the case. On the other hand, we find for the O I $\lambda 1302$ and Mg II h and k lines, which exhibit absorption components, that τ_0 must be ~ 25 and 10, respectively, while for the C II $\lambda 1335$ Å resonance multiplet lines, it will be larger by another order of magnitude, as might be expected (see above).

Thus, for the parameters found, we can explain the presence or absence of absorption components in most of the lines. Only the Al II $\lambda 1671$ Å and Si II lines constitute an exception. For example, the depth of the absorption component in the Si II $\lambda 1533$ Å line is approximately the same as that in the N I $\lambda 1493$ Å line (see Fig. 1). Therefore, it would be natural to expect that τ_0 for it will be the same as that for the N I $\lambda 1493$ Å line, i.e., $\sim 1-2$, but formula (13) yields an order of magnitude larger value. The discrepancy is even larger for the Al II $\lambda 1671$ Å line: it has no absorption component, while, according to (13), its value of τ_0 must be ~ 25! To eliminate this contradiction, the Al and Si abundances in the wind gas may be assumed to be much lower than the standard value, because these elements constitute the dust grains. Note that Al and Si belong to elements with high condensation temperatures; the aluminum underabundance in the interstellar gas can reach three orders of magnitude (Spitzer and Jenkins 1975).

Since there is a possibility that the elemental abundance in the jet differs from the standard abundance, the question arises as to whether the values of $N_0 r_0/p$ and T estimated by assuming the standard abundance are correct. However, we see from Fig. 5 that, in essence, the lines of C, N, and S whose underabundance in the interstellar gas is at a minimum (Spitzer and Jenkins 1975) form the basis for the estimate. This gives hope that we did not err strongly in estimating the parameters.

We estimated the gas velocity in the jet (to be more precise, its poloidal component V_z) to lie within the range 30 to 200 km s^{-1}. On the other hand, the disk region from where the wind blows lies within the range $\simeq 3 \times 10^{11}$ cm to $\simeq 0.5$ AU. Therefore, it would be natural to assume that $V_z \propto r_d^{-1/2}$, where r_d is the radius of the point on the disk at which

---

[2]All of the levels up to $E_i \simeq 4.7$ eV for Fe$^+$ have the same parity; as a result, radiative transitions between them have a low probability. Therefore, it would be natural to assume that their population in a dense gas is determined by collisions and does not differ greatly from the Boltzmann population.

the corresponding streamline starts. Incidentally, the disk wind model predicts precisely this dependence $V_z(r_d)$ (Garcia *et al.* 2001). Thus, we assume that the exponent p in law (4) does not differ greatly from $1/2$ either. In this case, $N_0 r_0 \simeq 2 \times 10^{19}$ cm^{-2}.

Kastner *et al.* (1999) found that the absorption of X-ray emission from TW Hya is variable and, therefore, takes place not in the interstellar medium, but in the vicinity of the star. They estimated the column density of the absorbing atoms in the stellar envelope, $\mathcal{N}_H = \int N dl \simeq N_0 r_0 / \sin i$, to change from 5×10^{20} to 3×10^{21} cm^{-2}. In other words, according to their estimate, $N_0 r_0 > 9 \times 10^{19}$ cm^{-2}, which is a factor of 4 to 5 higher than our value. The difference may be attributed to variability if the wind intensity when the ultraviolet spectra being analyzed were obtained was lower than that during the X-ray observations (several years earlier). However, it is worth noting that Kastner *et al.* (1999) analyzed the X-ray emission with energy above 0.5 keV whose absorption cross section is $< 7 \times 10^{-22}$ cm^2 (Morrison and Mc-Cammon 1983). This means that the optical depth of the jet at $E > 0.5$ keV for $\mathcal{N}_H < 2 \times 10^{21}$ cm^{-2} is smaller than unity; therefore, the reliability of the results by Kastner *et al.* (1999) may be called into question. Observations at softer energies are required to reliably estimate $\mathcal{N}_H$.

In the spectrum of TW Hya, the intensities of the H$_2$ lines with a common upper level are related as their Einstein coefficients A_{ki} (Herczeg *et al.* 2002). The B0-4 R(1) $\lambda = 1333.80$ Å line, whose intensity is a factor of 6 lower than its expected value, constitutes an exception. Since this line lies in the blue wing of the C II $\lambda 1334.53$ Å line ($\Delta V = 165$ km s^{-1}, $u \simeq 0.83$), Herczeg *et al.* (2002) concluded that its anomalously low intensity is attributable to absorption in the wind. It has been previously shown that $\tau_0 > 100$ for the C II $\lambda 1334.53$ Å line; since, according to (9), $\tau \propto 1/\cos\varphi$, we conclude that the jet must almost completely absorb the B0-4 R(1) line emission at any φ.

Denote the radius of the cylinder on which the gas velocity in the jet is $0.83V_0$. by $r_{0.83}$. Reversing the ray path, we may say that this cylinder casts an opaque shadow that partially shields the ring on the $z \simeq 0$ plane with an outer radius of $R_{H_2} \simeq 1$ AU within which the H$_2$ lines are formed. It follows from Fig. 6a that, if $r_{0.83} < R_{H_2}$ and if the ring is thin, then the jet cannot shield more than half of the observed emission. If, alternatively, the ring is wide, then the ratio of the observed flux in the B0-4 R(1) line to the expected flux ($\xi_{H_2} \equiv 1/6$) is related to the parameters $r_{0.83}$ and R_{H_2} by

$$\alpha + \cos\alpha + \frac{\pi}{2}\sin^2\alpha = \pi\left(1 - \xi_{H_2}\right), \quad (15)$$

where $\sin\alpha = r_{0.83}/R_{H_2}$, which yields $r_{0.83}/R_{H_2} \simeq 0.83$.

At $r_{0.83} > R_{H_2}$, the B0-4 R(1) line will be seen only if the opaque jet starts from a certain height h above the disk plane (see Figs. 6b and 6c). In this case, it is easy to derive a relation similar to (15), but it is virtually useless, because h and $r_{0.83}$ cannot be determined individually from it. Thus, we may only conclude from the anomalously low intensity of the H$_2$ $\lambda 1333.80$ Å line that $r_{0.83} > 0.8$ AU.

This inequality leads us to several important conclusions. First of all, setting $p = 0.5$, we obtain $r_0 > 0.5$ AU from (4), and, hence, the inner part of the disk wind is collimated at a distance of less than 3 AU from the disk plane. We find from the condition $N_0 r_0 \simeq 2 \times 10^{19}$ that the gas density at the inner jet boundary is $N_0 < 3 \times 10^6$ cm^{-3}. If the minimum gas velocity on the periphery of the jet is $\simeq 30$ km s^{-1}, then at $p = 0.5$ and $r_0 = 0.5$ AU, the radius of the outer jet boundary is found from (4) to be $R_j \sim 10$ AU, a value typical of CTTSs. Finally, we may conclude that the region with $T \simeq 2 \times 10^4$ K at $u \leq 0.83$ lies at a distance $z > R_{H_2} \cot i \simeq 6$ AU above the disk plane (see Fig. 6b).

Estimating the Mass-Loss Rate in the Jet

We estimated $N_0 r_0 / p$ and the gas temperature by assuming that the ion abundance corresponded to coronal equilibrium. Meanwhile, the ionization fraction of some of the elements in CTTS jets far from the star is known to be much higher than that for coronal equilibrium at the observed temperature (Bacciotti *et al.* 1996). The reason is that the gas temperature in the jet at a certain distance from the star falls rapidly, while the ionization fraction along the jet subsequently changes in the regime of free recombination. In particular, the change in hydrogen ionization fraction in this regime is described by the equation (Bacciotti and Eislöffel 1999)

$$\frac{DN_e}{Dt} = V\frac{dN_e}{dz} = -\alpha_H N_e^2. \quad (16)$$

Since the angular resolution of current telescopes is not high enough for the jet parameters to be determined at $z < 10$ AU, we do not know from which minimum distance the approximation of coronal equilibrium ceases to be applicable.

Let us assume that at the $z = 0$ level from which free recombination begins, the hydrogen in a cylindrical jet is completely ionized, i.e., $N_e(r, z = 0) \simeq$
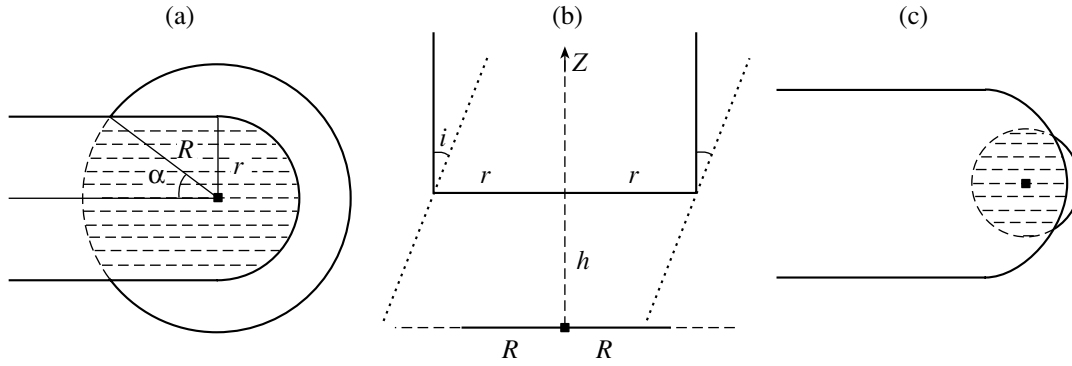
Fig. 6. Schematic view of the shielding of the H_2 emission region by the jet; the jet radius r is smaller than the outer radius of the emitting region R (a), $r > R$—side view (b) and top view (c). The quantities r and R indicated in the figure are denoted in the text as $r_{0.83}$ and R_{H_2}, respectively.

$N(r)$. In addition, the change in gas density across the jet is assumed to be described by a relation similar to (6), i.e.,

$$N = N_0 x^{-k}. \qquad (17)$$

Using (4), we may then write the solution of Eq. (16) as

$$N_e(r, z) = \frac{N_0}{x^k + x^p z / z_0}, \quad z_0 = \frac{V_0}{\alpha_H N_0}. \qquad (18)$$

The line of sight to the star crosses the inner $r = r_0$ boundary of the jet at the point with coordinates $x = 1, \varphi = 0, z = r_0 \cot i \simeq 6 r_0$. If ionization balance sets in before this point, then, according to (18), the hydrogen ionization fraction at this point will be

$$\frac{N_e}{N_0} = \left(1 + 6 r_0 N_0 \alpha_H V_0^{-1}\right)^{-1}.$$

For $\alpha_H \simeq 2 \times 10^{-13}$ cm^3 s^{-1} (Osterbrock 1989) and $N_0 r_0 > 10^{19}$, we then obtain $N_e / N_0 < 0.6$.

However, this conclusion is inconsistent with the presence of an absorption component in the C III $\lambda 977$ Å line. Indeed, according to (13), $\tau_0 \simeq 3 \times 10^3 n_{C3}$ for this line, where n_{C3} is the relative C^{+2} abundance. It thus follows for $\tau_0 \geq 1$ that $n_{C3} > 3 \times 10^{-4}$. If the jet plasma is in free recombination, then for the change in C^{+2} density we may write

$$V \frac{dN_{C3}}{dz} = -\alpha_{C3} N_{C3} N_e,$$

where α_{C3} is the recombination coefficient for C^{+2}, which in combination with (16) yields

$$n_{C3} = \frac{N_{C3}(z)}{N_{C3}(0)} = \left[\frac{N_e(z)}{N_e(0)}\right]^{\alpha_{C3}/\alpha_H}.$$

Since $\alpha_{C3} \simeq 6 \times 10^{-12}$ cm^3 s^{-1} (Nahar and Pradhan 1997), even if $n_{C3}(0) = 1$, $n_{C3} < 10^{-6}$ at the point at which the line of sight crosses the inner

jet surface, i.e., much smaller than that required for the presence of an absorption component in the C III $\lambda 977$ Å line.

Thus, for TW Hya, free recombination begins above the line connecting the star with the observer. Therefore, when estimating the ion abundance, we had the right to use the coronal approximation, and our conclusion about a high ($T \simeq 2 \times 10^4$ K) gas temperature in the jet seems trustworthy.

It would be natural to expect that the gas is heated as it outflows from the disk atmosphere, but the mass density in this region is fairly high. Therefore, we may assume that the wind temperature at small z will be comparatively low, and that atoms rather than ions must mainly emit here. An asymmetry in the Mg I $\lambda 2852$ Å line profile may be evidence for this: as we see from Fig. 1j, its blue wing extend to -100 km s^{-1}, while its red wing extends only to $+50$ km s^{-1}. Since the size of the region occupied by the wind increases greatly as the outflowing gas recedes from the disk plane, the wind matter will unlikely be heated appreciably even if it is heated by Lα emission from the accretion shock. The fact that the gas temperature in the jet rises to $\simeq 2 \times 10^4$ K probably stems from the gas heating during collimation when the direction and, possibly, magnitude of the gas velocity change greatly under the magnetic-field effect.

Since hydrogen must be almost completely ionized at $T \simeq 2 \times 10^4$ K (Mazzotta *et al.* 1998), it makes sense to use information about the radio emission from TW Hya to estimate the jet parameters. The only radio observation of the star was carried out on January 30, 1991 at frequencies of 1.49, 4.86, and 8.44 GHz (Rucinski 1992). Only upper limits for the radio fluxes were obtained; the most informative of them is the flux at $\nu = 8.44$ GHz: it was less than 8.4×10^{-31} W m^{-2} Hz^{-1} at the 3σ level, which

corresponds to an upper luminosity limit $L_\nu < 3.1 \times 10^{14}$ erg s^{-1} Hz^{-1}.

Let us estimate the optical depth of the jet at a frequency of 8.44 GHz. Since the bulk of the wind matter is strongly ionized, we assume that $N_e \simeq N = N_0 x^{-k}$. The optical depth of the wind along the line of sight to the star is then

$$\tau_{\mathrm{ff}} = \frac{1}{\sin i} \int\limits_{r_0}^{R_j} k_{\mathrm{ff}}^0 N_e^2 \mathrm{d}r \sim 6 \times 10^{-27} r_0 N_0^2, \quad (19)$$

where $k_{\mathrm{ff}}^0 \simeq 1.3 \times 10^{-27} T_4^{-1.35}$ cm^{-1} is the free−free absorption coefficient (Kaplan and Pikel'ner 1979), and R_j is the outer radius of the jet. When estimating the integral, we assumed that the optical depth was accumulated at the base of the jet. Since $N_0 r_0 \simeq 2 \times 10^{19}$ cm^{-2} and $r_0 > 0.5$ AU, we obtain $\tau_{\mathrm{ff}} \sim 3 \times 10^{12}/r_0 < 1$; i.e., the jet is transparent for radio emission with $\nu = 8.44$ GHz.

Let us estimate the radio luminosity of the part of the jet in which free recombination has not yet begun, i.e., the region with $z < r \cot i$. Denote the characteristic extent of this region along the z axis by Δz and the spectral power of the free−free emission at $\nu = 8.44$ GHz per proton (Kaplan and Pikel'ner 1979) by $\varepsilon_{\mathrm{ff}} N_e \simeq 3.4 \times 10^{-39} T_4^{-0.35} N_e$ erg s^{-1} Hz^{-1}. We then obtain

$$L_\nu = 2\pi \varepsilon_{\mathrm{ff}} \Delta z \int\limits_{r_0}^{R_j} N_e^2 r \mathrm{d}r \sim 2\pi \varepsilon_{\mathrm{ff}} \Delta z N_0^2 r_0^2. \quad (20)$$

Hence, we find that $\Delta z < 4 \times 10^{13}$ cm; i.e., the characteristic extent of the region with a temperature $T \simeq 2 \times 10^4$ K along the z axis is on the order of 1−3 AU.

A similar conclusion can also be drawn from the fact that the optically thin C II] $\lambda 2325$ Å quintet and Al II] $\lambda 2669$ Å lines exhibit no emission in their blue wings beyond $V_r = 50$ km s^{-1} (see Figs. 1k and 1l). In particular, for the C II] $\lambda 2323.5$ Å line, the upper luminosity limit in the range -200 to -50 km s^{-1} is $\sim 10^{28}$ erg s^{-1}. It follows from our calculations that the intensity of the emission in this line at $T_4 \simeq 2$ and $\log N_e < 7$ may be represented as $\varepsilon_{2324} \simeq 3 \times 10^{-25} N_e^2$, which allows a similar estimate to be obtained for Δz using a formula similar to (20).

We emphasize that the absence of blue wings in the C II] $\lambda 2323.5$ Å line imposes a severe upper limit on $N_0 r_0$. Therefore, we cannot reconcile our estimate of this quantity with the estimate by Kastner et al. (1999) by assuming that $p > 0.5$. In other words, we insist that our value of $N_0 r_0$ is actually lower than that from Kastner et al. (1999) and, thus, we assert that $p \leq 0.5$.

Whatever the gas heating mechanism at the base of the jet might be, its efficiency must be negligible at a large distance z_{max} from the disk plane, and free recombination will set in at $z > z_{\mathrm{max}}$. Since the gas is almost completely ionized up to this distance, the number of protons crossing the $z = z_{\mathrm{max}}$ plane per unit time is $\dot{M}_{\mathrm{w}}/m_p$, where

$$\dot{M}_{\mathrm{w}} = \int\limits_{r_0}^{R_j} m_p N(r) V(r) 2\pi r dr \quad (21)$$

is the mass-loss rate in the jet.

To the point of recombination, each proton will emit energy $t_{\mathrm{rec}} \varepsilon_{\mathrm{ff}} N_e$, where $t_{\mathrm{rec}} = 1/\alpha_{\mathrm{H}} N_e$ is the recombination time scale, in a 1-Hz frequency band near $\nu = 8.44$ GHz. Since each proton will eventually recombine and the jet is transparent for radio emission, the radio luminosity L_ν^{ff} of this part of the jet is related to the mass-loss rate by

$$\dot{M}_{\mathrm{w}} = \frac{m_p \alpha_{\mathrm{H}}}{\varepsilon_{\mathrm{ff}}} L_\nu^{\mathrm{ff}}. \quad (22)$$

Since $L_\nu^{\mathrm{ff}} \leq L_\nu$, we obtain $\dot{M}_{\mathrm{w}} < 7 \times 10^{-10} M_\odot$ yr^{-1}. Relation (22) can be rigorously derived from (18), (20), and (21) if $T(r, z) = $ const, which, however, is not a serious constraint, because α_{H} and $\varepsilon_{\mathrm{ff}}$ depend weakly on temperature.

The outflow rate $\dot{M}_{\mathrm{w}}$ can be independently estimated by assuming that the integral in (21) is accumulated near the inner jet boundary. In this case, $\dot{M}_{\mathrm{w}} \sim 2\pi m_p N_0 V_0 r_0^2$, which at $r_0 \simeq 0.5$ AU yields $\dot{M}_{\mathrm{w}} \sim 5 \times 10^{-10} M_\odot$ yr^{-1}, in agreement with the upper limit obtained.

CONCLUSIONS

We have drawn the following conclusions about the kinematics and physical parameters of the gas in the vicinity of TW Hya from an analysis of optical and ultraviolet line profiles.

(1) The inner boundary of the accretion disk is at a distance $R_m \sim 3 \times 10^{11}$ cm $\sim 5 R_*$ from the stellar center. Being frozen in the star's magnetic field lines, the disk matter rises in the magnetosphere to a height $z > R_*$ above the disk plane and falls to the star near its equator almost perpendicular to the disk plane.

(2) The C^{+3}, N^{+4}, and O^{+5} emission lines originate in the stellar magnetosphere; their blue wings, which extend to -350 km s^{-1}, are formed in the part of the magnetosphere that lies below the disk plane for the observer.

(3) The [O I] $\lambda 5577$, 6300, 6364 Å and [S II] $\lambda 4068$ Å lines observed in the spectrum of TW Hya

originate in the atmosphere of the disk outside the outflow region. In the formation region of the forbidden lines, $T \simeq 8500$ K, $N_e \simeq 5 \times 10^6$ cm^{-3}, and hydrogen is almost neutral: $x_e < 0.03$. The gas in this region is most likely heated and ionized not through heat release in the disk, but by accretion-shock-produced Lα photons. The lines of molecular hydrogen are also formed in the atmosphere of the accretion disk at a distance of ∼1 AU from the star through the heating of this region by Lα radiation from the accretion shock. The turbulent gas velocity in the disk atmosphere in the formation region of the forbidden and H$_2$ lines is close to the local speed of sound.

(4) The Lα line luminosity of TW Hya is ∼4 × 10^{31} erg s^{-1}, which accounts for ≃6% of the bolometric luminosity of TW Hya.

(5) Matter outflows from a disk region whose outer radius does not exceed ≃0.5 AU.

(6) The absorption features observed in the blue wings of some of the ultraviolet lines originate in the part of the wind that moves almost perpendicular to the disk plane, i.e., in the jet of TW Hya. The poloidal gas velocity V_z in the jet decreases with increasing distance from the jet axis from 200 to 30 km s^{-1}. The velocity component V_z for a streamline and the distance r_d to the star at which this streamline emerges from the disk are probably related by $V_z \propto r_d^{-1/2}$.

(7) The product of the radius r_0 of the inner jet boundary by the gas density N_0 at this radius is 4 × $10^{19}p$ cm^{-2}, where p is the exponent in law (4) of the velocity variations across the jet; we assume that $p \le 0.5$.

(8) We have received observational confirmation that matter outflows at a comparatively small angle to the plane of symmetry of the disk. To be more precise, we found that the matter outflowing from the inner disk boundary ($r \sim 3 \times 10^{11}$ cm) in the formation region of the line absorption components moves perpendicular to the disk plane at a distance of ∼0.5 AU from the axis of symmetry of the disk. This region of the wind is collimated into a jet at a distance $z < 3$ AU from the disk plane.

(9) The gas temperature in the formation region of the absorption components is ≃2 × 10^4 K, and the gas density is <3 × 10^6 cm^{-3} even at its inner boundary. The heating of the wind gas to such a high temperature is probably related to the wind collimation. This region of the jet is on the order of several AU away from the disk plane, and free recombination in the jet begins even farther from the disk.

(10) The mass-loss rate for TW Hya is $\dot{M}_w <$ $7 \times 10^{-10} M_\odot$ yr^{-1}, which is a factor of 3 lower than the mean accretion rate.

(11) The relative silicon and aluminum abundance in the jet gas is at least an order of magnitude lower than its standard value. The anomalously low intensity of the Si IV λ1400 Å doublet lines probably suggests that silicon is also underabundant in the accreting gas (Herczeg *et al.* 2002). This conclusion is consistent with the results by Calvet *et al.* (2002). These authors found that the inner regions of the disk around TW Hya contain an anomalously small amount of dust, probably because a fairly large planet has formed in the disk at a distance of ∼4 AU.

ACKNOWLEDGMENTS

REFERENCES

1. T. F. Adams, Astrophys. J. **174**, 439 (1972).
2. S. H. P. Alencar and C. Batalha, Astrophys. J. **571**, 378 (2002).
3. C. W. Allen, *Astrophysical Quantities*, 3rd ed. (Athlone Press, London, 1973; Mir, Moscow, 1977).
4. D. R. Ardila, G. Basri, F. M. Walter, *et al.*, Astrophys. J. **566**, 1100 (2002).
5. F. Bacciotti and J. Eislöffel, Astron. Astrophys. **342**, 717 (1999).
6. F. Bacciotti, G. A. Hirth, and A. Natta, Astron. Astrophys. **310**, 309 (1996).
7. C. Batalha, N. M. Batalha, S. H. P. Alencar, *et al.*, Astrophys. J. **580**, 343 (2002).
8. M. S. Bessel, Publ. Astron. Soc. Pac. **91**, 589 (1979).
9. R. D. Blandford and D. G. Payn, Mon. Not. R. Astron. Soc. **199**, 883 (1982).
10. P. F. C. Blondel, A. Talavera, A. Tjin, and H. R. E. Djie, Astron. Astrophys. **268**, 624 (1993).
11. N. Calvet, P. D'Alessio, L. Hartmann, *et al.*, Astrophys. J. **568**, 1008 (2002).
12. P. J. V. Garcia, J. Ferreira, S. Cabrit, and L. Binette, Astron. Astrophys. **377**, 589 (2001).
13. G. H. Herbig and K. R. Bell, Lick Observ. Bull., No. 1111 (1988).
14. W. Herbst, D. K. Herbst, E. J. Grossman, and D. Weinstein, Astron. J. **108**, 1906 (1994).
15. G. J. Herczeg, J. L. Linsky, J. A. Valenti, *et al.*, Astrophys. J. **572**, 310 (2002).
16. C. Johns, Publ. Astron. Soc. Pac. Conf. Ser. **244**, 147 (2002).
17. S. A. Kaplan and S. B. Pikel'ner, *Physics of the Interstellar Medium* (Nauka, Moscow, 1979) [in Russian].

18. J. H. Kastner, D. P. Huenemoerder, N. S. Schulz, *et al.*, Astrophys. J. **525**, 837 (1999).

19. A. Königl and R. E. Pudritz, *Protostars and Planets IV,* Ed. by V. Mannings, A. P. Boss, and S. S. Russell (Arizona Univ. Press, Arizona, 2000), p. 759.

20. A. S. Kravtsova and S. A. Lamzin, Pis'ma Astron. Zh. **28**, 748 (2002) [Astron. Lett. **28**, 676 (2002)].

21. J. E. Krist, K. R. Stapelfeld, F. Menard, *et al.*, Astrophys. J. **538**, 793 (2000).

22. J. R. Kuhn, D. Potter, and B. Parise, Astrophys. J. **553**, 189 (2001).

23. S. A. Lamzin, Astron. Zh. **75**, 367 (1998) [Astron. Rep. **42**, 322 (1998)].

24. S. A. Lamzin, Astron. Zh. **80**, 542 (2003) [Astron. Rep. **47**, 540 (2003)].

25. P. Mazzotta, G. Mazzitelli, S. Colafrancesco, and N. Vittorio, Astron. Astrophys., Suppl. Ser. **133**, 403 (1998).

26. R. Morrison and D. McCammon, Astrophys. J. **270**, 119 (1983).

27. S. N. Nahar and A. K. Pradhan, Astrophys. J., Suppl. Ser. **111**, 339 (1997).

28. D. E. Osterbrock, *Astrophysics of Gaseous Nebulae and Active Galactic Nuclei* (Univ. Sci. Book, Mill Valey, California, 1989).

29. A. Pradhan, http://www.astronomy.ohio-state.edu/~pradhan (2003).

30. M. M. Romanova, G. V. Ustyugova, A. V. Koldoba, *et al.*, Astrophys. J. **595**, 1009 (2003).

31. S. M. Rucinski, Publ. Astron. Soc. Pac. **104**, 311 (1992).

32. D. A. Smirnov, S. N. Fabrika, S. A. Lamzin, and G. G. Valyavin, Astron. Astrophys. **401**, 1057 (2003).

33. V. V. Sobolev, *A Course on Theoretical Astrophysics* (Nauka, Moscow, 1985) [in Russian].

34. L. Spitzer and E. Jenkins, Annu. Rev. Astron. Astrophys. **13**, 133 (1975).

35. N. I. Shakura and R. A. Syunyaev, Astron. Astrophys. **24**, 337 (1973).

36. F. H. Shu, J. R. Najita, H. Shang, and Zh. Li, *Protostars and Planets IV,* Ed. by V. Mannings, A. P. Boss, and S. S. Russell (Arizona Univ. Press, Arizona, 2000), p. 789.

37. D. A. Verner and G. J. Ferland, Astrophys. J., Suppl. Ser. **103**, 467 (1996).

38. R. A. Webb, B. Zuckerman, I. Platais, *et al.*, Astrophys. J. Lett. **512**, L63 (1999).

39. R. Wichmann, U. Bastian, J. Krautter, *et al.*, Mon. Not. R. Astron. Soc. **301**, L39 (1998).

40. D. J. Wilner, P. T. P. Ho, J. H. Kastner, and L. F. Rodriguez, Astrophys. J. **534**, 101 (2000).

41. P. R. Young, G. Del Zanna, E. Landi, *et al.*, Astrophys. J., Suppl. Ser. **144**, 135 (2003).

42. O. Zatsarinny and S. S. Tayal, J. Phys. B **35**, 2493 (2002).

Translated by V. Astakhov

Rules for Authors

The journal *Pis'ma v astronomicheskiĭ zhurnal* publishes papers on all topical questions of modern astronomy and astrophysics containing as yet unpublished results that require timely publication. Studies pertaining to new, rapidly developing fields of astronomy and astrophysics are given priority. More detailed information about the orientation of the journal can be learned from the introductory article published in its first issue for 1994 (vol. 20, p. 3).

The journal is translated into English by the International Academic Publishing Company Nauka/Interperiodica (MAIK Nauka/Interoperiodica). The English version of the journal is published simultaneously with its Russian version under the title *Astronomy Letters* and is distributed abroad by the American Institute of Physics.

General requirements. The total volume of a manuscript (including tables and figures) should not exceed 25 typewritten pages. It may be increased only in exceptional cases by decision of the editorial board. The text of a paper, irrespective of its volume, should be presented with the maximum possible brevity compatible with its clarity and be carefully edited. The abstract should contain the main results rather than a list of the issues considered in the paper and should not repeat its title.

The paper should give a clear idea of the objectives of the study, the techniques used, and the results obtained. Jargon, terms, and abbreviations used only by a narrow group of experts should be avoided. In particular, proprietary alphanumeric designations of telescopes, instruments, and projects should be avoided; instead, their full names and basic characteristics should be given, if necessary. Overloading papers with formulas and duplicating results in tables and figures is not permitted. Long tables (more than three typewritten pages) may be published in electronic form only (see below).

Submission of manuscripts. Papers written by Russian or foreign authors should be submitted to the Editorial Office at the following address: 117997 Moscow, Profsoyuznaya ul. 90, MAIK Nauka/Interperiodica, Editorial Office of the journal *Pis'ma v AZh*. The phone number of the Editorial Office is (095) 334-76-80, the fax number is (095) 333-53-77, the e-mail address is `pazh@maik.ru`, and the www address: `http://hea.iki.rssi.ru/pazh`.

The manuscript should be signed by all its authors. The address, surname, and first name of the author responsible for communications with the Editorial Office, along with his or her phone number (official and home), fax, and E-mail should be given.

Submitting the manuscript to the Editorial Office, the authors transfer the right to its publication in Russian and in translation into English to the founders, editorial board, and publishers of the Journal (Nauka Academic Publishing Center and MAIK Nauka/Interperiodica) while retaining all of the remaining rights of ownership of their paper. We ask the authors to attach the *Agreement to Transfer Copyright* to their manuscript according to the form given below:

Agreement
to Transfer Copyright

We, the undersigned, the authors of the manuscript
....
transfer the exclusive right to publication of this manuscript in Russian and in translation into English and to its distribution in Russia and worldwide to the founders, editorial board, and publishers of the journal *Pis'ma v AZh* (Nauka Academic Publishing Center and MAIK Nauka/Interperiodica). We confirm that this publication does not violate the copyright of other individuals and organizations.

Signatures of the authors
(surname, first name, date)

The papers of foreign authors submitted in English are translated into Russian at MAIK Nauka/Interperiodica. Authors from the Commonwealth of Independent States should submit their papers in Russian. An author's translation of the paper into English may be attached to the Russian version, but the Editorial Office does not guarantee that this translation will be completely or partially used when publishing the English version of the journal. For questions of using such a translation, its evaluation,

and payment, the authors should refer directly to MAIK Nauka/Interperiodica by phone (095) 334-74-20 (Mikhail Efimovich Gorelik).

Preparing manuscripts. Papers should be submitted in one typewritten (or computer-printed) copy with standard (12 pt) font with double spacing on one side of each page. Margins 25−30 m in width should be left on the left side of the page. The manuscript pages, together with tables and figures, should be numbered separately.

The following should be printed on the title page: the paper title, the initials and surnames of all authors (separated by a comma), the full name of the institution at which the work has been performed, and a brief abstract (∼150−200 words) with key words. The e-mail address of one of the authors (responsible for communications) should be given at the bottom of the page, with an asterisk being placed near his or her surname. If the study was carried out at different institutions, then a reference in the form of a number that specifies the institution where the author works should be given after the surname of each coauthor. A list of institutions is given after the surnames of all authors. As key words, it is desirable to use the section titles from the annual subject index of the journal (published in issue no. 12). A translation of the paper title, the initials and surnames of all authors, the institutions, and the abstract into English should be given on a separate page. It is also desirable to translate the special terms and the surnames of the authors of the effects and methods being discussed. The main body of the text should begin from the second page of the manuscript. It is recommended to break down the paper into sections, to begin it with an introduction formulating the problem, and end it with conclusions listing the main results of the work (section numbering should be avoided).

The text of the paper should be carefully edited. To distinguish the letters O (upper case), o (lower case), and 0 (zero), the letters O (upper case) and o (lower case) should be marked by two bars, $\underline{\underline{O}}$ and $\overline{\overline{o}}$, while zero should be marked by a bracket under it, $\underset{\smile}{0}$.

In general, the dimensions of quantities should be given using a slash (e.g., cm/s, g/cm^3, but the dimensions of number density should be written as cm^{-3}, not as 1/cm^3). The fractional part of a number should be separated from its integer part by a decimal point (e.g., 3.1416). In exponential form, such numbers are written as 1.3×10^{-2}, not as 1.3E−2. An approximate equality is denoted by $\approx$ or $\simeq$, an order-of-magnitude equality is denoted by $\sim$ (commonly used in the text), and proportionality is denoted by $\propto$.

Figures. The paper should not be overloaded with figures. If there are several interrelated figures, they should be arranged rationally and sparingly. The coordinate axes should be scaled; it should be indicated what physical quantity is plotted on them and what its dimensions are. It is not recommended to reproduce previously published figures for illustration purposes.

Figures and photographs should be submitted separately rather than inserted in the text of the manuscript. The quality of figures should be high enough to be reproducible in the journal in the form submitted by their authors. When plotting observational data, it is desirable to indicate observational error bars. Figures drawn with a pencil are not accepted. Brief captions must be submitted with the figures, which should be gathered on a separate page. There must be the minimum possible number of words in the figure itself; explanations should be given in the figure captions or in the text of the paper.

Literature. References to cited literature in the text should be given in the form of an author's surname and the year of publication of the paper with the addition of a letter for references to several publications of the author in the same year. For two authors, the surnames are separated by a comma; for three or more coauthors, only the first surname is given with the addition of *et al.* It is desirable to include surnames in the text of a phrase; when it is not possible, they should be given in parentheses.

The cited literature is given under the title References at the end of the paper in an alphabetic order of writing the surname of the first author. The surnames and initials of three authors with the addition of *et al.* are given in a reference. An abbreviated name of the journal in the system of abbreviations used in *Pis'ma v AZh*, the volume, the first page, and the year of publication are then given after a comma. For books, the surname(s) and initials of their author(s) or editor(s) (if it is a collection of works) the full title of the book, and, in parentheses, the publisher, city, and year of publication should be given. In references to papers published in conference proceedings, the conference name and then, in parentheses, editors, publisher, city, year of publication, and the first page of the publication should be given.

The following examples illustrate the rules for citing literature listed above:

1. A. Vikhlinin and W. Forman, Astrophys. J. **455**, 109 (1995).

2. O. Yu. Gnedin and D. G. Yakovlev, Pis'ma Astron. Zh. **19**, 280 (1993).

3. C. R. Canizares and J. L. White, *Active Galactic Nuclei, IAU Symp. 134*, Ed. by D. Osterbrock and J. Miller (Kluwer Acad. Publ., Dordrecht, 1989), p. 161.

4. E. M. Lifshitz and L. P. Pitaevskiĭ, *Statistical Physics* (Nauka, Moscow, 1973), Part 2.

5. O. V. Maxwell, Astrophys. J. **231**, 201 (1979).

6. D. M. Smith, M. Leventhal, R. Cavallo, *et al.*, Astrophys. J. **471**, 783 (1996).

7. R. W. Hanuschik, *Supernovae*, Ed. by S. E. Woosley (Springer-Verlag, N.Y., 1991), p. 26.

Tables. Since 1997, the Journal has been published long tables (more than three typewritten pages) in electronic form only and short tables in both printed and electronic forms. The electronic versions of tables are accessible via the Strasbourg Astronomical Data Center/CDS and its Russian branch, the Astronomical Data Center of the Russian Academy of Sciences (RAS). They are accessible from any computer connected to the Internet and may be retrieved via the anonymous ftp or www interfaces:

ftp://cdsweb.u-strasbg.fr/pub/cats/J

(ftp cdsarc.u-strasbg.fr, cd /pub/cats/J)

http://cdsweb.u-strasbg.fr/cats/J.htx.

By agreement with the CDS, the Astronomical Data Center of the RAS collects the electronic versions of the tables published and being republished in Russian astronomical journals and sends them to CDS after verification. If tables containing observational or computational data occupy a great deal of space in the paper, then its authors should prepare their electronic versions (in ASCII codes) and send them by e-mail to Veta Sergeevna Avedisova at the RAS Institute of Astronomy's Astronomical Data Center (e-mail: `veta@inasan.rssi.ru`). When submitting the paper, the author(s) should in any case attach one copy of the tables in printed form for evaluation.

Detailed instructions on how to prepare tables in the CDS format can be found at the following ftp and www sites:

ftp://hea.iki.rssi.ru/pub/pazh/instrelp.txt,

ftp://hea.iki.rssi.ru/pub/pazh/instrelp.ps.Z

http://hea.iki.rssi.ru/pazh

For explanations and help, the authors are referred to V.S. Avedisova at the above address or by phone at (095) 931-08-81. General instructions on preparing tables can also be obtained directly from CDS at the following ftp sites:

ftp://cdsarc.u-strasbg.fr/pub/cats/doc.dvi

ftp://cdsarc.u-strasbg.fr/pub/cats/doc.ps.Z

Electronic version of the paper. Simultaneously with the traditional (printed) version of the paper, the author(s) should submit electronic version (preferably a PS file) to the editorial office; this will speed up the evaluation process and improve the quality in preparing the paper for publication. The prepared files should be sent to the e-mail address of the editorial office (`pazh@maik.ru`) or on a floppy disk. An inventory (e.g., in the form of a file) in which it is necessary to specify the floppy format, the operating system, the name of the text editor, the list of files, the name of the journal, the paper title, and the surname(s) and initials of the author(s) should be added to the set of files.

It is desirable to submit the main body of the paper in LaTeX, TeX, or TextOnly formats with the addition of a PS file. In certain cases, the text may be submitted in Microsoft Word for Windows format with an indication of the version of the publishing system. The style file for the journal can be found on the www page (`http://hea.iki.rssi.ru`).

When preparing graphics files, the authors should adhere to the following rules:

The figures and illustrations should be black-and-white; in exceptional cases, the figures may be published in color in the form of color insets, if necessary, at the expense of the authors.

The TIFF format is preferred for gray photographs and line drawings, although the JPEG and GIF may be used; the resolution should be no worse than 600 dpi (dots per inch) for line drawings and no worse than 300 dpi for scanned gray drawings and photographs.

For vector drawings and diagrams (figures prepared in vector graphics applications), it is desirable to use the EPS format.

Each file should contain only one figure.

The files should be named in such a way as to be understandable to which paper they belong and which figure they contain.

For questions involving the preparation of the graphics and texts of papers, the authors should refer to the joint editorial office of physics journals by phone at (095) 335-83-66 or E-mail `ced@maik.ru`.

Evaluation. As a rule, the papers submitted to the journal *Pis'ma v AZh* are directed to two expert panels for review; in several cases, additional evaluation may be necessary. When the authors receive reviews that point to the necessity of revising the paper, the editorial office should receive an answer in no more than three months. Otherwise, the paper is deemed to

be withdrawn by the author(s). If the paper is rejected, the editorial office retains one copy.

Fees, reprints, and payment for publication. No payment is collected from the authors for publication in the Russian version of the journal, and no fee is paid. A fee is paid for publication in the English version to the authors from the Commonwealth of Independent States. The authors receive Russian and English reprints of their paper in the form of PDF files.

An electronic version of these rules, tables of contents for the Russian version of the journal *Pis'ma v AZh* for the past several years, and other useful information can be found on the homepage of the journal at the WWW address `http://hea.iki.rssi.ru/pazh`.

A list of accepted abbreviations of major astronomical and physical journals

Astron. Rep	*Astronomy Reports*
Sol. Sys. Res.	*Solar System Research*
Astron. Tsirk	*Astronomical Tsirkulyar*
Astrofizika	*Astrofizika*
JETP	*Journal of Experimental and Theoretical Physics*
Izv. KrAO	*Izvestiya Krymskoi Astrofizicheskoi Observatorii*
Space Res.	*Space Research*
Perem. zvezdy	*Peremennye zvezdy*
Astron. Lett.	*Astronomy Letters*
JETP Lett.	*Journal of Experimental and Theoretical Physics Letters*
Preprint IKI RAN	*Preprint Instituta Kosmicheskikh Issledovanii RAN*
Soobschch SAO RAN	*Soobshcheniya Spetsial'noi Astrofizicheskoi Observatorii RAN*
Uspekhi Fiz. Nauk	*Uspekhi Fizicheskikh Nauk*
Acta Astron.	*Acta Astronomica*
Adv. Space Res.	*Advances in Space Research*
Ann. Rev. Astron. Astrophys.	*Annual Review of Astronomy and Astrophysics*
Astron. Astrophys.	*Astronomy and Astrophysics*
Astron. Astrophys. Rev.	*Astronomy and Astrophysics Review (the)*
Astron. Astrophys. Suppl. Ser.	*Astronomy and Astrophysics Supplement Series*
Astron. Astrophys. Trans.	*Astronomical and Astrophysical Transactions*
Astron. J.	*Astronomical Journal (the)*
Astron. Lett.	*Astronomy Letters*
Astron. Nachr.	*Astronomische Nachrichten*
Astron. Rep.	*Astronomy Reports*
Astron. Telegram	*Astronomer's Telegram*
Astrophys. J.	*Astrophysical Journal (the)*
Astrophys. J. Suppl. Ser.	*Astrophysical Journal Supplement Series (the)*
Astrophys. Lett.	*Astrophysical Letters*
Astrophys. Lett. Comm.	*Astrophysical Letters & Communications*
Astrophys. Space Sci.	*Astrophysics and Space Science*
Aust. J. Phys.	*Australian Journal of Physics*
Bull. Am. Astron. Soc.	*Bulletin of the American Astronomical Society*
Canad. J. Phys.	*Canadian Journal of Physics*
ESO Messenger	*ESO Messenger (the)*
Exp. Astron.	*Experimental Astronomy*
IAU Circ.	*International Astronomical Union, Circular*
Icarus	*Icarus*
MNRAS	*Monthly Notices of the Royal Astronomical Society*
Nature	*Nature*
New Astron.	*New Astronomy*
Phys. Lett.	*Physical Letters*
Phys. Rev.	*Physical Review*
Publ. Astron. Soc. Japan	*Publications of the Astronomical Society of Japan*
Publ. Astron. Soc. Pacific	*Publications of the Astronomical Society of the Pacific*
Science	*Science*
Solar Phys.	*Solar Physics*
Sov. Astron.	*Soviet Astronomy*
Sov. Astron. Lett.	*Soviet Astronomy Letters*
Space Sci. Rev.	*Space Science Reviews*

─────────────── **ERRATA** ───────────────

Erratum: **"Anomalous Fe II Spectral Effects and High H I Lyα Temperature in Gas Blobs Near η Carinae"**

[*Astron. Lett.* 30, 58 (2004)]

S. Johansson and V. S. Letokhov

The formula (16) on page 62 should read

$$\alpha_{32} = \sigma_{32}\Delta N_{32}, \text{ where } \Delta N_{32} = W_{14}^{\text{exc}}\tau_3 N_1.$$